University of Zielona Góra
Faculty of Physics and Astronomy

Subject matter: Physical Science
Discipline: Physics

Maciej Sznajder

Degradation studies of materials under space conditions; under special emphasize of recombination processes.

(Badanie procesów degradacji materiałów w warunkach przestrzeni kosmicznej, ze szczególnym uwzględnieniem procesów rekombinacji)

Acceptance of supervisor:

PhD thesis
written under the supervision of:
dr hab. Ulrich Geppert, prof. UZ

Zielona Góra, 2013

Contents

Abstract

This thesis explains the importance of degradation processes of materials under space conditions. Studies of materials used in the space technology play a crucial role in each planned space mission. A large number of specialists, institutes, and facilities located all around the world indicate the importance of the subject.

A new degradation process has been proposed: formation of molecular hydrogen bubbles on metallic surfaces under proton irradiation. The process originates from recombination of solar protons with metallic free electrons into neutral hydrogen atoms. For solar protons three processes lead the recombination: the Auger-, the resonant-, and the Oppenheimer-Brinkman-Kramers (OBK) -process, respectively. Therefore, a detailed mathematical description of these processes is presented. The cross section of the OBK-process for the special case of light incident ions (here protons) has been calculated.

A thermodynamical model of bubble growth has been developed. The model is based on the assumption that the process is quasistatic. This means that the growth of bubbles proceed much slower then the Hydrogen recombination. As a result of that process, the irradiated metal is covered with hemispherical bubbles. A quantitative relation between the reflectivity of metal, and the bubbles surface density and radii has been derived. It is worth mentioning that the maximum decrease of the reflectivity of the irradiated sample was 26.5%. Such a decrease leads to changes of the thermo-optical properties of irradiated metal surfaces.

Results available from laboratory irradiation experiments have been compared with the presented model of bubble growth. The results of the model calculations coincide very well with observations of bubble growth in terrestrial laboratories. It has been shown that the conditions in the near vicinity of the Sun are favorable for the bubble grow process. Therefore, the model presented in this thesis provides a useful tool for well-founded forecast of degradation effects under space conditions.

Streszczenie

Abstract in Polish.

Chapter 1

Introduction

The importance of degradation processes of materials used in space technology is undeniable. All of the materials planned for space applications in which they will be exposed to the radiation in space have to be evaluated for their behavior under particle and electromagnetic irradiation [6, 28]. It is known from many of these evaluation tests that particle and electromagnetic radiation can significantly degrade materials and, e.g. lead to changes in their mechanical behavior or thermo-optical properties (see e.g. [3, 45, 65, 96]). These changes can cause early failures of satellite components or even failures of complete space missions [21].

The thermo-optical properties of materials are defined by a pair of parameters: the solar absorption coefficient α_S, and the thermal emission coefficient ϵ_t, respectively. According to the ECSS standard (European Cooperation for Space Standardization) α_S is defined as ratio of the solar radiant flux absorbed by a material (or body) to that incident upon it [29], while ϵ_t is the ratio of the radiant intensity of the specimen to that emitted by a black body radiator at the same temperature and under the same geometric and wavelength conditions [29].

Especially sensitive for any changes of thermo-optical properties are those materials which are exposed directly to the solar wind. That is the case for instance with solar sails. A solar sail is basically a large sheet of highly reflecting material bound to the deploying system by composite materials. The propulsion system of the sail is based on the momentum transfer made by solar photons. First concepts of sail-crafts have been made by several authors including the father of Astronautics, Konstanty Ciołkowski, also by Fridrikh Tsander and Herman Oberth [72]. Due to technological reasons the sail concept has vanished for more than 30 years. The idea has returned to the scientific and engineering arena after the article of Richard Garwin [32] has been published. After that, a significant amount of both theoretical and practical work has been performed to establish solar sailing as a propulsion technology, considering its astrodynamics, mission applications and technological requirements [72].

The revitalization of the solar sail propulsion technology at the DLR-Institute of Space Systems is one of the motivations for the thesis presented here. Within the 3-step DLR-ESA project "GOSSAMER" [33] extensive degradation studies of solar sail materials have been performed. It was decided to organize the project in three steps with increasing complexity. GOSSAMER-1 is a sail of a 5m $\times$ 5m in a 320 km Earth orbit. The planned start of the mission is 2015. GOSSAMER-2 will be a sail of a 20m $\times$ 20m in a 500 km Earth orbit. The sail will be launched in 2017. GOSSAMER-3 will be a sail of a 100m $\times$ 100m in a $>$10000 km Earth orbit. The start of this sail-mission is planned in 2019. Since sails will operate in different orbits, their materials will be exposed to slightly different environmental

effects. Each sail mission requires specific investigation according to the erosion processes which may happen. Laboratory tests have proven that surface destroying effect of particle and electromagnetic irradiation. However, no samples of materials that have been exposed to irradiation with solar protons in the interplanetary space have ever been returned to Earth. The real process of material degradation in space is yet unexplored. Therefore, this thesis is intended to provide some theoretical tools for estimates how much materials can suffer from the solar wind under space conditions.

Degradation may be caused by charge particles, electromagnetic radiation, atomic oxygen as well as space debris and micro-meteorites. In this thesis special attention is devoted to effects of irradiating protons. In Low Earth Orbits (LEOs) atomic oxygen is the main source of degradation, while in the interplanetary medium the solar wind and solar electromagnetic radiation dominates the degradation effects. Solar wind consists of charged particles especially protons and electrons. They originate from coronal mass ejections and solar flares. Electrons with energies from about 0.01 eV up to a few hundreds of eV originate from coronal mass ejections. Flares are the sources of electron with energies from 1 MeV up to hundreds of MeV. The solar protons carry energies from 0.2 keV to a few tens of keV in the solar wind and in coronal mass ejections and up to a few GeV when produced in solar flares [53].

The structure of the thesis is as follows. In Section 2 the interaction of the incident particles with matter is reviewed. The main content of this section is focused on recombination processes of incident protons. Protons penetrating metallic targets lose their energy and continuously bound and loss an electron. At rest all of the incident protons recombine with free electrons present in any metal. Depending on the kinetic energy of incident protons, one can distinguish four recombination processes: Auger- (2.4.1), resonant- (2.4.2), Oppenheimer-Brinkman-Kramers- (2.4.3), and the Radiative Electron Capture - process. For solar protons first three phenomenon dominate the recombination. A modification of the Oppenheimer-Brinkman-Kramers process will be presented. This modification is an original contribution of the thesis presented here. That modification assumes that the mass of the incident ion is much smaller than the mass of target's atoms. That is the situation when metallic samples are bombarded by Hydrogen ions.

Section 3 is devoted to degradation processes of materials under space conditions. A short overview of the most important erosion processes is presented. The possibility to charge metallic foils by solar wind is investigated (Subsection 3.1.1). Then the sputtering, an important degradation process which describes a removal of target's atoms by incident particles, is shortly described (Subsection 3.1.2). The process leads to mass loss of irradiated materials and is important for long term space missions. Next the effects of Atomic Oxygen (ATOX) is discussed (Subsection 3.1.3). ATOX is highly concentrated in the Low Earth Orbits regions. The concentration depends on altitude as well as on the activity of the Sun. Then a few experimental facts of exposure of a collection of materials used in space technology to the electromagnetic radiation are presented in Subsection 3.1.4.

Section 3.2 presents a new degradation process which may appear in the interplanetary medium: a formation of molecular hydrogen bubbles on metallic surfaces exposed to solar protons. Hydrogen is created in the sample by incident protons which recombine with its free electrons. Surfaces covered with bubbles will change its thermo-optical properties. The proposed blistering phenomenon would play a crucial role in the planned solar sail missions, since any change of the properties of its material leads to changes of the propulsion of the sail-craft or even to a failure of the entire mission. The theoretical description of dynamics of bubble growth is shown in the Subsection 3.2.1. It is a thermodynamic approach. The theory is based on the assumption that the bubbles grow in a quasistatic way, i.e. during

each time step a small portion of H_2 molecules is merged to the bubbles and an equilibrium is established. Subsection 3.2.2 presents a collection of experimental facts about bubble formation. Many materials have been investigated, for instance: Aluminum, Cooper, Iron, Tungsten, Palladium, Tantalum, and Vanadium. H^+ and H_2^+ ion fluxes have been taken into account. Then the possibility of bubble formation under space conditions is investigated. Characteristic temperatures as well as proton fluxes necessary for the formation are present in the interplanetary medium. Then a few numerical models of bubble formation and growth are presented. The reflectivity of Aluminum samples covered with different surface densities and different sizes of bubbles is studied in Subsection 3.2.3. The relation between bubble size and density to the reflectivity of irradiated materials provides a direct link to the solar sail propulsion efficiency, since the acceleration of the sail-craft is directly proportional to the reflectivity of used sail material. Finally in the Chapter 4 the Conclusions & Outlooks are presented.

It is planned that the blistering process will be validated by use of the Complex Irradiation Facility, located at DLR Bremen, Germany. The facility simulates complex space environmental conditions, i.e. high vacuum, simultaneous irradiation with protons and electrons as well as the full spectrum of electromagnetic radiation. With its uniqueness, flexibility and validated radiation sources, the facility is one of the best in Europe and will suited to test in the near future the predictions made by the thermodynamical approach presented here in this thesis.

Chapter 2

Interaction of the incident particles with matter

One can distinguish three types of interactions of incident particles with matter. First, *elastic scattering* - it takes place when the kinetic energy of the collision partners is conserved. Elastic scattering is also a source of heating of metallic foils, because there is a transfer of kinetic energy from the incident particle to the ions of the target [66]. Second, *non-elastic scattering* - where the internal energy of particles is changed. It is not a creation process of new particles but a source of destruction of crystals and molecular chains [66]. This phenomenon will be considered in Section 3. Third, *nuclear reactions* - in the result new particles are created [5, 86]. These physical processes will not be considered in this thesis.

If one wants to study irradiation processes and its properties, one has to consider the total and differential cross section. One can estimate energy loss per unit length by ionization and excitation when thin materials are bombarded with charged particles. These physical processes are described by the Bohr formula, and will be studied in detail in the following sections.

2.1 Total and differential cross section

The thicker the irradiated metallic foil, the smaller the number of the incident particles at a constant energy that will penetrate it and leave the foil at its back side. Thus the initial particle number decreases with increasing depths.

Let's study the concept of the total cross section Σ_{total}. The basic assumption is that each target ion represents a total cross section. If an incident particle strikes such an area, it will be scattered. Otherwise it will not interact [23]. If the foil has a thickness of Δx, which is called the *penetration length parameter* measured in gcm^{-2} and n_0 is the number of lattice ions in the unit volume, the probability $P(x)$ that incident particle scatters in Δx is [23]:

$$P(x) = \frac{\Sigma_{\text{total}} n_0}{\rho} \Delta x, \tag{2.1}$$

where ρ is the density of the material. Whenever a particle scatters, number of particles $N_{\text{particles}}$ at distance x decreases by the value of $dN_{\text{particles}}$:

$$dN = -N_{\text{particles}} P(x). \tag{2.2}$$

By use of the so-called attenuation coefficient $\mu = \frac{\Sigma_{\text{total}} n_0}{\rho}$ one integrates Eq. 2.2, and get a simple formula between an initial intensity $I_{\text{particles,0}}$ and the intensity $I_{\text{particles}}$ at a given depth x, where intensity is the number of incident particles in unit time $I_{\text{particles}} = N_{\text{particles}}/t$, $N_{\text{particles,0}}$ is the number of incident particles [53, 54, 59, 86]:

$$I_{\text{particles}} = I_{\text{particles,0}} e^{-\mu x}. \tag{2.3}$$

The attenuation coefficient depends on the physical properties of foils and on the energy of the incident particles [53]. The Eq. 2.3 is correct under the following assumptions:

1. The decrease of the incident particle intensity is proportional to the number of collisions centers in the foil, where kinetic energy can be dissipated.

2. The character of interactions does not depend on the thickness of a metallic foil [5, 86].

The total cross section is a great theoretical tool to study many physical problems. However, it will be insufficient if one wants to find the angular distribution of scattered particles. In that situation the concept of the differential cross section is used [86].

The initial path of inflowing particles is bended by metallic foil ions. The deflection angle δ is gradually different from zero. The impact parameter ξ is defined as closest distance of the incident particle with respect to the ion [66, 85, 86]. The range of deflection angles corresponds to a ring of impact parameters. The inner and outer radius is ξ and $\xi + d\xi$, respectively. The equation for the differential cross section is:

$$d\Sigma = 2\pi\xi d\xi. \tag{2.4}$$

By determining two independent relations for the change in the momentum Δq of the scattered initial particle, it is possible to find a general relation between the impact parameter ξ and the scattering angle δ [85]. δ varies from 0 to π. From the classical theory of electrodynamics the force F_C acting between two charges ze and Ze, being in a distance r to each other is:

$$F_{\text{C}} = \frac{zZe^2}{4\pi\epsilon_0 r^2}. \tag{2.5}$$

The geometry of the phenomenon allows to write $F = F_{\text{C}} cos\phi$.
Now the momentum transfer Δq may be written as the time integral of the force F [85]:

$$\Delta q = \int_{-\infty}^{\infty} F dt = \frac{zZe^2}{4\pi\epsilon_0} \int_{-\frac{\pi-\delta}{2}}^{\frac{\pi-\delta}{2}} \frac{cos\phi}{\omega_0 r^2} d\phi, \tag{2.6}$$

where ω_0 is the angular frequency, ϕ is the angle between radius vector r and the bisector [85]. As seen in Fig. 2.2, the angular momentum $\vec{L} = \vec{r} \times m\vec{v}$ at points A and B is given by:

$$L_{\text{point A}} = rmv \sin\frac{\pi}{2} = m\omega_0 r^2, \tag{2.7}$$

$$L_{\text{point B}} = rmv \sin\psi = rm\xi. \tag{2.8}$$

The conservation of angular momentum in an elastic scattering process, $L_{\text{point A}} = L_{\text{point B}}$, returns for the angular frequency:

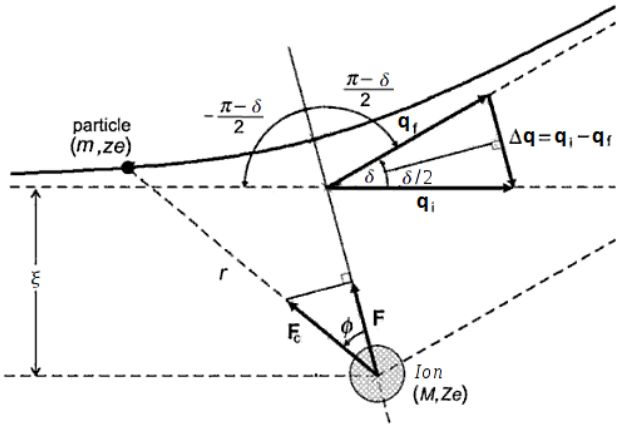

Figure 2.1: Scattering of an incident particle on a metallic foil ion, where Δp is the change in the particle momentum. The ion is located in the outer focus of the hyperbolic trajectrotry of the particle [85].

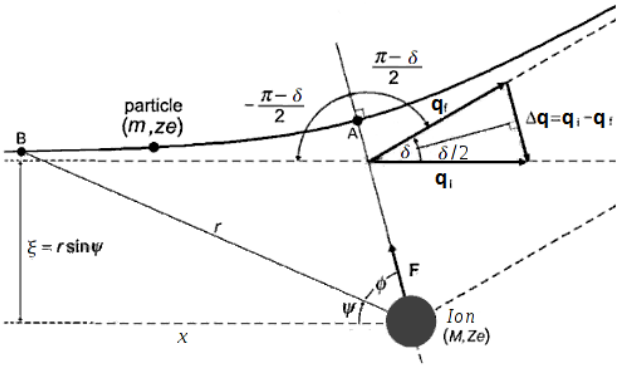

Figure 2.2: Geometry of the phenomenon. Point A is the apex of the hyperbola - trajectory of incident particle. Point B is assumed to be at large distance from the ion [85].

$$\omega_0 = \frac{v\xi}{r^2}, \tag{2.9}$$

where m and v are the mass and velocity of the incident particle, respectively. After inserting Eq. 2.9 into Eq. 2.6 and solving the integral, the momentum transfer in the collision process is [85]:

$$\Delta q = 2\frac{zZe^2}{4\pi\epsilon_0 v\xi}\cos\frac{\delta}{2}. \tag{2.10}$$

Suggested from Fig. 2.1, if $q_\mathrm{f} = mv_\mathrm{i}$ the momentum transfer Δq may be written also as:

$$\Delta q = 2mv\ sin\frac{\delta}{2}. \tag{2.11}$$

The required relation for the impact parameter ξ is obtained after combining Eq. 2.10 and Eq. 2.11 [85]:

$$\xi = \frac{zZe^2}{8\pi\epsilon_0 E_K} cot\frac{\delta}{2}, \tag{2.12}$$

where z and Z are the atomic numbers of a incident particle and a foil ion respectively. E_K is the kinetic energy of an incident particle. One can now write the Eq. 2.4 in a different form:

$$d\Sigma = 2\pi \frac{\xi}{sin\delta} sin\delta \left|\frac{d\xi}{d\delta}\right| d\delta. \tag{2.13}$$

Calculating $\frac{d\xi}{d\delta}$ and using the solid angle $d\Omega = 2\pi sin\delta\ d\delta$ one has:

$$\frac{d\Sigma}{d\Omega} = \left(\frac{zZe^2}{16\pi\epsilon_0 E_K}\right)^2 \frac{1}{sin^4\frac{\delta}{2}}. \tag{2.14}$$

Equation 2.14 describes the differential cross section for scattered particles. It is called the Rutherford formula [85, 86]. The cross section depends on two factors:

1. If the kinetic energy of incident particles increases, then the differential cross section will decrease. Therefore, the incident particles with the lower kinetic energy will have a higher probability to be scattered off by ions of the foil.

2. For a given target foil (Ze) and given incident particle (ze, E_K), a large differential cross section implies a small scattering angle δ.

3. In the process of continuous irradiation of the foil with electrons and/or ions, the degree of ionization of the foil atoms (see Section 2.2) grow, hence, the degradation process may be characterized by the increase of the differential cross section.

2.2 Energy loss per unit length by ionization and excitation

Collisions with ions of the metallic foil are caused by incident particles which penetrate the material, hence ions can get additional energy. Atoms can be excited or ionized, while the incident particles lose their energies simultaneously [86]. If the energy loss per unit length per ion is known, one can calculate the energy loss per unit length of an incident particle, which travels through the foil: $-dE/dx$. It is proved experimentally, that this quantity depends on the type and on the energy of the incident particle and on the physical properties of the metallic foil [5, 86]. The required formula is obtained by use of the principle of conservation of energy and momentum, taking into account also the geometry of the phenomenon. Only perpendicular forces act on the incident particle. Forces parallel to the line of flight are canceled out by the symmetry [66]:

$$F = \frac{zZe^2}{4\pi\epsilon_0 r^2} \sin\psi, \qquad dt = \frac{dx}{v}, \tag{2.15}$$

where dx is the path of the incident particle which moves in unit time dt. Now, using the geometry of the collision process (Fig. 2.2):

$$\frac{\xi}{x} = \tan\psi, \qquad r = \frac{\xi}{\sin\psi}, \qquad dx = -\frac{\xi}{\sin^2\psi} d\psi. \tag{2.16}$$

The momentum transfer Δq of the incident [66] is:

$$\Delta q = \int_{-\infty}^{\infty} F dt = -\frac{zZe^2}{4\pi\epsilon_0 \xi v} \int_0^{\pi} \sin\psi d\psi. \tag{2.17}$$

The energy transfered to the metallic foil nuclei is [66]:

$$\frac{\Delta q^2}{2M} = \frac{1}{2M}\left(\frac{zZe^2}{2\pi\epsilon_0 \xi v}\right)^2. \tag{2.18}$$

The energy loss rate per unit length dx is the product of Eq. 2.18 and the number of collisions in the metallic foil with impact parameter in range ξ to $\xi + d\xi$:

$$\frac{dE}{dx} = -\int_{\xi_{min}}^{\xi_{max}} n_0 2\pi\xi d\xi \frac{1}{2M}\left(\frac{zZe^2}{2\pi\epsilon_0 \xi v}\right)^2. \tag{2.19}$$

Finally, after integration, one finds:

$$\frac{dE}{dx} = -\frac{n_0}{\pi M}\left(\frac{zZe^2}{2\epsilon_0 v}\right)^2 \ln\left(\frac{\xi_{max}}{\xi_{min}}\right), \tag{2.20}$$

where M is the mass of an ion of the metallic foil material, v is the velocity of the incident particle. The energy loss per unit length depends on:

- the velocity of the incident particle $\sim v^{-2}$. The higher the kinetic energy, the lower loss rate.
- the square of the incident and ion number, z^2 and Z^2, respectively. It means that if z increases by a factor of two, the energy loss rate per unit length will increase by a factor of four, hence, Eq. 2.20 is very sensitive for changes of the atomic numbers and ionization process.
- the logarithm of ratio of the upper and lower limits of the impact parameter, i.e. its a weak dependency.

The evaluation of ξ_{max} and ξ_{min} will be studied in next subsections, for the protons as incident particles. The case of relativistic protons as the incident particles will be considered as well.

2.3 Interactions of protons with matter

The previous subsection discusses the general problem of the energy loss per unit length by an incident particle. According to the experimental data [102] protons lose energy while penetrating a target mainly by collisions with electrons. Target atoms are then ionized additionally. Therefore the relation 2.20 has to be modified. The mass of the target ion M is replaced by the mass of an electron m_e:

$$\frac{dE}{dx} = -\frac{n_0}{\pi m_e}\left(\frac{zZe^2}{2\epsilon_0 v}\right)^2 \ln\left(\frac{\xi_{max}}{\xi_{min}}\right), \tag{2.21}$$

This subsection studies the integration limits of the impact parameter, Eq. 2.21 in two cases: non - relativistic and relativistic, respectively.

2.3.1 Non-relativistic case

Protons with kinetic energies not larger than 1 MeV are certainly non-relativistic. The maximum value of the impact parameter $\xi_{\max}$ is estimated under the assumption that the metallic foil ion can be excited or ionized. Duration of the collision is equal or longer then a circulation time of the electrons in the ion [66, 86]. Collecting these information together one can calculate the physical quantity ξ_{max} by use of the condition that the collision time (time in which incident proton interacts with the electron) equals the circulation time of the electron in the ion:

$$\frac{2\xi_{\max}}{v} = \frac{2\pi}{\omega_0}, \tag{2.22}$$

where ω_0 is the angular velocity of an electron in an ion, v is the velocity of the incident proton.

The minimum value of the impact parameter can be estimated for two cases, using either classical or quantum physics. First let's consider the classical approach.

If the electrostatic potential interaction energy of the incident proton and the metallic foil electron is equal to the maximum possible energy transfer (the maximum transfer of the energy to the electron by the incident proton is possible if one assumes perfect elastic collision, then the kinetic energy becomes $\frac{1}{2}m_{\mathrm{e}}\left(2v\right)^2 = 2m_{\mathrm{e}}v^2$), it corresponds to the minimum distance of the approach [66]:

$$\frac{ze^2}{4\pi\epsilon_0\xi_{\mathrm{min_C}}} \approx 2m_{\mathrm{e}}v^2, \qquad \xi_{\mathrm{min_C}} \equiv \xi_{\mathrm{min_{Classical}}}, \tag{2.23}$$

where v is the velocity of the incident proton in the laboratory frame.

Now let's calculate the quantum mechanical approach of the minimum impact parameter. The maximum velocity transfer to the electron is $2v$, hence change of its momentum is $\Delta q = 2m_{\mathrm{e}}v$. From the Heisenberg Uncertainty Principle it is known that $\Delta x > \hbar/4m_{\mathrm{e}}v$ [66], hence:

$$\xi_{\mathrm{min_Q}} = \frac{\hbar}{4m_{\mathrm{e}}v}, \qquad \xi_{\mathrm{min_Q}} \equiv \xi_{\mathrm{min_{Quantum}}}. \tag{2.24}$$

It is important to find a criterion whether the classical or quantum approach is appropriate. It can be done by studying the ratio of the two impact parameters:

$$\frac{\xi_{\mathrm{min_Q}}}{\xi_{\mathrm{min_C}}} = \frac{2\pi\epsilon_0\hbar v}{zZe^2}. \tag{2.25}$$

By use of a fine structure constant $\alpha_{\mathrm{c}} = e^2/4\pi\epsilon_0 c\hbar \approx 1/137$, Eq. 2.25 receive a much simpler form:

$$\frac{\xi_{\mathrm{min_Q}}}{\xi_{\mathrm{min_C}}} = \frac{1}{2zZ\alpha_{\mathrm{c}}}\frac{v}{c}. \tag{2.26}$$

When the Eq. 2.26 is larger then unity, the quantum approach should be used, otherwise classical one.

Finally the energy loss rate per unit length for non-relativistic energies of protons is [66]:

$$\frac{dE}{dx} = -\frac{n_0}{\pi m_{\mathrm{e}}}\left(\frac{ze^2}{2\epsilon_0 v}\right)^2 \ln\left(\frac{8\pi^2\epsilon_0 m_{\mathrm{e}}v^3}{\omega_0 ze^2}\right). \tag{2.27}$$

The corresponding formula for quantum case is:

$$\frac{dE}{dx} = -\frac{n_0}{\pi m_\mathrm{e}} \left(\frac{ze^2}{2\epsilon_0 v}\right)^2 \ln\left(\frac{4\pi m_\mathrm{e} v^2}{\hbar\omega_0}\right). \tag{2.28}$$

Equation 2.28 can be rewritten into a more simple and usable form. First step is to replace $\hbar\omega_0$ by its relation to the binding energy $\frac{1}{2}\hbar\omega_0$ of the electron in Bohr's description [66]. The binding energy is also the ionization potential I_p which should be a properly weighted mean over all states of the electrons in the metallic foil ions $\bar{I}_\mathrm{p}$ that ionization potential has to be found experimentally [66]. In a second step we put all this information together and find:

$$\ln\left(\frac{2\pi m_\mathrm{e} v^2}{\hbar\omega_0}\right) \equiv \ln\left(\frac{2m_\mathrm{e} v^2}{\bar{I}_\mathrm{p}}\right), \tag{2.29}$$

In classical approach the energy loss per unit length depends almost on the same conditions as in Eq. 2.21, because logarithm yields a relatively small correction only.

2.3.2 Relativistic case

For kinetic energy exciting 1 MeV protons have relativistic velocities. Also the flux of solar protons for such energies is relatively small; this case will be considered here. The maximum kinetic energy transfered to the metallic foil electron is estimated by use of the Lorentz transformation of the four-momentum of the incident proton and the metallic electron. The frame of reference moving with velocity v_F will be indicated by upper coma symbol, laboratory frame without any symbol (see Fig. 2.3).

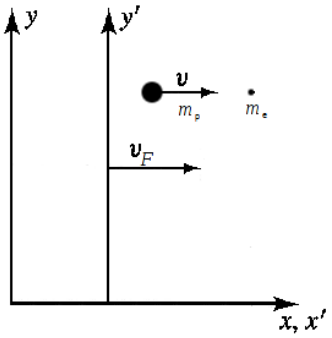

Figure 2.3: The impression of the laboratory frame $x-y$ and a reference frame $x^{'}-y^{'}$ moving with the velocity v_F. In the laboratory frame the incident proton with mass m_p is moving to the electron m_e with velocity v.

The four-momentum $p^\alpha = (E, \vec{p}) = (m_\mathrm{p}\gamma, m_\mathrm{p}\gamma\vec{v})$ [44] in laboratory frame for the incident proton and metallic foil electron is given by, respectively:

$$(m_\mathrm{p}\gamma, m_\mathrm{p}\gamma v, 0, 0), \tag{2.30}$$

$$(m_\mathrm{e}, 0, 0, 0), \tag{2.31}$$

here $\gamma = (1 - v^2/c^2)^{-1/2}$ is the Lorentz factor. Applying Lorentz transformation [44]:

$$x' = \gamma_{\mathrm{F}}(x - v_{\mathrm{F}}t), \tag{2.32}$$

$$t' = \gamma_{\mathrm{F}}\left(t - \frac{v_{\mathrm{F}}}{c^2}x\right), \tag{2.33}$$

where v_F is the velocity of the moving reference frame, $v_F||v$, one can calculate the four-velocity and the four-momentum in the reference frame of the incident proton and the metallic electron, respectively [66] one finds:

$$v' = \gamma_{\mathrm{F}}(v - v_{\mathrm{F}}) \qquad \Rightarrow \qquad (\gamma m_{\mathrm{p}} v)' = \gamma_{\mathrm{F}}(\gamma m_{\mathrm{p}} v - \gamma m_{\mathrm{p}} v_{\mathrm{F}}), \tag{2.34}$$

$$v'_e = \gamma_{\mathrm{F}}(0 - v_{\mathrm{F}}) \qquad \Rightarrow \qquad p'_e = -\gamma_{\mathrm{F}} m_{\mathrm{e}} v_{\mathrm{F}}. \tag{2.35}$$

In the center of momentum frame in which the center of mass is at rest $(\gamma m_{\mathrm{p}} v)' + p'_i = 0$ one can calculate the velocity of the reference frame:

$$v_{\mathrm{F}} = \frac{\gamma m_{\mathrm{p}} v}{m_{\mathrm{e}} + \gamma m_{\mathrm{p}}}. \tag{2.36}$$

The 0-component of the four-momentum of the electron in the laboratory frame is:

$$p^0 = \gamma\left(m_{\mathrm{e}}\gamma_{\mathrm{F}} + \frac{v_{\mathrm{F}}^2}{c^2} m_{\mathrm{e}}\gamma_{\mathrm{F}}\right). \tag{2.37}$$

Assuming that $\gamma m_{\mathrm{p}} \gg m_{\mathrm{e}}$ and taking into account Eq. 2.36 it is $v_{\mathrm{F}} \approx v$ and $\gamma_{\mathrm{F}} \approx \gamma$, hence:

$$p^0 = \gamma^2 m_{\mathrm{e}}\left(1 + \frac{v^2}{c^2}\right). \tag{2.38}$$

The total energy transfered to the electron is:

$$E = \gamma^2 m_{\mathrm{e}} c^2\left(1 + \frac{v^2}{c^2}\right). \tag{2.39}$$

Therefore its kinetic energy is:

$$E_{\mathrm{K}} = E - m_{\mathrm{e}}c^2 = m_{\mathrm{e}}c^2\gamma^2\left(1 + \frac{v^2}{c^2} - \frac{1}{\gamma^2}\right). \tag{2.40}$$

The maximum kinetic energy transferred to the electron by the incident proton is then [66]:

$$E_{\mathrm{K_{max}}} = 2m_{\mathrm{e}}\gamma^2 v^2. \tag{2.41}$$

Now using Eq. 2.41 it is easy to write the logarithm for the energy loss per unit length Eq. 2.20:

$$\ln\left(\frac{\xi_{\mathrm{max}}}{\xi_{\mathrm{min}}}\right) \equiv \ln\left(\frac{E_{\mathrm{K_{max}}}}{\bar{I}_{\mathrm{p}}}\right) = \ln\left(\frac{2\gamma^2 m_{\mathrm{e}} v^2}{\bar{I}_{\mathrm{p}}}\right). \tag{2.42}$$

The exact formula of the energy loss per unit length of incident proton in the quantum-relativistic description is known as the Bethe-Bloch formula [113]:

$$-\frac{dE}{dx} = \frac{n_0}{\pi m_{\mathrm{e}}}\left(\frac{ze^2}{2\epsilon_0 v}\right)^2\left[\ln\left(\frac{2\gamma^2 m_{\mathrm{e}} v^2}{\bar{I}_{\mathrm{p}}}\right) - 2\ln\gamma + \gamma^{-2} - 1\right]. \tag{2.43}$$

The second and the third terms are correction factors that are neglected for low velocities of the incident particles [113]. The Bethe - Bloch formula depends on:

- the velocity of the incident particle. The increase of that velocity decreases the energy loss per unit length.
- charge z of the incident particle (here proton). With an increase of the charges, the loss per unit length increases too.

2.4 Recombination of electrons and protons to Hydrogen

Rausch von Traubenberg and Hahn in 1922 have discovered for the very first time a proton recombination process [116]; they used thin films as targets. Basic aspects of two-electron Auger recombination of low energy ions at surfaces, originally proposed by Shekhter already in 1937, has been described extensively within a probability model by Hagstrum [43]. In 1987, Taute considered variability of Auger recombination rate as a function of an ion velocity. There have been considered small grazing angles [104, 116].

In solids one can distinguish four processes of recombination of incident H^+ ions (protons) with electrons to neutral Hydrogen atoms:

1. the Auger process,
2. the resonant process,
3. Oppenheimer-Brinkman-Kramers (OBK) process,
4. Radiative Electron Capture (REC) process.

Since the solar wind consists mainly of low ($\leq$ 100 keV) energetic protons only the first three processes will be considered in this thesis. The Auger process dominates the total cross section [101]. According to Raisbeck and Yiou [87] for protons the REC process dominates the recombination only above proton energies of about 300 MeV (for Al foil); therefore this process will be not discussed here.

For each of these recombination processes one can calculate the rate Γ of capture (recombination rate) or loss (ionization rate) of an electron. The cross section per atom for each charge exchange process is defined by [84]:

$$\Sigma = \frac{\Gamma}{n_0 v}, \tag{2.44}$$

where v is the ion speed and n_0 is the number density of material ions.

The plan of this section is as follows: first a short introduction to the Hydrogen atom in a classical and quantum approach is made. Next a description of conditions which have influence to the number of free electrons in solids is made. Finally the recombination processes are described.

The Hydrogen atom - quasi-classical approach

The classical description of the Hydrogen atom is based on two assumptions:

1. An electron with mass m_e in an atom orbits with a radius $r_e(n)$ and velocity $v_e(n)$ the proton. n is a number of the shell. The angular momentum is defined as:

$$m_e v_e(n) r_e(n) = n\hbar, \qquad n = \{1, 2, 3, ...\}. \tag{2.45}$$

2. An atom emits a photon of electromagnetic radiation when an electron jumps to lower shell. On the other hand it jumps to higher shell when it absorbs a photon. The energy difference ΔE is proportional to the frequency of the electromagnetic radiation:

$$\Delta E = h\nu. \tag{2.46}$$

Radius, velocity and energy of an electron at the n'th shell are calculated by use of both Bohr's assumptions and the balance of the centripetal and Coulomb forces:

$$r_e(n) = \frac{n^2\hbar^2}{m_e e^2}, \qquad v_e(n) = \frac{e^2}{n\hbar}, \qquad E(n) = -\frac{1}{n^2}\frac{m_e e^4}{2\hbar^2}. \tag{2.47}$$

For $n = 1$, the minimum radius (the Bohr radius) and the energy (the Bohr energy) for an electron are:

$$r_{\text{Bohr}} = \frac{\hbar^2}{m_e e^2} \cong 5.29 \times 10^{-9} \text{ cm}, \qquad \text{E}_{\text{Bohr}} = -\frac{\text{m}_\text{e}\text{e}^4}{2\hbar^2} \cong -13.6 \text{ eV}. \tag{2.48}$$

The Hydrogen atom - quantum approach

In quantumm physics the Hamiltonian of the Hydrogen atom and the Schrödinger equation are:

$$H = -\frac{\hbar^2}{2m_e}\boldsymbol{\nabla}^2 + V(r), \qquad H\psi(r,\theta,\phi) = E\psi(r,\theta,\phi), \tag{2.49}$$

where $V(r)$ is the potential energy, $V(r) = -\frac{e^2}{r}$. The state function is written in spherical coordinates as [95, 103]:

$$\psi(r,\theta,\phi) = \frac{R_{n,l}(r)}{r} Y_{l,m}(\theta,\phi), \tag{2.50}$$

while its angular part is described by spherical harmonics. The radial part fulfills the following ordinary secondary differential equation [95, 103]:

$$\frac{d^2 R_{n,l}(r)}{dr^2} + \left\{ \frac{2m_e}{\hbar^2}\left(E_n + \frac{e^2}{r}\right) - \frac{l(l-1)}{r^2} \right\} R_{n,l}(r) = 0, \qquad l = \{0, 1, 2, ...\}. \tag{2.51}$$

Here l is the orbital quantum number. The energy of an electron at the n'th shell is:

$$E_n = -\frac{1}{n^2}\frac{m_e e^4}{2\hbar^2}, \tag{2.52}$$

which is the same result obtained from classical approach (see Equation 2.47). The radial part of the state function is:

$$\frac{R_{n,l}(r)}{r} = e^{-ik_n r} r^l L_{n+1}^{2l+1}(2k_n r), \tag{2.53}$$

where $k_n = \sqrt{-\frac{2m_e E_n}{\hbar^2}}$ and $L_{n+1}^{2l+1}(x)$ is the Laguerre polynomial:

$$L_{n+1}^{2l+1}(x) = \frac{d^{2l+1}}{dx^{2l+1}} \left\{ e^x \frac{d^{n+l}}{dx^{n+1}} \left(x^{n+l} e^{-x} \right) \right\}. \tag{2.54}$$

A detailed derivation can be found in the standard text books [57, 95, 103].

Number of free electrons in solids

Each solid at given physical conditions (temperature, pressure) has an approximately constant number of free electrons. A possibility to change the number is to irradiate the target by incident particles.

The number of lattice ions per unit volume is:

$$n_0 = \frac{N_A \rho}{M_{\mathrm{u}}}, \tag{2.55}$$

where N_A is the Avogadro's number (6.022×10^{23} mol^{-1}), ρ the density of a given material, M_{u} is the molar mass, it is 27 g mol^{-1} for Aluminum and n_0 is 6.026×10^{22} atoms cm^{-3}.

According to [37] one can estimate a number of free electrons n_e per one lattice atom as a function of conductivity σ:

$$\frac{n_e}{n_0} = \left(\frac{3}{8\pi} \right)^{\frac{1}{2}} \frac{1}{n_0} \frac{h^{\frac{3}{2}}}{e^3} \left(\frac{\sigma}{\bar{l}} \right)^{\frac{3}{2}}, \tag{2.56}$$

Here $\bar{l}$ is the mean free path. The conductivity which is related to the resistivity $\sigma = 1/\varrho$ [37]. The resistivity obeys the Matthiessen's rule (not satisfied for Noble metals: ruthenium, rhodium, palladium, silver, osmium, iridium, platinum and gold) [115]:

$$\varrho_{total} = \varrho(T) + \varrho_{\text{impurities}}(x) + \varrho_{\text{crystal imperfections}}, \tag{2.57}$$

where x is the concentration of impurities. The first term of this formula is given by the Bloch - Grüneisen relation [115]:

$$\varrho(T) = \varrho(0) + A \left(\frac{T}{\Theta} \right) \int_0^{\frac{\Theta}{T}} \frac{x^{n_{\mathrm{i}}}}{(e^x - 1)(1 - e^{-x})} dx. \tag{2.58}$$

Here A is a constant number that depends on a velocity of the electrons at the Fermi surface and the Debye radius and a density of electrons in the meta. Θ is the Debye temperature, n_{i} is an integer, where [13, 115]:

- $n_{\mathrm{i}} = 2$ means that resistivity is determined by electron - electron interactions,
- $n_{\mathrm{i}} = 5$ means that resistivity is determined by scattering of electrons by phonons.

The second component of the Eq. 2.57, $\varrho_{\text{impurities}}(x)$, depends on a type and the concentration x of the impurities. If the target contains a mole fraction x of an element one element and $1-x$ of an another element. The relation $\varrho(x)$ can be described by Nordheim's rule [115]:

$$\varrho(x) \sim x(1-x). \tag{2.59}$$

The rule has been checked experimentally, see Fig. 2.4. One can see the quadratic relation between the resistivity and the percentage of an impurity.

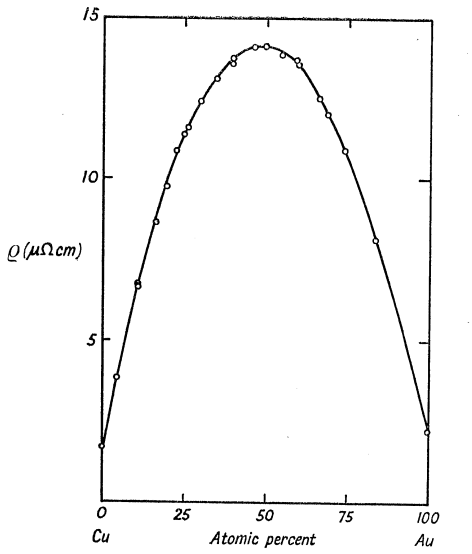

Figure 2.4: The Nordheim's rule, resistivity as a function of the percentage of impurities [115]. The open circles represent measurements; solid curve: the relation $\varrho(x) \sim x(1-x)$.

The third component of the Eq. 2.57 describes the contribution to the resistivity from dislocations:

$$\varrho_D \sim 2.3 \times 10^{-19} N_D \quad [\Omega\text{cm}], \tag{2.60}$$

where N_D is the number of dislocations [115].

2.4.1 Auger recombination

According to [27, 41, 83, 84, 92, 100, 101] in the Auger process, an electron is captured (or lost) by the incident ion to (or from) a bound state with incident ion assisted by a third body, an electron-hole pair. A scheme of the electron-hole Auger process (electron capture) is shown in the Fig. 2.5.

According to Fig. 2.5 one can write the energy conservation of the process as:

$$E_{\text{initial}} = E_{\text{ion}} + E', \tag{2.61}$$

$$E_{\text{final}} = E_{\text{neutral}} + E_{\text{K}}^{\text{e}}, \qquad E_{\text{K}}^{\text{e}} = E_{\text{pot}}^{\text{ion}} - E' - E''. \tag{2.62}$$

Here E_{initial} is the energy of the initial configuration of the system. At the initial state the incident ion is penetrating the target having the total energy of E_{ion}. To recombine it needs

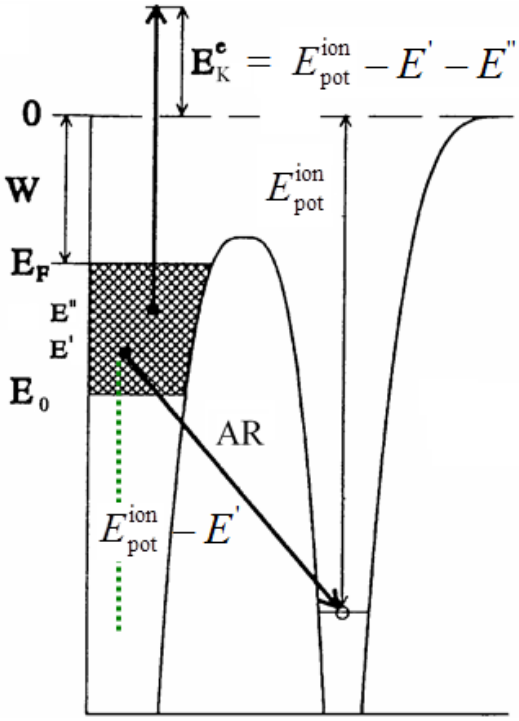

Figure 2.5: Energetic representation of the Auger process. Electrons in the conduction band have energies between E_0 and the Fermi's energy $E_{\rm F}$. W denotes the work function, $E_{\rm pot}^{\rm ion}$ is the potential energy of the incident ion, and $E_{\rm K}^{\rm e}$ is the kinetic energy of the Auger electron.

an electron from the conduction band. The electron has the energy of E'. On the other hand $E_{\rm final}$ is the energy of the final configuration of the system, which is a neutral atom with an energy of $E_{\rm neutral}$ and an ejected electron (an Auger electron) with the kinetic energy of $E_{\rm K}^{\rm e}$.

The plan of the section is as follows: first the Hamiltonian, eigenfunctions and eigenvalues of the Auger process are presented. The probability per unit time of the Auger capture and loss process is calculated by use of a semiclassical approach. Then the probability per unit time will be used to calculate the cross section of the process.

Atomic units are used i.e. $e^2 = \hbar = m_{\rm e} = 1$, the Bohr radius, r_0, is the unit of length. The energy is measured in Hartrees, $1E_{\rm h}$ is 27.211 eV. Vector variables are denoted by use of a bold font. The Hamiltonian of the system is:

$$H = H_0 + H_{\rm I} + \sum_{\rm j} \left(\frac{1}{|\mathbf{r}_{\rm j} - \mathbf{r}_{\rm e}|} - \frac{Z}{|\mathbf{r}_{\rm j} - \mathbf{R}_{\rm I}|} \right), \tag{2.63}$$

where H_0 is the Hamiltonian of the electron gas, $\mathbf{r}_{\rm j}$ denotes the vector components of the $\rm j^{th}$ electron of the gas; $\mathbf{R}_{\rm I}$ are the vector components of the ion, and $\mathbf{r}_{\rm e}$ denotes the vector components of the electron in the ion-electron composite [26]. The schematic representation of the system is shown in the Fig. 2.6.
$H_{\rm I}$ is the Hamiltonian of the ion-electron composite:

$$H_{\rm I} = -\frac{1}{2M}\boldsymbol{\nabla}^2_{\mathbf{R}_{\rm I}} - \frac{1}{2}\boldsymbol{\nabla}^2_{\mathbf{r}_{\rm e}} - \frac{Z}{|\mathbf{R}_I - \mathbf{r}_e|}. \tag{2.64}$$

In Eq. 2.63 the term

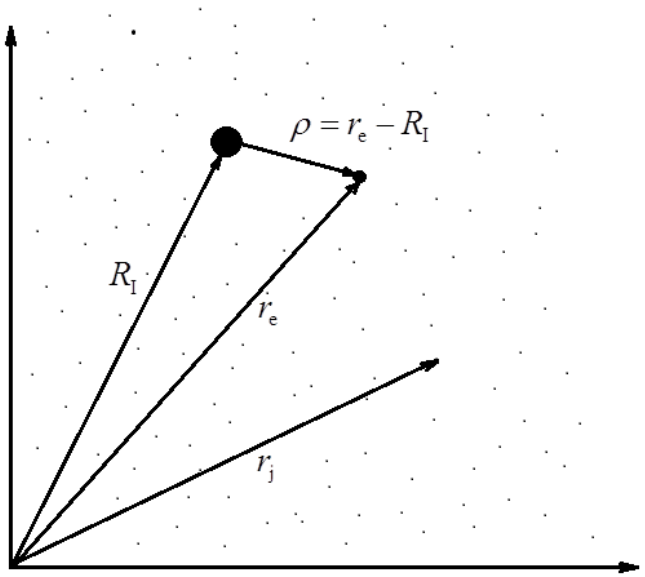

Figure 2.6: Graphical 2-D projection of the 3-D system: ion-electron and electron gas, $\mathbf{R}_\mathrm{I}$ is the position of the incident ion, $\mathbf{r}_\mathrm{e}$ the position of the captured electron, $\mathbf{r}_\mathrm{j}$ the position of the j^{th} electron in the gas, and $\boldsymbol{\rho}$ is the distance between the ion and the electron.

$$\sum_{\mathrm{j}} \left(\frac{1}{|\mathbf{r}_\mathrm{j} - \mathbf{r}_\mathrm{e}|} - \frac{Z}{|\mathbf{r}_\mathrm{j} - \mathbf{R}_\mathrm{I}|} \right), \tag{2.65}$$

describes the interaction between the electron gas and the ion-electron pair [26]. The eigenfunctions of H_I are given by:

$$\mid i\rangle = e^{i\mathbf{k}_0 \cdot \mathbf{R}} u_0(\boldsymbol{\rho}), \tag{2.66}$$

with stationary Schroedinger equation:

$$H_\mathrm{I} \mid i\rangle = E_\mathrm{i} \mid i\rangle, \tag{2.67}$$

and the eigenvalues

$$E_\mathrm{i} = \frac{k_0^2}{2(M+1)} + \omega_0, \tag{2.68}$$

where

$$\mathbf{R} = \frac{\mathbf{r}_\mathrm{e} + M\mathbf{R}_\mathrm{I}}{1+M}, \tag{2.69}$$

represents the coordinates of the center of mass, $\mathbf{k}_0$ the total momentum of the composite, and $u_0(\boldsymbol{\rho})$ the wave function describing the relative motion of the electron in the composite with respect to the ion, i.e., $\boldsymbol{\rho} = \mathbf{r}_\mathrm{e} - \mathbf{R}_\mathrm{I}$ with the binding energy of ω_0 [26].

The physical description begins with the Poisson's equation for the scalar electric potential $\phi(\mathbf{r}, t)$ generated at position $\mathbf{r}$ and time t by the charge density $\varrho_c(\mathbf{r}, t)$ in a medium, that is characterized by a causal dielectric constant ϵ [26]:

$$\epsilon \boldsymbol{\nabla}^2 \phi = -4\pi \varrho_{\rm c}(\mathbf{r}, t). \tag{2.70}$$

An incident particle with charge Z may be considered to give rise to a charge density $\varrho_{\rm c}(\mathbf{r}, t) = Z\delta(\mathbf{r} - \mathbf{v}t)$ [26]. To write the equation in the momentum space, one has to use the Fourier transformation:

$$f(\mathbf{q}, \omega) = \int \frac{d^3q}{(2\pi)^3} \int_{-\infty}^{\infty} d\omega \; e^{-i(\mathbf{q}\cdot\mathbf{r} - \omega t)} f_{\mathbf{r},t}, \tag{2.71}$$

where $\mathbf{q}$ is the momentum and ω the energy. Thus the density is $\varrho_{\mathbf{q},\omega} = 2\pi Z\delta(\omega - \mathbf{q}\cdot\mathbf{v})$. By use of Eqs. 2.70 and 2.71 one can calculate the scalar potential:

$$\phi_{\mathbf{q},\omega} = \frac{4\pi \varrho_{\rm c}(\mathbf{q}, \omega)}{q^2 \epsilon(\mathbf{q}, \omega)}. \tag{2.72}$$

An incident particle moving through the target with velocity $\mathbf{v}$ induces an electric field, whose scalar potential is given by [27]:

$$\phi^{\rm ind}_{\mathbf{q},\omega} = \frac{8\pi^2 Z}{q^2} \delta(\omega - \mathbf{q}\cdot\mathbf{v}) \left(\frac{1}{\epsilon(\mathbf{q}, \omega)} - 1 \right). \tag{2.73}$$

When an incident particle is passing through the matter, the induced potential around the moving ion deviates from the spherical symmetry. For a charge at rest this potential is spherically symmetric, but as its velocity increases the potential loses this symmetry. A strong modification of this type should create an important effect to the state of the electron which is bound to the ion [41]. Additionally, at the end of the subsection this effect will be presented by use of the wave function $u_0(\boldsymbol{\rho})$ which describes the relative motion of the electron in the ion-electron composite .

The rate of energy loss per unit time of the incident particle $\frac{dE}{dt}$ is obtained from the induced electric field $\mathbf{E}^{\rm ind} = -\boldsymbol{\nabla}\phi^{\rm ind}$ [26]:

$$\frac{dE}{dt} = -Z\mathbf{v}\cdot\mathbf{E}^{\rm ind}(\mathbf{r}, t). \tag{2.74}$$

According to [26] one can write the energy loss as:

$$\frac{dE}{dt} = \int \frac{d^3q}{(2\pi)^3} \int_0^{\infty} \frac{d\omega}{2\pi} \; 2\omega Z {\rm Im}(-\phi^{\rm ind}_{\mathbf{q},\omega}) \tag{2.75}$$

It is taken only the imaginary part of the potential, i.e. imaginary part of the dielectric function: ${\rm Im}\left(-\frac{1}{\epsilon(\mathbf{q},\omega)}\right)$. According to Jackson [49] the imaginary part of ϵ represents the energy dissipation of an electromagnetic wave in the medium. If ${\rm Im}(\epsilon) < 0$ then energy is transfered from the media to the wave. $\frac{dE}{dt}$ can also be written in much more suitable form [26]:

$$\frac{dE}{dt} = \int dx \; \omega\Gamma(\mathbf{q}, \omega), \qquad \int dx \equiv \int \frac{d^3q}{(2\pi)^3} \int_0^{\infty} \frac{d\omega}{2\pi}, \tag{2.76}$$

where $\Gamma(\mathbf{q}, \omega)$ is the probability per unit time that the initial ion loses energy ω and momentum $\mathbf{q}$ [26] ($\mathbf{q}$ and ω represent the momentum and energy transferred to the solid by an incident particle [92]):

$$\Gamma(\mathbf{q},\omega) = 2Z\mathrm{Im}(-\phi^{\mathrm{ind}}_{\mathbf{q},\omega}) = \frac{16\pi^2 \mathrm{Z}^2}{\mathrm{q}^2}\mathrm{Im}\left(-\frac{1}{\epsilon(\mathbf{q},\omega)}\right)\delta(\omega - \mathbf{q}\cdot\mathbf{v}). \tag{2.77}$$

Note that the energy loss per unit length dx can be written immediately by use of the Eq. 2.76:

$$\frac{dE}{dx} = \frac{1}{v}\int dx\ \omega\Gamma(\mathbf{q},\omega). \tag{2.78}$$

To adopt the result of Eq. 2.77 to the Auger process one has to consider a few corrections:

1. When an incident particle captures an electron that lies inside the Fermi sphere $\mid \mathbf{k}+\mathbf{v} \mid < k_F$, where $\mathbf{k}$ is the momentum of the electron, k_F is the Fermi's wave number. On the other hand when the particle loses an electron, an electron-hole pair is created, and $\mid \mathbf{k}+\mathbf{v} \mid > k_F$. One can clearly imagine this situation considering the Fig. 2.5. Thus the first multiplication correction factor to Eq. 2.77 is:

$$\Theta(\pm k_{\mathrm{F}} \mp \mid \mathbf{k}+\mathbf{v} \mid), \tag{2.79}$$

   where $\Theta(x)$ is the step function, $\Theta(x) = 1$ when $x \geq 0$, and $\Theta(x) = 0$ when $x < 0$. Upper signs $(+/-)$ denote capture of an electron by incident ion, while lower signs $(-/+)$ loss of the electron.

2. If one looks carefully to the energy conservation of the process, Eqs. 2.61 and 2.62, it is obvious that in each single process the energy of the ejected Auger electron could be different, it mainly depends on the energy of the incident ions. Also the energy of the bound to the incident ion-electron could be different because it is inside the Fermi sphere having an energy waring in the range of E_0 to E_{F}.

   The recombination will proceed more rapidly if the coupling between the initial and final states is stronger. This coupling term is traditionally called the *matrix element*: $\langle f \mid \hat{A} \mid i\rangle$. The matrix element can be placed in the form of an integral, where the interaction which causes the process is expressed as an operator $\hat{A}$ which acts on the initial state wavefunction. The recombination probability is proportional to the square of the integral. This kind of approach using the wavefunctions is of the same general form as that used to find the *expectation value* of any physical variable in quantum mechanics [47]. Here the initial eigenstate $|i\rangle$ is described by use of the $u_0(\boldsymbol{\rho})$ wave function; final eigenstate $\langle f|$ by use of OPW (Orthogonal Plane Wave) function $\mid \mathbf{k}_{\mathrm{OPW}}\rangle = \mid e^{i\mathbf{k}\cdot\boldsymbol{\rho}}\rangle - \langle u_0(\boldsymbol{\rho}) \mid e^{i\mathbf{k}\cdot\boldsymbol{\rho}}\rangle \mid u_0(\boldsymbol{\rho})\rangle$ [26]. An OPW is defined as a plane wave which has been made orthogonal to Bloch waves by use of the Schmidt process [1, 16, 46]. OPW describes the state of an electron in the conduction band in solids [26]; the method was proposed by Herring in 1940 [46]. In the literature one can find also the method proposed by Wigner and Seitz [108] which gives good results for lower states of the valence electron band of a metal, but the extension of this method to states of higher energy becomes rapidly more unreliable as the energy increases [26]. Here $\hat{A}$ is an operator for the physical interaction which couples the initial and final states of the system; $\hat{A}$ is here $e^{\pm\mathbf{k}\cdot\boldsymbol{\rho}}$. Thus the second multiplication correction factor is:

$$\mid \langle \mathbf{k}_{\mathrm{OPW}} \mid e^{\pm\mathbf{k}\cdot\boldsymbol{\rho}} \mid u_0(\boldsymbol{\rho})\rangle \mid^2 . \tag{2.80}$$

Upper sign (+) denotes capture of an electron by the incident ion, while lower sign (−) loss of the electron.

3. Also one has to modify the δ function. The correction takes into a account captured or an ejected electron [26]:

$$\delta(\omega - \mathbf{q}\cdot\mathbf{v} \mp \frac{k^2}{2} \pm \omega_0) \tag{2.81}$$

Upper signs (−/+) denotes capture of an electron by the incident ion, while lower signs (+/−) loss of the electron.

Thus the probability per unit time of electron capture or loss in the Auger process is [27, 83, 92, 100, 101]:

$$\begin{aligned}\Gamma_{\mathrm{A}}^{\mathrm{C,L}} = & \int \frac{d^3q}{(2\pi)^3}\int_0^\infty \frac{d\omega}{2\pi}\int \frac{d^3k}{(2\pi)^3}\,\Theta(\pm k_{\mathrm{F}} \mp \mid \mathbf{k}+\mathbf{v}\mid) \\ & \frac{16\pi^2 Z^2}{q^2}\mathrm{Im}\left(-\frac{1}{\epsilon(\mathbf{q},\omega)}\right)\delta(\omega - \mathbf{q}\cdot\mathbf{v} \mp \frac{\mathrm{k}^2}{2} \pm \omega_0) \\ & \mid \langle \mathbf{k}_{\mathrm{OPW}} \mid e^{\pm\mathbf{k}\cdot\boldsymbol{\rho}} \mid u_0(\boldsymbol{\rho})\rangle \mid^2 .\end{aligned} \tag{2.82}$$

By use both Eqs. 2.44 and 2.82 one can easily calculate the cross section of the Auger process, both for losing and capturing of an electron.

According to [26, 41] the bound state wave function (the wave function describing the relative motion of the electron in the composite with respect to the ion) is assumed to be of the form:

$$u_0(\boldsymbol{\rho}) = \left(\frac{a^3}{\pi}\right)^{\frac{1}{2}} \exp(-a\boldsymbol{\rho}). \tag{2.83}$$

Guinea et al. [41] have calculated the wave functions and the binding energies, ω, of the first and second electron bound to H. Results are presented in the Table 2.1.

One can calculate the probability amplitude by use of well-known formula $\Pi \sim \mid u_0(\boldsymbol{\rho}) \mid^2$. Here Π predicts the position where the bound (to the incident ion) state is most probable. Results are presented in Fig. 2.7 where the incident particle is a proton. The left plot shows the situation where the first electron is bound to the proton; while in the right plot the second electron is bound to the H atom. The amplitude $\mid u_0(\boldsymbol{\rho}) \mid^2$ is plotted as a function of the distance (Y axis, in a.u.) from the incident proton or H atom and of the energy of the incident proton or H atom (X axis, in keV).

It is obvious that the smaller the distance to the incident proton or H atom, the higher is the probability of a recombination event. While the kinetic energy energy of the incident H is much smaller than for proton.

2.4.2 Resonant recombination

The incident ion is recombined with an electron which is tunneled to the metastable state [43], see Fig 2.8. The inverse process is also possible. An electron which is in a metastable state with respect to the metallic ion can populate one of the free electron states of the metal

E	First Electron		Second Electron	
keV	a	ω [a.u.]	a	ω [a.u.]
0	0.90	-0.106	0.76	-0.046
1.0	0.88	-0.096	0.072	-0.036
4.0	0.86	-0.075	0.76	-0.012
9.0	0.80	-0.048	0.54	-0.004
16.0	0.72	-0.027	0.52	-0.009
25.0	0.74	-0.027	0.58	0.010
36.0	0.82	-0.041	0.70	0.011
49.0	0.86	-0.063	0.74	0.011
64.0	0.90	-0.096	0.74	0.006
81.0	0.92	-0.125	0.72	0.005
100.0	0.94	-0.184	0.72	0.001

Table 2.1: Binding energies (ω in a.u.) and values of the parameter a defining the wave function for proton (first column) and H atom (second column) as a function of the energy, E, of the incidence ion. Binding energies are referred to the bottom of the conduction band [26].

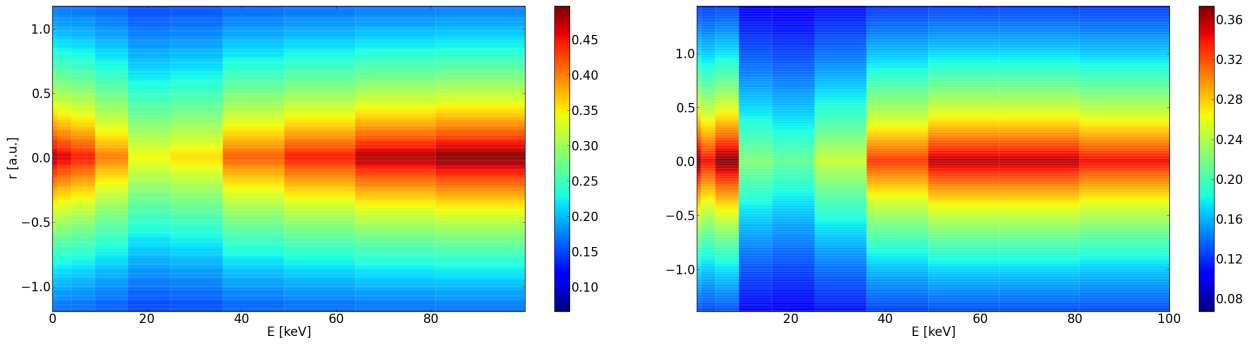

Figure 2.7: Left plot, first electron is bound to the H^+. Right plot, second electron is bound to the H atom. The density of probability is plotted as a function of the distance (Y axis, in a.u.) and the kinetic energy E of the incident ion (X axis, in keV). The amplitude is color-coded.

only if it become free (the Pauli exclusion principle). The shift of the energy levels is due to the electric field.

The effect comes from the crystal structure itself. The resonant processes are due to the potential seen by the moving ion i.e. they are described in a frame where the ion is at rest [100]. From the point of view of the ion, there appears a moving periodic potential which gives rise to transitions between bound states of the composite and free electron states [26]. The potential seen by the ion can be written as follows:

$$V(\mathbf{r},t) = \sum_{\mathbf{G}} V(\mathbf{G}) e^{i\mathbf{G}(\mathbf{r}\mp\mathbf{v}t)}, \tag{2.84}$$

here $\mathbf{G}$ is the reciprocal vector of the lattice, and $V(\mathbf{G})$ is assumed to be the Hartree potential created by all the charges of the crystal, the $\mp$ sign denotes that the periodic potential recedes $(+)$ from or approaches $(-)$ to the ion [100]. The idea of the Hartree approximation and

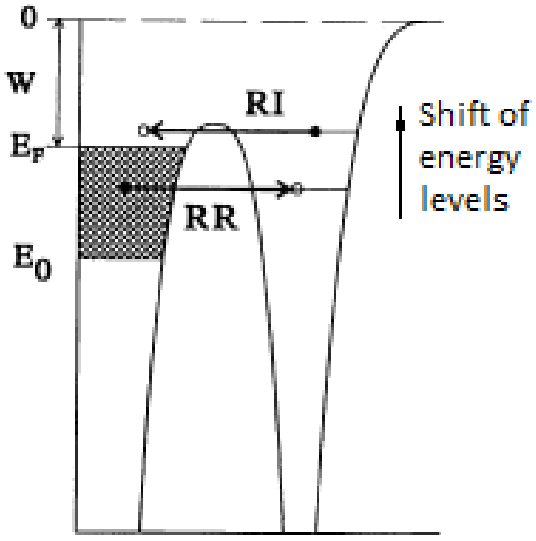

Figure 2.8: Energetic representation of resonant recombination. Electrons from the conduction band have energies between E_0 and the Fermi energy E_F. W is the work function, RR denotes the resonant recombination and RI inverse ionization process.

potential is presented in Appendix A.1. By use of the Fourier transformation the Eq. 2.84 also could be written as [101]:

$$V(\mathbf{r},\omega) = 2\pi \sum_{\mathbf{G}} V(\mathbf{G}) e^{i\mathbf{G}\cdot\mathbf{r}} \delta(\omega \pm \mathbf{G}\cdot\mathbf{v}), \tag{2.85}$$

The potential $V(\mathbf{r},\omega)$ is seen by the moving ion as a frequency - dependent perturbation which contributes to the capture and loss processes. The perturbation induces transitions between the atomic bound state and the free-electron levels of the metal [101]. As in the Auger recombination process one has to consider a few corrections to get the formula of the probability per unit time of the process.

1. First of all, the probability per unit time is proportional to the square root of the *matrix element* $\langle f \mid \hat{A} \mid i \rangle$ of the process. Here the initial state of the system $|i\rangle$ is described by use of the $u_0(\boldsymbol{\rho})$ wavefunction. An electron bound to the incident ion is considered as the initial state. The valence electron state is described by an OPW wave function $|\mathbf{k}_{\mathrm{OPW}}\rangle$. In the rest frame of the ion, the momentum $\mathbf{k}_e$ of the valence electron is given by $\mathbf{k}' - \mathbf{v}$, where $\mathbf{k}'$ is the momentum in the laboratory frame. First of all one has to find the correct form of the operator $\hat{A}$:

$$\begin{aligned} \langle u_0(\boldsymbol{\rho}) \mid 2\pi \sum_{\mathbf{G}} V(\mathbf{G}) e^{i\mathbf{G}\cdot\boldsymbol{\rho}} \delta(\omega + \mathbf{G}\cdot\mathbf{v}) \mid \mathbf{k}_{\mathrm{OPW}} \rangle \quad &= \\ 2\pi \sum_{\mathbf{G}} \langle u_0(\boldsymbol{\rho}) \mid V(\mathbf{G}) e^{i\mathbf{G}\cdot\boldsymbol{\rho}} \mid \mathbf{k}_{\mathrm{OPW}} \rangle \; \delta(\omega + \mathbf{G}\cdot\mathbf{v}). & \end{aligned} \tag{2.86}$$

The probability per unit time of the process is proportional to the square root of the *matrix element*:

$$\Gamma_{\mathrm{R}}^{\mathrm{L}} \sim 2\pi \sum_{\mathbf{G}} \mid V(\mathbf{G}) \mid^2 \mid \langle u_0(\boldsymbol{\rho}) \mid e^{i\mathbf{G}\cdot\boldsymbol{\rho}} \mid \mathbf{k}_{\mathrm{OPW}} \rangle \mid^2 \delta(\omega + \mathbf{G}\cdot\mathbf{v}), \tag{2.87}$$

The matrix element describe the electron loss only.

2. The δ function in Eq. 2.87 has to be modified. The correction should take into account whether an electron is captured or ejected [27]:

$$\delta(\omega - \frac{1}{2}\mathbf{k}_{\mathrm{e}}^2 \mp \mathbf{G}\cdot\mathbf{v}) \tag{2.88}$$

Upper sign $(-)$ denotes the capture of an electron by the incident ion, while lower sign $(+)$ corresponds to the loss of an electron.

3. When an incident particle loses an electron, an electron-hole pair is created, thus $\mid \mathbf{k}_{\mathrm{e}} + \mathbf{v} \mid > k_{\mathrm{F}}$. On the other hand, when an incident particle captures an electron it lies inside the Fermi sphere, $\mid \mathbf{k}_{\mathrm{e}} + \mathbf{v} \mid \leq k_{\mathrm{F}}$. As in the Auger recombination process one has to use the $\Theta(x)$ step function:

$$\Theta(\pm k_{\mathrm{F}} \mp \mid \mathbf{k}_{\mathrm{e}} + \mathbf{v} \mid), \tag{2.89}$$

Upper signs $(+/-)$ denote capture of an electron by incident ion, while lower signs $(-/+)$ loss of the electron.

Collecting all these information together one can write the probability per unit time of the resonant recombination process as [26, 27, 84, 92, 100, 101]:

$$\begin{aligned} \Gamma_{\mathrm{R}}^{\mathrm{C,L}} = {} & 2\pi \int \frac{d^3k}{(2\pi)^3}\, \Theta(\pm k_{\mathrm{F}} \mp \mid \mathbf{k}_{\mathrm{e}} + \mathbf{v} \mid)\, \delta(\omega_0 - \frac{1}{2}\mathbf{k}_{\mathrm{e}}^2 \mp \mathbf{G}\cdot\mathbf{v}) \\ & \sum_{\mathbf{G}} \mid V(\mathbf{G}) \mid^2 \mid \langle u_0(\boldsymbol{\rho}) \mid e^{i\mathbf{G}\cdot\boldsymbol{\rho}} \mid \mathbf{k}_{\mathrm{OPW}} \rangle \mid^2, \end{aligned} \tag{2.90}$$

The cross section of this process as well as a comparison with other recombination processes is presented in the Section 2.4.4.

2.4.3 Oppenheimer - Brinkman - Kramers (OBK) Process

The OBK process is a capture process, where an inner or outer shell electron of a target atom is transferred to the moving ion [100]. In the literature one can find a lot of physical approaches [4, 12, 15, 20, 24, 25, 31, 34, 35, 60, 63, 79]. Different results may be obtained depending on the approximation applied to the wave functions and the energy levels involved in the process [27].

This thesis presents one of them, the author's modification of so-called *model-potential OBK* approximation (MPOBK), the $1s$-$1s$ capture. The modification assumes that the mass of the incident ion is much lower then the mass of the target's atom. That is exact the situation when the metal sample is bombarded by protons. The transition electron caught by the incident proton is considered as the active electron. The other electrons are considered to be the passive ones [27]. In the OBK process the outer-shell electrons of the metal ions

experience a strong Coulomb field of the incident ion. The electronic wave function of the electrons is distorted [55, 56]. For the inner-shell capture, the screening effect of the outer-shell electrons of the metallic ions reduces the capture probability of an active electron by the incident proton [10, 55, 109]. The geometry of the process is shown below. Note that the vectors: $\mathbf{r}$, $\mathbf{r}_1$, $\mathbf{r}_2$ and $\mathbf{R}$ are parallel shifted. This is done to show clearly the position of each single vector.

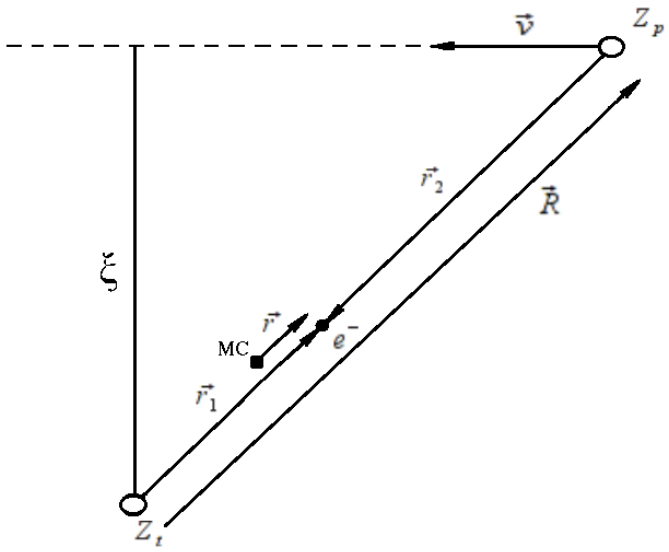

Figure 2.9: Z_p is the charge of the incident ion, Z_t is the charge of the target atom, ξ is the impact parameter, $\mathbf{v}$ is the velocity of the incident proton, $\mathbf{r}_1$ is the position of the active electron relative to the target atom and $\mathbf{r}_2$ is the position of the electron relative to the incident ion, $\mathbf{r}$ is the position vector of the electron relative to the mass center of the target atom and the incident ion, $\mathbf{R}$ is the position vector of the incident ion relative to the target atom, MC is the position of the center of mass.

The best choice of an effective potential, which is felt by the active electron, should be an experimentally found ionization potential [25]. For the multielectron targets it is a standard procedure to work with hydrogenic wave functions corresponding to an effective target charge [25]. The effective potential is given by:

$$V_\mathrm{S} = -\frac{1}{r_1} - \frac{(Z_\mathrm{t}-1)}{r_1}\exp(-Cr_1). \tag{2.91}$$

C is wavenumber tabulated specific for each element. The *model-potential* approximation neglects the core-core interaction. Atomic units are used again. In the initial state, the active electron is in the $1s$ orbital, the electronic wave function is:

$$\phi_\mathrm{i}(\mathbf{r}_1) = \pi^{-\frac{1}{2}}\alpha^{\frac{3}{2}}\exp(-\alpha\mathbf{r}_1), \tag{2.92}$$

where α is the variation parameter which, in fact, contains the screening effect of the passive electrons [55]. The Hamiltonian of the active electron is:

$$H = -\frac{1}{2}\boldsymbol{\nabla}^2 - \frac{1}{r_1} - \frac{(Z_\mathrm{t}-1)}{r_1}\exp(-Cr_1). \tag{2.93}$$

By use of the concept of the average energy $E(\alpha, C) = \langle \phi_{\mathrm{i}}(\mathbf{r}_1) \mid H \mid \phi_{\mathrm{i}}(\mathbf{r}_1) \rangle$ one can calculate the experimental ionization potential I_{K} of the K shell. The detailed derivation is given in Appendix A.2. The potential is:

$$E(\alpha, C) = -I_{\mathrm{K}} = \frac{1}{2}\alpha^2 - \alpha - 4(Z_{\mathrm{t}} - 1)\frac{\alpha^3}{(C + 2\alpha)^2} \tag{2.94}$$

One can compare the model with data which are available in the literature [97, 98]. In Fig. 2.10 the ionization energy of an electron in the *1s* state is shown as a function of atomic number Z of the target atom. One can see that for metals, e.g. Al(13) ($\pm$ 0.023 keV), Fe(26) ($\pm$ 0.028 keV) or Cu(29) ($\pm$ 0.045 keV), the here derived MPOBK result fit very well to the experimental data.

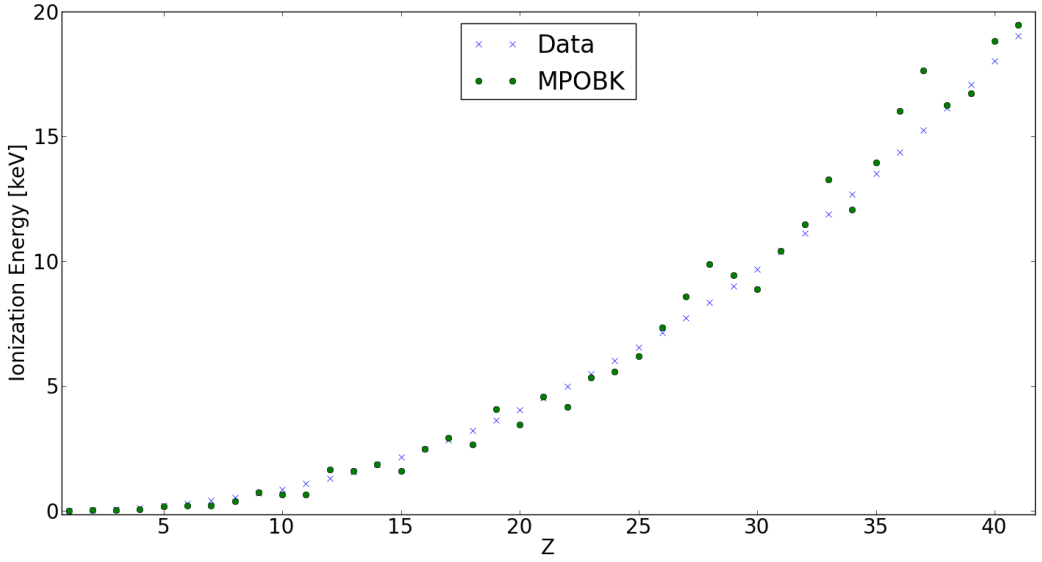

Figure 2.10: Measured (x) and calculated (o) ionization energies of electron in *1s* state as a function of target atomic number Z [97, 98].

The procedure to get the model values looks as follows: for each nucleus one has to find a pair α and C that the value of the Eq. 2.94 is comparable to the experimental one.

After the recombination, the electron is in the $1s$ orbital of the incident proton, the wave function of the electron then is:

$$\phi_{\mathrm{f}}(\mathbf{r}_2) = \pi^{-\frac{1}{2}} Z_{\mathrm{p}}^{\frac{3}{2}} \exp(-Z_{\mathrm{p}}\mathbf{r}_2). \tag{2.95}$$

After a transformation into the center of mass frame the initial and final state functions are:

$$\psi_{\mathrm{i}}(\mathbf{r}_1, t) = \phi_{\mathrm{i}}(\mathbf{r}_1) \exp\left(-ip\mathbf{v}\cdot\mathbf{r} - i\frac{1}{2}p^2v^2t\right), \tag{2.96}$$

$$\psi_{\mathrm{f}}(\mathbf{r}_2, t) = \phi_2(\mathbf{r}_2) \exp\left[i(1-p)\mathbf{v}\cdot\mathbf{r} - i\frac{1}{2}(1-p)^2v^2t\right]. \tag{2.97}$$

Here $\mathbf{r}$ is the position of the electron relative to the center of mass, $\mathbf{v}$ is the velocity vector of the incident ion in the laboratory frame, and $p = m_\mathrm{p}/(m_\mathrm{p} - m_\mathrm{t})$. It is assumed that the incident ion moves along the path with the impact parameter ξ [55]. The relation between the position vectors of the electron are: $\mathbf{r}_1 = \mathbf{r} + p\mathbf{R}$, $\mathbf{r}_2 = \mathbf{r} - (1-p)\mathbf{R}$, where $\mathbf{R}$ is the position vector of the incident ion to the target atom, $\mathbf{R} = \boldsymbol{\xi} + \mathbf{v}t$.

Up to now the case of the incident ion (here proton) is much smaller than mass of ions that form metal has not been considered in the literature. Therefore in this thesis the case of a small parameter p (Eqs. 2.96 and 2.97) will be studied - the more because such a situation is realized when metallic surfaces are exposed to the protons of the solar wind. For Aluminum as a target and proton as an incident ion the parameter is $p \approx 0.036$. Hence it could be set to zero. Thus the wave functions are:

$$\psi_\mathrm{i}(\mathbf{r}_1, t) \cong \phi_\mathrm{i}(\mathbf{r}_1), \tag{2.98}$$

$$\psi_\mathrm{f}(\mathbf{r}_2 = \mathbf{r} - \mathbf{R}, t) \cong \phi_2(\mathbf{r}_2 = \mathbf{r} - \mathbf{R}) \times \exp\left[i\mathbf{v}\cdot\mathbf{r} - \frac{i}{2}v^2 t\right]. \tag{2.99}$$

By use of the scattering amplitude A [55] which is related to the effective potential V_S Eq. 2.91 one can calculate the cross section of the process [25]:

$$A(b) = \frac{1}{i}\int_{-\infty}^{\infty} dt\ \langle\psi_\mathrm{f} \mid V_\mathrm{s} \mid \psi_\mathrm{i}\rangle, \tag{2.100}$$

$$\Sigma \sim \int_0^\infty db\ \mid A(b) \mid^2 b \sim v^{-12}. \tag{2.101}$$

A detailed derivation of this relation is presented in Appendix A.3. The cross section depends strongly on the velocity of the incident proton. Note that a similar velocity dependency of the cross section has been evaluated by Kuang [55]. He has investigated a general model where heavy ions can be used as incident particles. Therefore the p parameter cannot be set to zero.

For too low kinetic energies of the incident proton the active electron at $1s$ state is screened by a cloud of electrons, and the incident proton has not enough energy to pass through a potential barrier. It is then neutralized by another recombination process, e.g. Auger recombination. Also when the kinetic energy of the incident proton is too high, the proton passes the electron cloud of the metal ion without a recombination event; the velocity of proton is so large that it has no time to catch an electron.

2.4.4 Summary

To compare all of the capture (Auger, resonant and OBK) and loss (Auger, resonant) processes one can imagine a simple experiment. Protons with the initial energy of E_p are generated by a proton gun and shoot to a thin metallic foil. A detector which is located behind the foil collects the ions: H^+, H^- and neutral hydrogen atoms H. To separate beams the magnetic field $\mathbf{B}$ can be applied. The scheme of the experiment is shown in Fig. 2.11.

The selection of ions and neutral hydrogen atoms is collected by the detector corresponding to the capture and loss processes that appear in the foil. The state of the charge fractions of the three components of the beam after penetrating the foil, negative ions (H^-) neutral atoms (H) and protons (H^+), can be described in terms of electron -capture an -loss rates Γ (probabilities per unit time) [84]. The fractions are given by [84]:

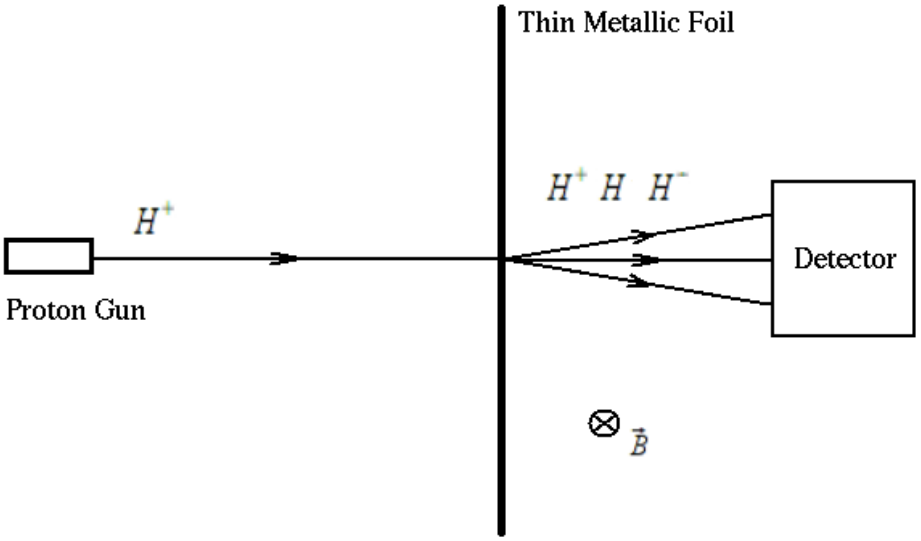

Figure 2.11: Thin metallic foil is irradiated by protons. Capture and loss processes take place inside the foil. Ions and neutral hydrogen atoms are registered by the detector. Beams are deflected by the magnetic field **B**.

$$\begin{aligned} \phi^+ &= \Gamma^{\mathrm{L}}(H)\Gamma^{\mathrm{L}}(H^-)D^{-1}, \\ \phi^0 &= \Gamma^{\mathrm{L}}(H^-)\Gamma^{\mathrm{C}}(H^+)D^{-1}, \\ \phi^- &= \Gamma^{\mathrm{C}}(H^+)\Gamma^{\mathrm{C}}(H^0)D^{-1}, \end{aligned} \tag{2.102}$$

where:

$$D = \Gamma^{\mathrm{L}}(H)\Gamma^{\mathrm{L}}(H^-) + \Gamma^{\mathrm{L}}(H^-)\Gamma^{\mathrm{C}}(H^+) + \Gamma^{\mathrm{C}}(H^+)\Gamma^{\mathrm{C}}(H). \tag{2.103}$$

They dynamics of capturing and loosing electrons during the incident proton penetrate of foil is described in terms of rates $\Gamma^{\mathrm{L,C}}$. Here $\Gamma^{\mathrm{L}}(H)$ and $\Gamma^{\mathrm{L}}(H^-)$ are the probabilities per unit time for the first and second electron loss, while $\Gamma^{\mathrm{C}}(H^+)$ and $\Gamma^{\mathrm{C}}(H)$ are the probabilities per unit time for the first and second electron capture, respectively [84].

Now by use of Eqs. 2.44 and 2.102 theory and experiment can be compared: left hand side of the set of Eq. 2.102 comes from experiment, while right hand side from theoretical models. For experiments the fractions of protons, neutral Hydrogen atoms, and negative ions are obtained. Then by use of Eq. 2.102 the corresponding rates are calculated. Having the rates and knowing the velocity of incident protons the corresponding cross sections can be calculated form Eq. 2.44.

Two plots in the Fig. 2.12 show the different cross sections both for capture and loss when Aluminum is irradiated with protons H^+/Al as a function of proton kinetic energy given in keV [101]. One can see that for a capture of an electron (upper plot) that the Auger process Σ_{A} is a dominant one. The resonant process has negligible contribution to the total cross section. The OBK process (in the literature it is often called the "shell process") gives the main contribution to the total cross section beyond some MeV, depending on the material

used as a target [87]. There is also one capture process which was not described in the thesis, it is called the Radiative Electron Capture (REC). For Aluminum it predicts to be the dominant cross section above a proton energy of $\sim$ 300 MeV and e.g. for Mylar above $\sim$ 125 MeV [87]. In this energy range a flux of solar protons at $\sim$ 1 AU is very small.

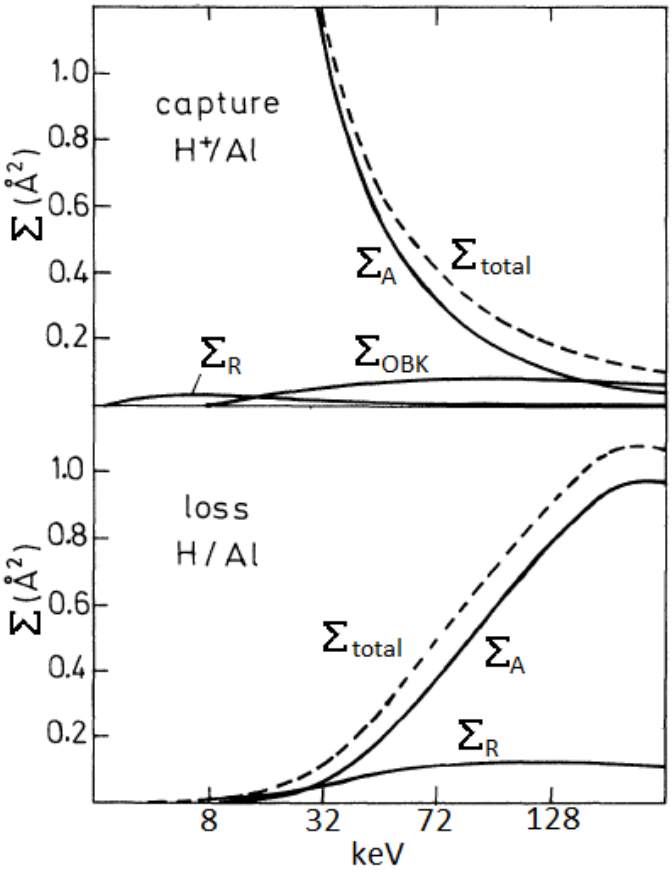

Figure 2.12: Top plot, cross sections for capture processes of H^+ ion: Auger (Σ_A), resonant (Σ_R) and OBK process (Σ_{OBK}). Lower plot, cross sections for loss processes of Hydrogen atom: Auger and resonant process. The dashed line represents the total cross section Σ_{total} of all of the processes.

The theory presented in the previous subsections was tested by many scientific groups e.g. [26, 27, 84, 87, 92, 100]. Experimental facts clearly show that considered capture and loss processes adequately describe the nature of charge fluctuation phenomena which appear inside bombarded material. For majority of the solar protons for which the kinetic energy is lower than 100 keV, the Auger process leads the recombination. The maximum contribution of the OBK process to the total cross section is located in a kinetic energy range exceeding few MeV where solar proton flux is already smaller than that below 100 keV.

Chapter 3

Degradation of materials under space conditions

3.1 An overview of degradation processes

3.1.1 Positive electric charging of foils due to irradiation

The surface of the sail-craft will lose electrons and become positively charged by ionization. This can be caused by the photoelectric effect, by Compton scattering and/or by electron - positron pair production when high energy photons hit metallic surfaces [54]. For instance electrons may be ejected from the surface by the Auger process (see Section 2.4.1). Part of the electron flux will escape from the sail-craft, another part will be attracted back by the positively charged sail and therefore partially neutralize it, and third part will produce an electron cloud near the surface of the sail which will screen the electric field [54]. Also, electrons from solar wind can partially neutralize the positively charged sail.

During the sail mission total surface charge density can be written as:

$$\Delta Q_{\mathrm{s}} = e\left(\frac{dN_{\mathrm{i}}}{dt} - \frac{dN_{\mathrm{r}}}{dt}\right)\Delta t, \tag{3.1}$$

where dN_{i}/dt is the number of sail atoms ionized per second and square meter, dN_{r}/dt is the number of sail ions recombined per second and square meter, Δt is the operation time of the sail mission [54]. Now one can determine the rate of ionization. It is shown e.g. by Kazerashvili and Matloff [54] that only a small fraction $X\%$ of sail atoms are ionized. X has to be determined experimentally. In order to estimate the recombination rate of sail atoms per unit area, first one has to calculate the number recombined sail ions per mass. In kg this is [54]:

$$\frac{N_{\mathrm{A}}}{A10^{-3}} \cdot \frac{X}{100}, \tag{3.2}$$

where N_{A} is Avogadro's number and A is the mass number. Multiplying this number by the sail material density ρ_{Sail} and the thickness of the sail L_{s} (see Fig. 3.1 [54]) one obtains the number of recombined sail ions per unit area:

$$\frac{N_{\mathrm{A}}\rho_{\mathrm{Sail}}L_{\mathrm{s}}}{A10^{-3}} \cdot \frac{X}{100}. \tag{3.3}$$

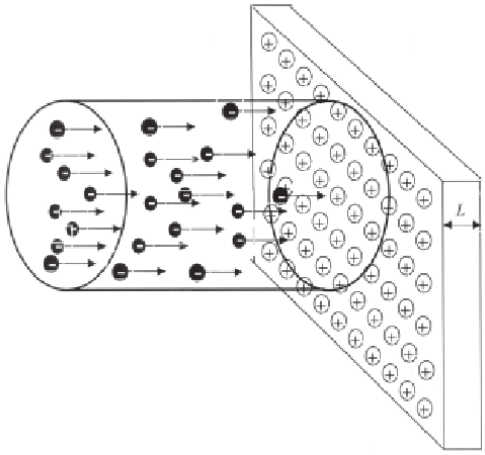

Figure 3.1: Schematic representation how solar wind electrons (black circles) bombard metal ions (white circles), of a sail of thickness L [54].

The flux of incident electrons is $n_e \times v_e$, where n_e is the number density and v_e the velocity of the incident electrons, respectively. Hence the recombination rate per unit time and area is:

$$\frac{dN_r}{dt} = n_e v_e \frac{N_A \rho_{Sail} L_s}{A \cdot 10^{-3}} \frac{X}{100} \Sigma_{RR} \tag{3.4}$$

where Σ_{RR} is the total cross section of radiative recombination processes. The cross section decreases with increasing electron energy, as the Bethe-Bloch-equation for the interaction of electrons with metal surfaces proves [66]. The recombination rate increases with:

- number density of incident electrons,
- velocity of incident electrons,
- thickness and density of the metallic foil,
- the total cross section of radiative recombination.

On the other hand it decreases with mass number of metallic foil. A charged sail can cause a failure of the electrical equipment mounted in the sail-craft. Charged foils can cause also distortions in a trajectory of the sail-craft, since solar ions are screened by the foil and an additional pushing force may act. Therefore sophisticated methods have to be developed to discharge the sail.

3.1.2 Sputtering - removal of the metallic foil ions by the incident particles

Sputtering is defined as removal of material atoms by incident particles: neutral atoms, neutrons, protons or electrons. The sputtering is a well investigated subject, there exist many reviews [11, 17, 51, 73, 74, 99]. Sputtering as a physical process has many useful applications:

- the production of atomically clean surfaces in vacuum,
- analysis of surfaces,
- the production of the thin films.

The production of atomically clean surfaces was studied by Fransworth et al. [30]. They have described, how impurities are removed from surfaces. The bombardment of surfaces of neutral or charge particles has, however, some unwanted side effects: it damages the surfaces. In this thesis it will be considered only the second point: the analysis of the surfaces and their damages.

Methods to analyze materials by sputtering was studied e.g. by Liebl and Herzog [62]. The idea is to sputter a target, and the fraction of particles that leaves the material as ions is accelerated and analyzed in a mass spectrometer. This technique is known as the secondary ion mass spectrometry, *the SIMS* [74]. The idea is to measure the charged/neutral ratio of the sputtered ions, which depends on the state of the surface and can vary from on element to another. The *SIMS* method can provide useful information about the physical properties of the metallic foil [74]. Castaing and Slodzian [19] used the secondary ion technique for spatial surface analysis. Abdullayeva el al. [2] have used secondary ions from sputtered surfaces to produce negative ions for particular applications [74].

An appropriate theory of sputtering was developed e.g. by Sigmund in 1969 [99]. Sigmund's description is based on the collision processes, Boltzmann's equations and general transport theory. Sputtering takes place when the incident atoms that sputter off surface ions have a larger kinetic energy then the surface binding energy of the metal ions. A collision cascade can be initiated when the incident particle energy E is sufficient to transfer an energy greater than the displacement energy of a lattice atom. Sigmund considered the amount of energy per unit length $F(x, E, \kappa)$ that is transferred to the lattice in a layer of a thickness dx at x close to the surface by incident particles of an energy E; κ is the direction cosine. He has shown that the number of low-energy atoms which are put in motion in an energy range from E_0 to $E_0 + dE_0$ (where E_0 is the energy of sputtered ions) in the pre-defined layer is [73, 74, 99]:

$$\frac{6}{\pi^2}\frac{F(x, E, \kappa)}{E_0^2}dE_0dx, \qquad E_0 \ll E. \tag{3.5}$$

To calculate the number of surface atoms $SY(E, \kappa)$ that acquired sufficient energy to overcome the surface binding energy one has to integrate Eq. 3.5 over the surface [73, 74, 99]. The result is:

$$SY(E, \kappa) = \frac{3}{4\pi^2}\frac{F(0, E, \kappa)}{n_0 U_0 C_0}, \tag{3.6}$$

The $SY(E, \kappa)$ is also known as a Sputtering Yield. Here n_0 is the number density of material atoms in a unit volume, U_0 is the surface binding energy, C_0 is a constant value with a dimension of an area [74, 99]. The energy loss per unit length $F(x, E, \kappa)$ is in detail derived in Winterbon et al. [110]. For the low incident particle energies up to 1 keV, Eq. 3.6 can be approximated by:

$$SY(E, \kappa) = \alpha_{\mathrm{m}}\frac{3}{4\pi^2}\frac{4mM}{(m + M)^2}\frac{E}{U_0}, \tag{3.7}$$

where m is the mass of the incident particle, M is the mass of the material ion, α_{m} is a dimensionless physical quantity which depends on the ratio M/m. For the high energy incident particle energies greater or equal than 1 keV [74]:

$$SY(E,\kappa) = 0.042\alpha_{\mathrm{m}} 4\pi Z_m Z_M \frac{ae^2}{U_0}\left(\frac{m}{m+M}\right) s_n(\epsilon_{\mathrm{m}}), \tag{3.8}$$

where $\epsilon_{\mathrm{m}} = a\frac{ME}{m+M}/(Z_m Z_M e^2)$, Z_m, and Z_M are charge numbers of the incident particle and the material ion, respectively. $s_n(\epsilon_{\mathrm{m}})$ is a universal function tabulated by Lindhard et al. [64], $a = 0.8853 r_0 (Z_m^{\frac{2}{3}} Z_M^{\frac{2}{3}})^{-\frac{1}{2}}$, and r_0 is the Bohr radius.

The sputtering yield can also be defined as a function of an angle between the normal to the irradiated surface and the path of the incident particles $SY(\theta)$:

$$SY(\theta) = \frac{SY(E,\kappa)}{SY(E,1)} = \sec^f \theta, \tag{3.9}$$

where f is a function of the ratio of the mass of a material ion and a mass of the incident particle M/m [74]. The coefficient is plotted in Fig. 3.2.

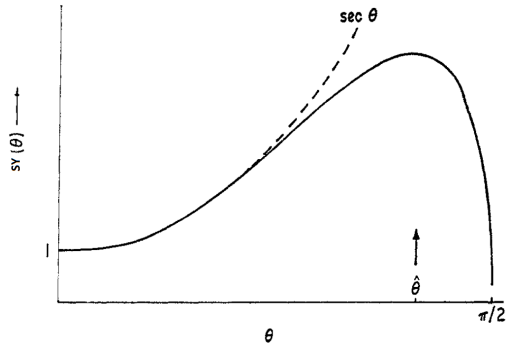

Figure 3.2: The sputtering yield as a function of angle θ [74].

The sputtering yield $SY(\theta)$ has its maximum at $70^o \sim 80^o$ and then decreases to zero at 90^o. This fact cannot be explained by use of here presented theory, because according to the Eq. 3.9, $SY(\theta)$ is proportional to the secans of the angle θ [74]. However, the theory can explain the phenomenon up to $\theta \leq 80^o$, as it is seen in Fig. 3.2. For angles larger than 80^o is not a dominating degradation effect.

There exist many sputtering experiments. Karmakar et al. [52] investigated the sputtering on to a variety of thin metallic foils: Co, Cu, Ag, Pt and Au. The thickness of films varied in the range of 30 - 200 nm. The samples were exposed to ion fluences of 1×10^{17} ions cm^{-2} for Co, Cu, Ag and Au and 5×10^{16} ions cm^{-2} for Pt of the 16.7 keV Ar^+ ion beam. The base pressure in the target chamber was less than 5×10^{-8} mbar [52]. Results are presented in Fig. 3.3.

The first column shows unbombarded surfaces, while the second, third and fourth columns shows surface bombarded under $\theta = 60^o$, 70^o and 80^o with above mention fluxes, respectively. At 60^o riples appear for Co and Cu parallel to the ion beam direction. At 70^o arrays of tiny cones appear in the ion beam direction. At 80^o characteristic ripples appear in all films [52].

By use of the SRIM software one can calculate the sputtering yield for a given angle between normal to the target and a beam line. 7.5 μm Kapton foil covered on both sides with 100 nm Al, a typical solar sail material, was examined. The sample was irradiated

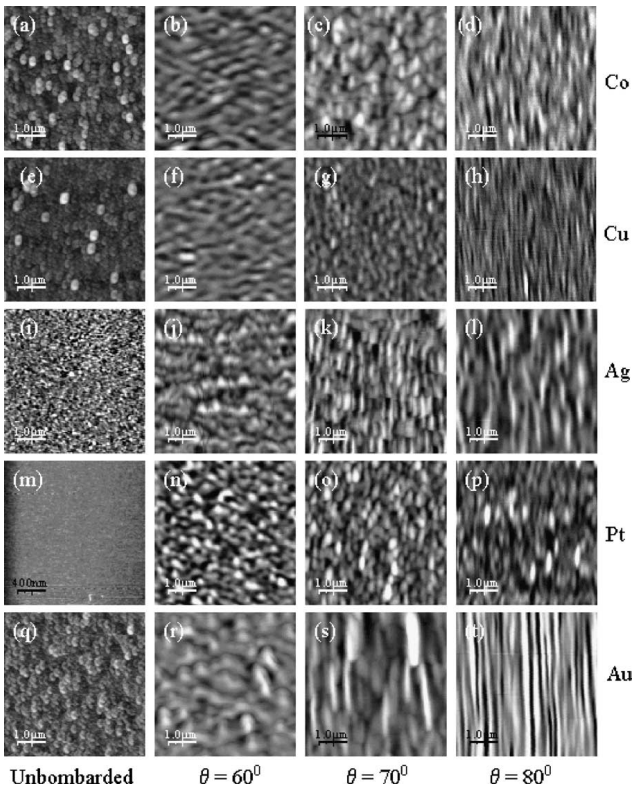

Figure 3.3: First column shows unbombarded surfaces, second, third and fourth 60^o, 70^o and 80^o of the θ angle, respectively. Rows from top to bottom for: Co, Cu, Ag, Pt and Au [52].

perpendicular by incident protons. Fig. 3.4 shows the sputtering yield as a function of energy of incident protons. Results are derived for 1000 incident particles.

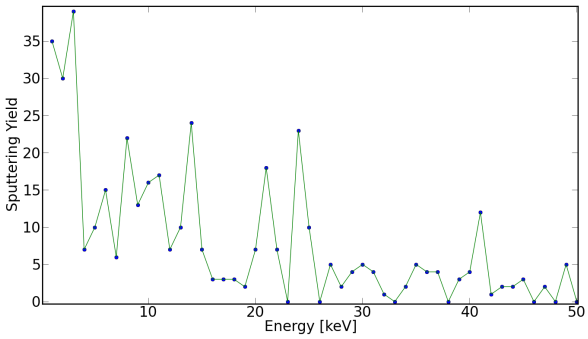

Figure 3.4: sputtering yield as a function of the energy of incident protons. The data were derived by use of the SRIM software [114].

The sputtering yield decreases with increasing energy. It is obvious because more energetic particles penetrate the foil to higher depths, while low energy incident particles degrade only the first few atomic layers of the foil. This causes the ejection of foil ions from the surface.

In the laboratory it is possible to measure the mass of a foil before and after irradiation. The mass difference is proportional to the number of sputtered ions. It is worth studying both

experimentally and theoretically the sputtering yield for a given configuration of: energy of incident particles, angle between beam line and surface normal, type of target film, pressure and temperature conditions in the vacuum chamber, where the sputtering processes are observed.

3.1.3 Atomic Oxygen - ATOX

Atomic Oxygen (AO) in the Low Earth Orbits (LEOs) is known to cause severe damage to organic-based materials as well as to polymers and metals. It is produced by the photo-dissociation of molecular oxygen in the upper atmosphere by solar radiation of wavelength of about 243 nm [8]. Fig. 3.5 shows the relation between the altitude and the concentration of the AO (lower scale) [77]. For moderate solar activity and for an altitude of 500 km the concentration of ATOX is 10^7 cm^{-3} and the flux is 10^{13} cm^{-2} s^{-1}. In this altitude the thermal energy of ATOX is about 0.1 eV [8]. At LEO space vehicles are orbiting the Earth with velocities of 7.113 to 7.726 km s^{-1} [80]. Under such conditions the impact energy of ATOX on the satellite is about 5 eV.

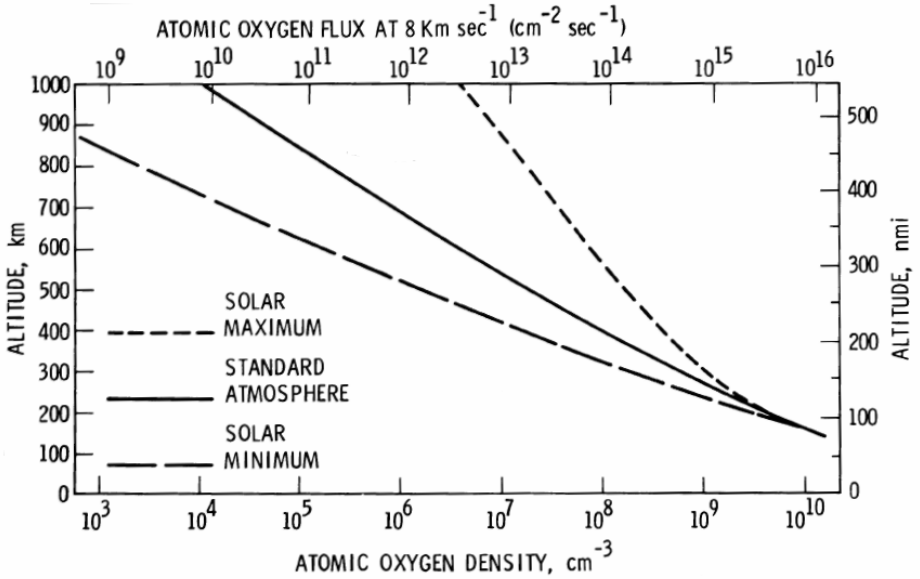

Figure 3.5: Atmospheric Atomic Oxygen density in Low Earth Orbit [90].

SASLab, the Laboratory of the Aerospace and Astronautics Engineering Department of the University of Rome performed experiments with Kapton and Kapton-ge films. Kapton-ge film is a germanium coated Kapton film [14]. The SAS (Space Environment Simulator) facility simulates space conditions of the LEO in which the impacting kinetic energy between the spacecraft moving with speed 7-8 km/h and incident particles is approximately 4.5 - 5 eV [14, 39, 112]. SAS facility used ATOX as incident particles. Degradation processes manifest themselves as material's mass loss, changes of chemical, electrical, thermo-optical and mechanical properties of the irradiated foils [14, 38, 76].

Fig. 3.6 shows results of bombardment of Kapton (first columns) and Kapton-ge (second column) films. The Kapton film looks very smooth before bombardment (upper left, magnification 20000). After 1 h bombardment by ATOX ions with a fluence of 4.3×10^{18} ions cm^{-2}

(lowe left, magnification 60000) the surface is eroded and has a cone-like morphology [14]. Kapton-ge film before experiment (upper right) looks similar to the Kapton film. After 1 h of bombardment with the same fluence of ATOX ions, it's erosion looks very different (lower right): there appears only a slightly visible roughness of the surface. Of course the differences of the bombardment results are caused by structural differences between both films [14].

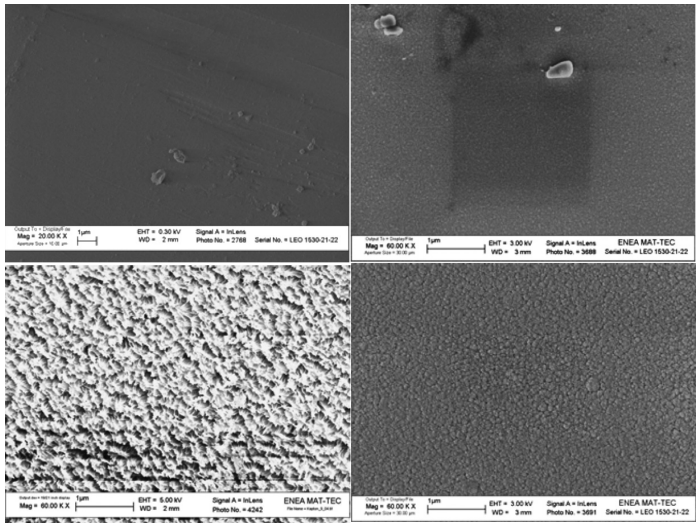

Figure 3.6: Two films, Kapton (first column) and Kapton-ge (second column) before (first row) and after (second row) bombardment of 4.3×10^{18} ATOX ions cm^{-2} in 1 hour experiment [14].

Degradation effects caused by ATOX are considered as one of the most serious hazard to spacecraft materials and are effective at altitudes between 200 and 700 km [90]. They change optical, mechanical, electrical and chemical properties of materials [40]. Fig. 3.7 shows the erosion of a Kapton foil covered with Aluminum. The picture has been taken by the electronic microscope [9]. It givens an impression how a typical ATOX flux of 10^{13} cm^{-2} s^{-1} damages surfaces exposed to it over a few mission years.

3.1.4 Electromagnetic radiation

The contribution of all degradations encountered in space can be represented by a decrease of the thermo-optical efficiency of investigated materials over the exposure time of materials [21].

The most important defects in the free space originates from the complex influence of the ultraviolet radiation at wavelength below 200 nm together and simultaneously with particle radiation by protons and electrons [65].

The role of UV radiation in degradation processes of space materials have been studied experimentally by many scientific groups. Selected results and conclusions are presented below.

Simultaneous ultraviolet and ionizing radiations can give different results then those obtained during an irradiation using only one type of irradiation, or two types of irradiations sequentially carried out [93]. That has been shown by a series of experiments made at ONERA/DESP. Various polymers and white paints have been used: Polyamide Kapton, S13G/LO, PSG120, Z93 and PSZ 184 [93].

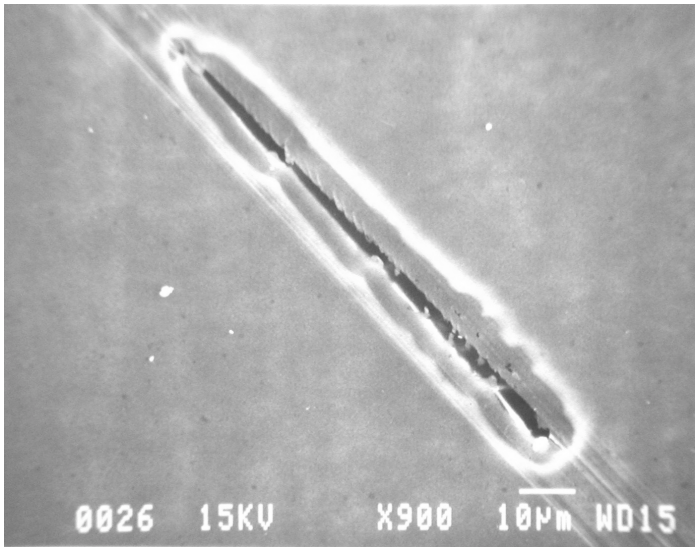

Figure 3.7: The scanning electron microscope photography. The crack is caused by ATOX bombarding an Aluminum covered with Kapton film [9].

Studies of solar absorption coefficient α_S have been made by a DLR group in collaboration with the Institute of Physics and Power Engineering, Russia. It has been shown that UV radiation together with proton/electron irradiation causes a larger increase (about 131 %) of α_S, apposed to the exposure of the sample only to protons/electrons [3, 65]. The sample was a 7.5 μm thick Kapton foil, its front side was covered with a 100 nm Al layer and its back side with 30 nm Chrome layer [65]. The black chrome back side guarantied a fast thermalization. The front side of the sample was exposed to the radiation sources.

According to the irradiation test performed in the SEMIRAMIS facility (ONERA), degradation of silicate (white ceramic) and silicone paints is higher with electrons than with UV light and proton irradiation [69]. The degradation of material was measured as a change of solar absorption coefficient and reflectance of irradiated probes. The test duration of 5 months simulated eight years of flight in a Geostationary orbit (GEO) [69].

Another set of tests was made by Sharma et al. [96]. The group used the SEMIRAMIS facility (ONERA). The goal was to simulate the radiative geostationary space environment. Different kind of materials were examined: white paints, black paints, multilayer insulation materials (MLI), varnish coated aluminized polyimide, germanium coated polyimide, polyether ether katone (PEEK) and poly tetra fluoro ethylene (PTFE). The solar absorption coefficient α_S as well as the thermal emission coefficient ϵ_t ware measured after 0.5, 1.0, 2.0 and 3.0 ESY (Equivalent Sun Years) of irradiation of the UV-light. Note that Equivalent Sun Hour (ESH) is defined as a number of laboratory irradiation hours multiplied by the number of used solar constants in a given spectral range. For instance for MLI after 3 ESY of irradiation the α_S increased by a factor of 32.5% after UV exposure. The α_S increased by a factor of 47.9% when MLI was exposed to UV radiation together with irradiation of electrons and protons. For aluminized Polymide foil and 3 ESY the α_S increased 46% after the exposure only to UV light. It increased 58.73% after irradiation of the sample with UV-light together with electrons and protons. On the other hand the emissivity ϵ_t increased by a factor of: 1.95% and 2.78% for MLI and aluminized Polyimide, respectively. This is a significantly increase then observed for α_s. Note that ϵ_t was measured after the samples were

exposed to UV-light and irradiated by electrons and protons together.

Unfortunately, the group used the sequential irradiation of the samples, which means that the probe was first exposed to UV-light then α_S was measured and after that the same sample was irradiated by electrons and protons and again α_S was measured. This method does not allow to examine the true role of degradation of the probe due to electrons/protons irradiation alone, because the optical properties of the sample were already changed by the preceding UV irradiation.

The space mission BepiColombo to planet Mercury planned and prepared by ESA together with JAXA, provides a great opportunity to check the role of UV radiation in the degradation process of the protection shield of the spacecraft. Tests have been made in the ESA/ESTEC laboratories [45]. The shield has been produced with various silicate paints (white ceramic). Probes were irradiated by two types of UV radiation sources: a deuterium lamp (UV) and a VUV source. The UV wavelength bandwidth is 200 to 400 nm, while the VUV bandwidth is 115 to 200 nm. Probes were exposed at elevated (450^oC) temperature to UV and VUV radiation of approximately 17 Solar Constants (SC), accumulating a total UV dose of 52000 ESH [45]. Many types of white ceramic have been used (Astroquartz 2, Astroquartz 3 and Nexel Refrex 1210), the increase of the solar absorptance α_S varied from 353 % to 410% [45].

In summary, the optical properties (α_S, ϵ_t) of different kinds of surfaces are damaged more by exposure to UV-light then by electron/proton irradiation at least relatively short distances to the Sun [3, 65]. However, according to the studies accomplished by Marco et al. [69] in a GEO orbit, electrons cause larger changes of optical properties of white ceramic and silicone paints then UV-light together with proton irradiation. However in case of aluminized Kapton and MLI blankets sequential irradiation with UV-light and charge particles has shown then the UV-light causes the main contribution to changes of the solar absorption and the thermal emission coefficient [96]. Extreme environmental conditions like those which are present at Mercury distance to the Sun were carefully studied at ESA/ESTEC [45]. The growth of the solar absorption coefficient of white ceramic due to UV radiation was enormous. Unfortunately degradation effects due to particle irradiation were not taken into account.

3.2 Blistering

H_2 blisters are metal bubbles filled with hydrogen molecular gas resulting from recombination processes in the metal lattice. Blistering occurs as an effect of irradiation damages. It changes the physical properties of the irradiated surface and increases the erosion rate [7]. As it is known from experiments, caps of blisters lose thermal contact with the target body and, therefore, become overheated under intensive beams [7]. Growth of blisters on a flat surface can be considered as the increase of surface roughness that causes the decrease of mirror reflectivity [7].

Degradation of structural properties of solids, referred to as embrittlement caused by Hydrogen, plays an important role in material physics [67]. Four general processes of the embrittlement have been proposed: formation of a hydride phase, enhanced local plasticity, grain boundary weakening, and blister/bubble formation [67, 81].

Blistering is caused by formation of pockets of hydrogen gas just below the metal surface. The tendency to form bubbles depends on: proton energy, time - integrated proton flux, temperature of the target, crystallographic orientation of the irradiated surface and on impurities and defects in the sample [22]. The amount of Hydrogen retained in the sample

is sensitive to the crystallographic orientation as well as to the diffusion rate [22].

Hydrogen atoms are much smaller then metal atoms, but they can introduce strain into the metal lattice when absorbed as interstitial atoms [75, 89, 105]. They can also change the electronic structure of near neighbor metal atoms [89]. That causes an increase of the energy of the sample. The energy may be decreased by the aggregation of the interstitial hydrogen atoms into hydrogen atom clusters, which then form molecular hydrogen bubbles [89]. Hydrogen could not agglomerate into H_2-clusters without the presence of vacancies in the metal lattice. The final number of bubbles depends on the number of vacancies initially placed in the metal lattice [77], i.e. it depends crucially on the production process of the metallic surfaces. A single vacancy in Aluminum can trap up to twelve H atoms. For comparison, a vacancy in Iron can trap only up to six H atoms [67].

Blistering takes place together with the so-called pitting formation. The pits are surface micropores that occur during proton irradiation of materials. The distribution of pits was found to be affected by particle energy, total flux, crystal orientation, and crystal substructure [77]. The density of pits increase with decreasing energy of incident particles. Thus, even a perfectly produced metallic surface that contains no vacancies will acquire a certain surface roughness as soon as it is exposed to solar proton irradiation.

3.2.1 Time evolution of bubble formation

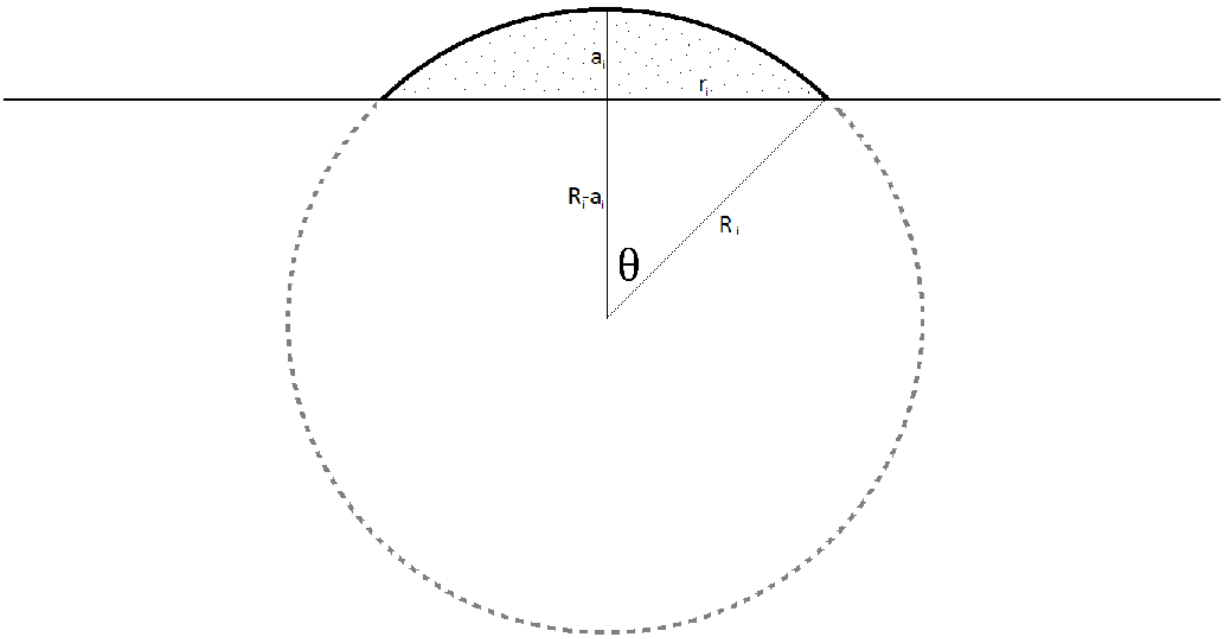

Figure 3.8: Schematic representation of a bubble. The dotted area is filled with hydrogen molecular gas. The bubble has a radius of r_i and the height of a_i.

Fig. 3.8 shows the scheme of a cap of a sphere with a radius R_i. Here a_i is the height

of the cap, while r_i is it's radius. Hereafter the cap is named as the bubble. By use of the spherical coordinates, the volume of the i$^{\mathrm{th}}$ bubble is:

$$V_\mathrm{i} = \frac{2}{3}\pi r_\mathrm{i}^3, \tag{3.10}$$

For simplicity in this thesis a half sphere is considered, i.e. $a_\mathrm{i} = R_\mathrm{i} = r_\mathrm{i}$. The general equation as well as the relation between the height and the radius of a cap of a sphere is presented in Appendix B.1.

The differential growth of the radius of the i$^{\mathrm{th}}$ bubble dr_i is caused by a small portion of H_2 molecules merged to the bubble in a period of time dt.

It is assumed that the gas inside the i$^{\mathrm{th}}$ bubble behaves like an ideal gas:

$$p_\mathrm{i} V_\mathrm{i} = \sum_\mathrm{j}^\mathrm{N} N_{\mathrm{H_2,i,j}} k_\mathrm{B} T, \tag{3.11}$$

where p_i is the pressure of the gas, k_B is the Boltzmann constant, T denotes the temperature of the sample, $N_{\mathrm{H_2,i,j}}$ is the number of H_2 molecules merged to the i$^{\mathrm{th}}$ bubble in the j$^{\mathrm{th}}$ period of time step Δt_j, N is the number of tiny time steps, hence $N \times \Delta t_\mathrm{j}$ is the total irradiation time of the sample. The number $N_{\mathrm{H_2,i,j}}$ is then given by:

$$N_{\mathrm{H_2,i,j}} = 0.5 \left(N_\mathrm{B}^\mathrm{T}\right)^{-1} N_{\mathrm{p^+,j}}\ \eta\ \xi_{\mathrm{H_2}}\ (1 - BS), \qquad N_\mathrm{B}^\mathrm{T} = N_\mathrm{B} A_\mathrm{s}, \qquad N_{\mathrm{p^+,j}} = I \Delta t_\mathrm{j} A_\mathrm{s}. \tag{3.12}$$

The factor 0.5 reflects that a single H_2 molecule consists of two H atoms, N_B^T is the total number of bubbles on the irradiated sample, N_B is the number of bubbles per unit area, I is the proton flux, A_s is the area of the sample, $N_{\mathrm{p^+,j}}$ is the number of protons sent to the sample in the j$^{\mathrm{th}}$ period of time step Δt_j. While 100% of protons recombine into H atoms in the metal lattice, only a few percent of them recombine to H_2 molecules [18]. Hence the η factor is the relation between the number of H_2 molecules and the H atoms in the lattice. Not all of the H_2 molecules will merge into a H_2-clusters and finally to H_2-bubbles, hence the $\xi_{\mathrm{H_2}}$ factor is the relation between the number of H_2 molecules inside and outside the bubbles. BS is the factor of backscattered ions. If BS is 1 then all of the incident ions are backscattered. If BS is 0 then all of the incident ions penetrate into the target. BS depends on the proton energy and on metal properties and can be estimated by use of the SRIM software [114].

The first step to estimate the radius of the i$^{\mathrm{th}}$ bubble is to calculate the Helmholtz free energy of the whole configuration F_config. Since the free energy is an additive quantity, the total free energy of bubble formation is a sum of following constituents: free energy of H_2 gas inside the i$^{\mathrm{th}}$ bubble ($F_\mathrm{gas,i}$), the metal deformation ($F_\mathrm{md,i}$) of the surface caused by the bubble itself, the surface free energy ($F_\mathrm{surf,i}$) of the cap of the bubble, free energy of H_2 molecules ($F_{\mathrm{H_2}}$), and that of the H atoms (F_H) placed outside the bubbles within the metal lattice.

The Helmholtz free energy of the whole configuration described above is:

$$F_\mathrm{config} = F_\mathrm{gas,i} + F_\mathrm{md,i} + F_\mathrm{surf,i} + F_{\mathrm{H_2}} + F_\mathrm{H}. \tag{3.13}$$

The next step is to estimate the free energy of the increase of the i$^{\mathrm{th}}$ bubble. It consists of the free energy of a gas filled in the bubble, the free energy of a metal deformation, and of the surface free energy of the bubble cap.

Using the well known thermodynamical relation between the pressure of the gas and the Helmholtz free energy, $p = \left(\frac{\partial F}{\partial V}\right)_T$, together with Eq. 3.11, the free energy of a gas contained in the i$^{\text{th}}$ bubble is:

$$F_{\text{gas,i}} = -\sum_{\text{j}}^{\text{N}} N_{\text{H}_2,\text{i,j}} k_{\text{B}} T \ln\left(\frac{V_{\text{max,i}}}{V_{\text{min}}}\right), \tag{3.14}$$

where $V_{\text{max,i}}$ is the maximum volume a bubble can reach before it breaks, while V_{min} is its minimum volume.

It is assumed that two H_2 molecules form the smallest possible bubble. The radius of such bubble is approximately 3.2 Bohr radius [88].

The bubble will crack if the pressure of the gas inside is higher then the pressure exerted by the metal deformation of the cap. The relation between the pressure of the gas, the strain σ_{s} of the metal, and the bubble radius corresponding to $V_{\text{max,i}}$ is [61]:

$$p_{\text{gas, insite bubble}} - p_{\text{outside bubble}} = \frac{2\sigma_{\text{s}}}{r_{\text{max,i}}}. \tag{3.15}$$

Since it is assumed that the sample is placed in the space vacuum, the pressure outside the bubble is set to zero. The strain is a function of the temperature and it is unique for a given material. The maximum volume of the bubble is:

$$V_{\text{max,i}} = \frac{2}{3}\pi \left[\frac{3\sum_{\text{j}}^{\text{N}} N_{\text{H}_2,\text{i,j}} k_{\text{B}} T}{4\pi\sigma_{\text{s}}(T)}\right]^{\frac{3}{2}}. \tag{3.16}$$

The free energy of a metal deformation $F_{\text{md,i}}$ caused by the bubble with radius r_{i} can be found in [58]. It is given by the following relation:

$$F_{\text{md,i}} = \frac{4\pi}{3}\frac{r_{\text{i}}^3(1+\gamma_{\text{p}})}{E_{\text{Y}}} p_{\text{i}}^2. \tag{3.17}$$

Here γ_{p} is the Poisson coefficient, i.e. the ratio of transverse to axial strain of the sample material, E_{Y} is the Young module. In Appendix B.4 in Table B.2 some Poisson coefficients and Young modules for common materials are listed.

The free energy of a surface of a cap of the i$^{\text{th}}$ bubble can be found in [70]. It is given by:

$$F_{\text{surf,i}} = 4\pi r_{\text{i}}^2 \sigma_{\text{s}}(T). \tag{3.18}$$

The Helmholtz free energy of H_2 molecules located outside the bubbles at certain positions within the metal lattice is expressed by the following relation:

$$F_{\text{H}_2} = \left(N_{\text{H}_2}^{\text{T}} - \sum_{\text{i}}^{N_{\text{B}}^{\text{T}}}\sum_{\text{j}}^{\text{N}} N_{\text{H}_2,\text{i,j}}\right)\left[\epsilon_{\text{H}_2} + k_{\text{B}} T \ln\left(\frac{N_{\text{H}_2}^{\text{T}} - \sum_{\text{i}}^{N_{\text{B}}^{\text{T}}}\sum_{\text{j}}^{\text{N}} N_{\text{H}_2,\text{i,j}}}{N_0}\right)\right], \tag{3.19}$$

where $N_{\text{H}_2}^T$ is the total number of H_2 molecules inside the sample, N_{B}^{T} is the total number of bubbles on the sample, ϵ_{H_2} is the binding energy of the H_2 molecule with a vacancy, and N_0 is the number of the lattice sites. The detailed derivation of the Eq. 3.19 is presented in Appendix B.2.

Similarly, the Helmholtz free energy of H atoms located outside bubbles at certain positions within the metal lattice is described by:

$$F_{\mathrm{H}} = \left(N_{\mathrm{H}}^{\mathrm{T}} - 2N_{\mathrm{H_2}}^{\mathrm{T}}\right)\left[\epsilon_{\mathrm{H}} + k_{\mathrm{B}}T\ln\left(\frac{N_{\mathrm{H}}^{\mathrm{T}} - 2N_{\mathrm{H_2}}^{\mathrm{T}}}{N_0}\right)\right], \tag{3.20}$$

where ϵ_{H} is the migration energy of the H atom in the metal lattice, and $N_{\mathrm{H}}^{\mathrm{T}}$ is the total number of H atoms in the sample. The detailed derivation of the Eq. 3.20 can be found in Appendix B.3.

Since now each term of the Eq. 3.13 is determined, the next step is to estimate the radius r_{i} of the i^{th} bubble at a given time t. This will be performed by assuming that the process of bubble growth is a quasistatic one, i.e. during each j^{th} time step Δt_{j} a small portion of H_2 molecules is merged to the i^{th} bubble and the thermodynamic equilibrium is rapidly established:

$$\frac{\partial F_{\mathrm{config}}}{\partial N_{\mathrm{H_2,i,j}}} = 0. \tag{3.21}$$

The condition leads to the following relation:

$$8\pi\Xi_{\mathrm{i,j}}\sigma_{\mathrm{s}}(T)r_{\mathrm{i}}^5 - H_{\mathrm{i}}r_{\mathrm{i}}^4 + \frac{3}{\pi}\frac{1+\gamma}{E}\left(\sum_{\mathrm{j}}^{\mathrm{N}} N_{\mathrm{H_2,i,j}}\right)k_{\mathrm{B}}^2T^2\left[2Nr_{\mathrm{i}} - 3\Xi_{\mathrm{i,j}}\sum_{\mathrm{j}}^{\mathrm{N}} N_{\mathrm{H_2,i,j}}\right] = 0, \tag{3.22}$$

$\Xi_{\mathrm{i,j}}$ is defined below in Eq. 3.25. H_{i} is an abbreviation of:

$$H_{\mathrm{i}} = -\frac{\partial F_{\mathrm{gas,i}}}{\partial N_{\mathrm{H_2,i,j}}} - \frac{\partial F_{\mathrm{H}}}{\partial N_{\mathrm{H_2,i,j}}} - \frac{\partial F_{\mathrm{H_2}}}{\partial N_{\mathrm{H_2,i,j}}}. \tag{3.23}$$

The derivatives of the Helmholtz free energy of the gas inside the i^{th} bubble, of metal deformation caused by the bubble, of H_2 molecules and of H atoms with respect to the number of H_2 molecules added at the j^{th} time step to the i^{th} bubble are shown in the Appendix B.4.

Experimental facts, the possibility of formation of hydrogen molecular bubbles under space conditions as well as the numerical solutions of Eq. 3.22 will be considered in Section 3.2.2. Finally in Section 3.2.3 the reflectivity of a foil coved with a certain hydrogen molecular bubbles having different sizes will be presented.

3.2.2 Experimental facts, space environment, and numerical analysis of bubble formation

The plan of the Section is as follows: first the physical conditions under which bubble formation is possible at all are explored and some numerical simulations that use proton fluxes at Earth orbit will be shown. Then the possibility of growth of hydrogen molecular bubbles on metallic surfaces under space conditions will be considered.

Experimental facts

According to experiments performed by many scientific groups, e.g. [22, 77, 78], there exist two critical parameters for the bubble formation: the total dose of protons and the temperature of a sample. The temperature range in which bubbles were observed on the foils is 288-573 K [22, 77]. Above 630 K, the diffusivity of H in Aluminum is so large that Hydrogen atoms escape from the metal lattice before they can form bubbles [78]. Depending on the experimental setup, the critical dose of protons above which the process occurs is $10^{16}...10^{17}$

H^+cm^{-2}. The blistering phenomenon was observed also after sample irradiation by H_2^+ ions. In that case the critical dose of ions above which the process took place is $\sim 10^{18}$ H_2^+ cm^{-2}.

A large set of proton irradiation tests has been made by Milacek et al. [77]. Rolled 99.999% Aluminum was used as target material. The energy range of incident protons varied from 10 to 200 keV. Aluminum samples were exposed to a flux of 1.5×10^{12} and 11.8×10^{12} H^+ cm^{-2} s^{-1} at room temperature. Some of the samples were annealed above 470 K. Depending on the experimental setup, the total dose of protons varied from 1.0×10^{16} H^+ cm^{-2} to 3.5×10^{17} H^+ cm^{-2}. Hydrogen molecular bubbles were observed at room temperature after proton irradiation with energies lower then 70 keV. For higher proton energies bubbles appeared after annealing of the samples to approximately 470 K.

The bubbles once formed, were elongated along the rolling of the samples. Typical lengths of bubbles were 1.2 μm for samples irradiated at room temperature by 50 keV protons, and 117 μm for samples irradiated by 200 keV protons at 470 K. The higher the temperature of the sample, the larger the observable size of the bubbles.

An energetic and temperature threshold of formation of molecular hydrogen bubbles was measured by Daniels [22]. The Aluminum sample was irradiated by a flux of 100 keV protons. The total dose of protons was 10^{17} H^+ cm^{-2}. The sample was irradiated at a temperature of 300 K. Under these conditions no bubbles were observed. Afterwards, the sample was heated up to 570 K and a dense concentration of bubbles was observed.

It is worth mentioning that molecular hydrogen bubbles ware also observed on: Cooper, Tungsten, Palladium, and Iron [7]. The samples were irradiated by protons, with energies from 100 to 200 keV. The maximum dose sent to the samples was 7×10^{20} H^+ cm^{-2}. Two temperatures of the samples were investigated: 297 and 370 K, respectively. The higher the temperature, the larger diameters of bubbles were observed. Materials that do not exhibit blistering are e.g. Tantalum and Vanadium. Proton doses up to 2.3×10^{20} H^+ cm^{-2} did not cause and blistering on these materials [7]. Perhaps these metals are well suited for application in space technology.

The size distribution of molecular hydrogen bubbles was studied by Kamada et al. [50]. They irradiated Aluminum foils by a flux of 25 keV H_2^+ ions. The result is shown in Fig. 3.9, for a total fluence of 4×10^{17} H_2^+ cm^{-2} (squares) and 1.6×10^{18} H_2^+ cm^{-2} (cycles). The temperature of the specimen hold at 300 K. Two samples have been irradiated. The first sample had a dimension of $20\times20\times0.1$ mm while the second one had a thickness of 5 μm. The majority of bubbles have diameters below 400 Å. The maximum number of bubbles, about 30% of the population, have a diameter of 180 Å.

Different results have been shown by Milcius et al. [78] they used as well H_{2+} ions as incident particles. The Aluminum foil of thickness of $2-5$ μm has been irradiated by a flux of 1 keV H_2^+ ions, when total fluence of incident ions was 10^{18} H_2^+ cm^{-2}. As is seen in the Fig. 3.10, the diameter of bubbles at room temperatures (left picture) is in μm range. The largest bubble diameter is smaller then 10 μm. On the other hand, at 450 K it is seen that the diameter of some bubbles is even larger then 100 μm.

Hemispherical bubbles have been observed by Rozenek [91]. Hydrogen was filled into the samples by electrochemical charging. Current densities of 50 mA cm^{-2} were applied. The method is based on the principle that the sample is negatively and the gas is positively charged. Then a flux of ions is generated. Bubbles were observed on a surface of 99.999% Aluminum samples with thickness of 2 mm. A wide variation in the size from large (tens of micrometers in diameter) to very small sizes (nanometers in diameter), in the distribution, in the density, and in the geometrical shapes of the surface bubbles were observed [91]. A single bubble of Rozenek's experiments is presented in Fig. 3.11. The picture is taken by use of the

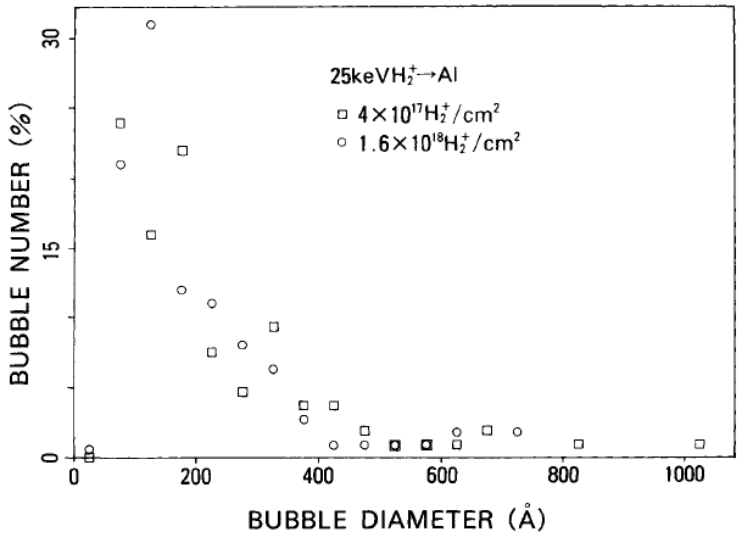

Figure 3.9: Diameter distribution of hydrogen molecular bubbles on a surface of Aluminum. The target was irradiated by 25 keV H_2^+ ions with a fluence of 4×10^{17} H^+ cm^{-2} (squares) and 1.6×10^{18} H^+ cm^{-2} (cycles) [50].

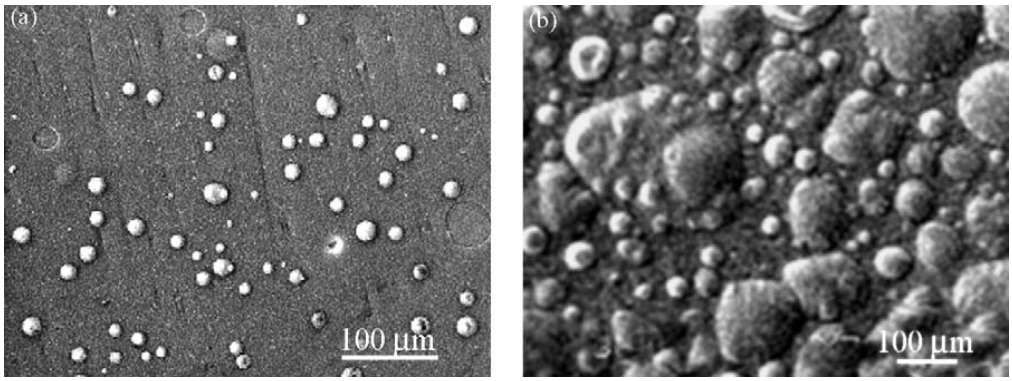

Figure 3.10: An Aluminum sample at two different stages is considered. It was irradiated with 1 keV H_2^+ ions. The left picture shows the sample at the temperature of 300 K, while the right picture at 450 K [78].

SEM (Scanning Electron Microscope) method. The Aluminum sample was electrochemically charged for 24h at room temperature. The method of electrochemical charging, however, can serve as a model of bubble creation under space conditions.

Blistering under space conditions

To check rather the growth of molecular hydrogen bubbles is possible under space conditions a simple model is considered. A cube of 1m satellite size located at 1 AU distance orbit from the Sun. The idea is to estimate the temperature of the satellite when the rotation axis is perpendicular to the orbit's plane. It is assumed that the cube is made of 10 μm polished Aluminum plates. The temperatures of the walls as a function of the rotation speed of the cube are presented in the Table 3.1. The maximum temperature denotes the temperature

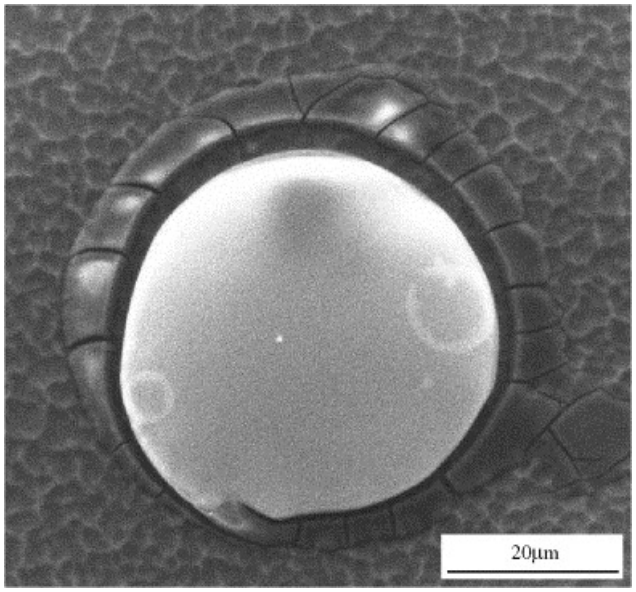

Figure 3.11: A bubble of a diameter of 50 μm is presented. The temperature of a sample was 300 K [91].

Table 3.1: The temperature of a cold wall and hot wall of a rotating cubic satellite with a given RPM is presented. Three distances from the Sun are considered: 0.5, 1.0, and 1.5 AU, respectively. The blue and red cases are not suited for bubble formation.

	1.5 AU		1.0 AU		0.5 AU	
RPM	Temp. min [K]	Temp. max [K]	Temp. min [K]	Temp. max [K]	Temp. min [K]	Temp. max [K]
0.0	3	423	3	518	3	733
0.01	100	423	101	518	101	733
0.05	165	421	168	517	170	732
0.10	202	415	207	515	213	732
0.50	278	358	316	476	346	703
1.00	300	335	350	443	418	673
5.00	314	321	382	397	524	593
10.0	320	319	385	393	535	567
50.0	317	318	388	390	547	553
100.0	318	318	389	389	549	552

of walls exposed to the Sun, while the minimum temperature is the temperature of the walls in the shady side to the Sun. Additionally two distances of the satellite to the Sun are considered: 0.5 and 1.5 AU, respectively. According to the experimentally found limits [22, 77], below a sample temperature of 288 K and above 630 K no formation of bubbles is possible. Hence values marked by blue color indicate that for the given rotational speed of the satellite and the given distance to the Sun formation of bubbles is stopped. The red color indicates that the temperature is to high to form bubbles. Therefore the temperature criterion of bubble formation is fulfilled for those satellites which are located at distances of 1.0 and 1.5 AU to the Sun, and whose rotational speed is higher then 5 RPMs if they are located at 0.5 AU distance orbits to the Sun.

The second criterion of bubble formation is to receive a minimum dose of incident protons ($\sim 10^{16}$ p^+cm^{-2}). Fig. 3.12 presents the solar proton flux at 1 AU distance. Assuming that the Sun generates only monoenergetic 5 keV protons, then the sample will collect the critical number of protons after 10^7 seconds, i.e. after 116 days. To estimate the flux of protons at

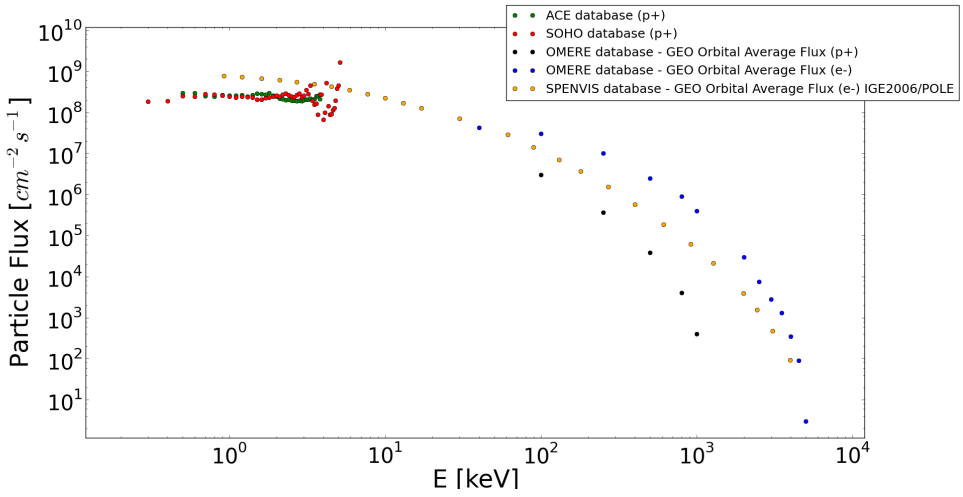

Figure 3.12: The flux of solar protons as a function of energy is presented. The four on-line databases were used: the SOHO, ACE, ONERE, and SPENVIS.

0.5 or 1.5 AU one can use the relation:

$$4\pi(1\mathrm{AU})^2 \times \mathrm{I}_{1\mathrm{AU}} = 4\pi \mathrm{r}^2 \times \mathrm{I}_{\mathrm{r}}, \tag{3.24}$$

where I_{r} is the flux at distance r. Therefore, for 0.5 AU distance orbits the bubble formation will be possible after only 29 days, while at 1.5 AU it takes 260 days to collect the minimum dose.

The presented requirements for total dose of protons as well as for temperatures clearly show that the occurrence of blistering in space, at least in the vicinity of the Earth is highly probable. Here it was assumed for simplicity that the Sun generates only monoenergetic protons. Under real space conditions with a wide spectral distribution of the proton flux, the bubble formation will proceed somewhat faster.

Numerical model of bubble formation

We consider the growth of the i^{th} bubble located on the metal surface. It is assumed that the Aluminum sample has an area of 1 cm^2. At time $t = 0$, a "seed" bubble is present that contains only two H_2 molecules in accordance with a assumption about V_{min}. At each time step Δt_{j} a number of H_2 molecules $N_{\mathrm{H_2,i,j}}$ is merged to the bubble. Hence, Eq. 3.22 has to be solved at each time step. At the beginning of the bubble growth process, the differential increase of the bubble radius $dr_{\mathrm{i,j}}$ is higher then at its end. To realize that fact lets consider a simple example. At time $t = 0$ the bubble consists of two H_2 molecules. For simplicity it is assumed that during each time step only two H_2 molecules are merged to the bubble. After Δt the bubble consists of $4H_2$ molecules, hence the number of molecules increases by 50%. At the time $2\Delta t$ the bubble consists of $6H_2$ molecules, hence the number increase is now 33.3%, and so on. A realistic description of the H_2 molecule number increase in a bubble with time is:

$$\Xi_{i,j} = \frac{\Delta r_{\mathrm{i}}}{\Delta N_{\mathrm{H_2,i,j}}} = j^{\frac{1}{3}} r_{\mathrm{i,0}}. \tag{3.25}$$

The exponent $\frac{1}{3}$ is a model parameter of a bubble growth. Increasing that exponent leads to a reduction of the pressure in the bubble. However, $\frac{1}{3}$ is a good guess accordance with experimental data.

Six models are considered. In each model it is assumed that the sample has been irradiated by a flux of protons of 6.24×10^{12} $H^+cm^{-2}s^{-1}$ during more than 10^4 seconds. Hence the criterion of the proton critical dose above which the bubble formation is observed is fulfilled. Two different temperatures of the sample are realized: 300, and 550 K, respectively. The BS coefficient is set to 10^{-2}, which means that 1% of the incident protons are back scattered. The value is taken from a set of experiments made by SRIM software [114]. The number density of bubbles per cm^2 is set to 100. The η parameter is set to 10^{-2}. This value is taken from the work of Canham et al. [18]. The free parameter ξ_{H_2}, which is the relation of H_2 molecules inside and outside the bubbles, is set to 10^{-6}, 10^{-4}, and 10^{-2}, respectively.

Results are presented in Fig. 3.13. The left plot shows time evolution of bubble growth at 300 K while the right one at 550 K. Blue-, green- and red- line denotes models with ξ_{H_2} factor of: 10^{-6}, 10^{-4}, and 10^{-2}, respectively. One can clearly see that the size of bubble is higher at 550 K than at 300 K. There is a significant difference between the size of bubble at three different ξ_{H_2} values. At time $t = 10^4$ s and temperature of 300 K the radius of the bubble is 4.3-, 7.4-, and 11.7 -times smaller than its maximum radius (defined by Eq. 3.16) for $\xi_{H_2} = 10^{-6}$, 10^{-4}, and 10^{-2}, respectively. For the temperature of 550 K the radius is 3.3-, 6.7-, and 10.8 -times smaller than its maximum one for $\xi_{H_2} = 10^{-6}$, 10^{-4}, and 10^{-2}, respectively.

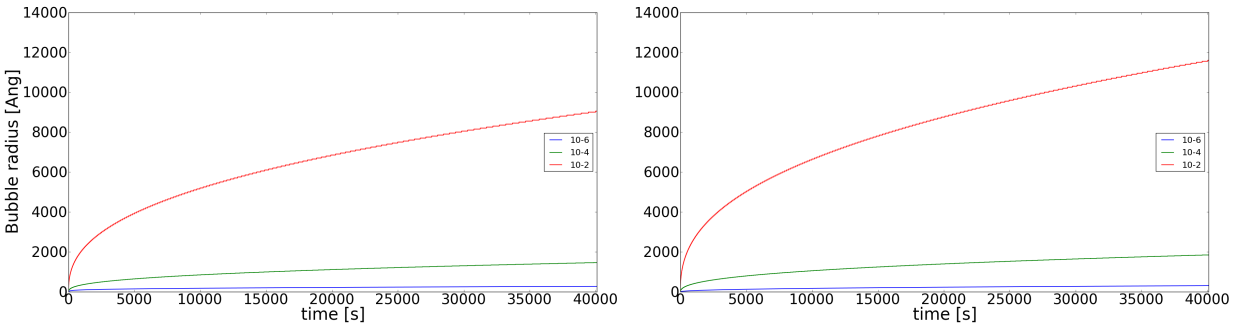

Figure 3.13: Two temperatures of the sample are considered: 300 K (left plot) and 550 K (right plot), respectively. Three different ξ_{H_2} values have been used: 10^{-6}, 10^{-4}, and 10^{-2}, respectively.

With here presented theory of bubble formation allows to predict of growth process of small bubbles (tens of Å in a diameter), as well as of those whose radius is larger than 10 μm. The presented experimental results can be reproduced. Also it has been proven that molecular hydrogen bubbles can be formed in the interplanetary medium, since both flux of solar protons and temperatures are well suited for bubble formation.

3.2.3 Reflectivity of a metallic foil covered with bubbles

The momentum transfer of a photon to an ideal reflecting surface is given by the well known relation $\Delta q = 2q\cos\theta$, where θ is the angle between the surface normal and the path of a light ray. A foil at two different surface qualities is considered. At time $t = 0$ the foil has not

been exposed to the electromagnetic radiation and/or charged particles, and is considered to be a perfect mirror with reflectivity factor $R = 1$. It means that all of the incident light rays are reflected ideally, no light ray is absorbed by the target. The other state of the foil is when it has been irradiated by a flux of protons and hydrogen molecular bubbles have been formed on its surface. The reflectivity of the degraded foil is calculated in the following way. It is assumed that the foil is covered by a grid with fixed size of a single cell. The cell has a size of $\epsilon_{\text{cell}} \times \epsilon_{\text{cell}}$, see Fig. 3.14.

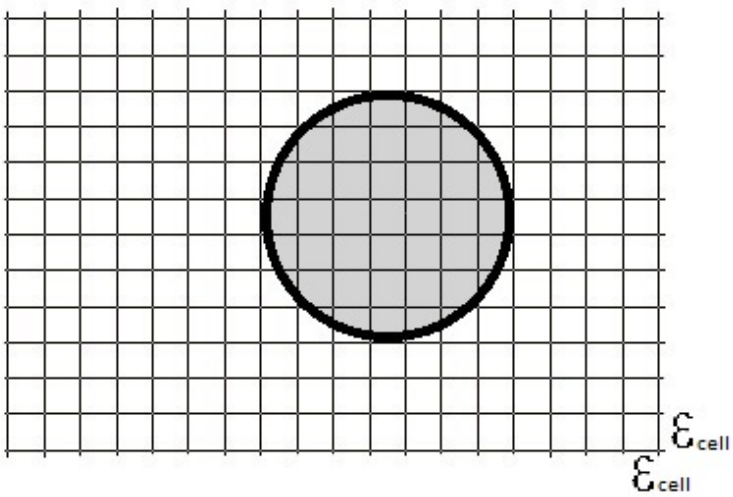

Figure 3.14: A fraction of the foil with one spherical bubble is shown. The size of a single cell of the grid is $\epsilon_{\text{cell}} \times \epsilon_{\text{cell}}$.

The reflectivity of a single cell is:

$$R_{\text{cell}} = \frac{\Delta q}{\Delta q_{\text{max}}}, \tag{3.26}$$

where Δq is the momentum transfer of a photon to the degraded foil. Δq_{max} is the momentum transfer of a photon to a cell at $t = 0$. Taking in to account all cells, one has:

$$R_{\text{foil}} = \frac{\sum_{\text{i}}^{\text{N}_{\text{cell}}} \Delta q_{\text{i}}}{\sum_{\text{i}}^{\text{N}} \Delta q_{\text{max,i}}}. \tag{3.27}$$

Here N_{cell} is the number of cells. Assuming that the flux of photons irradiates parallel to the foil surface normal, and that at time $t = 0$ the foil was a perfect mirror without surface imperfections, Eq. 3.27 reduces to:

$$R_{\text{foil}} = \frac{\sum_{\text{i}}^{\text{N}_{\text{cell}}} 2q \cos\theta_{\text{i}}}{N_{\text{cell}} \times 2q} = \frac{\sum_{\text{i}}^{\text{N}_{\text{cell}}} \cos\theta_{\text{i}}}{N_{\text{cell}}}. \tag{3.28}$$

Where θ_{i} is the angle of deflection of a photon from a single i^{th} cell. Table 3.2 shows the relation between the average radius of a bubble $\bar{r}$ and the reflectivity of a foil. Note that the size distribution of bubbles is considered to be as in Kamada et al.([50], see Fig. 3.9). Three different bubble number densities N_{B} are considered: 500, 1000 and 1500, respectively. The ratio of the average radius of the bubbles $\bar{r}$ to the size of the cell ϵ is fixed, and is set to 100. Data from the table are plotted in Fig. 3.15. It turns out that the reflectivity is very sensitive to the average radius and surface density N_{B} of bubbles that cover the irradiated

foil. For a small average radius of bubbles the change of reflectivity factor is negligibly small. For bubbles with an average radius of 100 μm the change in the reflectivity with respect to the initial state of the foil is: 7.3, 17.4, and 26.5% for 500, 1000 and 1500 N_{B}, respectively.

Table 3.2: Relation between average radius of a bubble, and the reflectivity of a foil. Three different number of bubbles per one cm^2 N_{B} are considered: 500, 1000, and 1500, respectively.

$\bar{r}$ [μm]	R: $N_{\mathrm{B}} = 500$	R: $N_{\mathrm{B}} = 1000$	R: $N_{\mathrm{B}} = 1500$
10.0	0.999	0.998	0.997
20.0	0.997	0.993	0.989
30.0	0.994	0.985	0.970
40.0	0.989	0.973	0.950
50.0	0.983	0.959	0.927
60.0	0.978	0.942	0.898
70.0	0.969	0.918	0.855
80.0	0.959	0.895	0.789
90.0	0.944	0.857	0.752
100.0	0.927	0.826	0.735

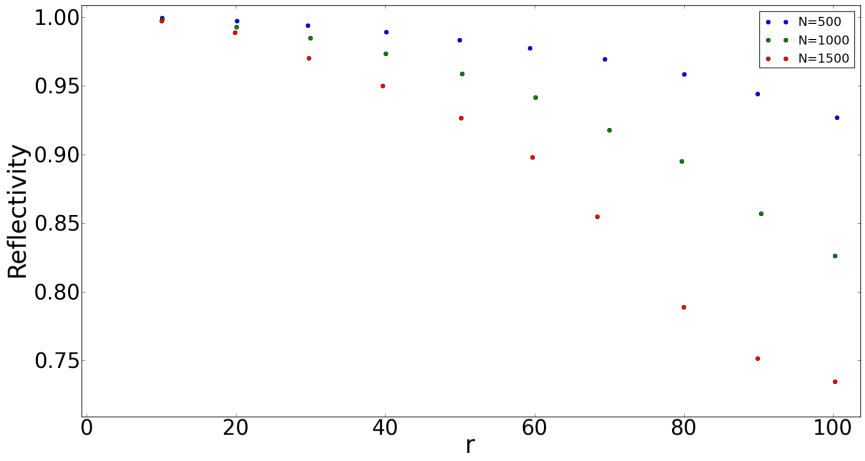

Figure 3.15: The reflectivity of a metallic foil covered with hydrogen molecular bubbles as a function of average radius of a bubble. Three different number of bubbles per one cm^2 are considered: 500, 1000, 1500, respectively.

Chapter 4

Conclusions and Outlooks

This thesis explained the importance of degradation processes of materials under space conditions. The space environment is highly rough for any technical equipment, since space is filled with high speed charge particles and electromagnetic radiation. In this thesis the solar sail technology was used as a reference example. The performance of sail-crafts is slightly defected to any changes of thermo-optical properties of their materials, since their propulsion abilities suffers from any degradation processes.

A short review of the most important degradation processes was given. A possibility of charge of metallic foils under particle irradiation was investigated. The following degradation processes that may appear in space have been discussed: the sputtering process, influence of the Atomic Oxygen, and effects of electromagnetic irradiation.

Recombination processes of incident protons with metal free electrons were investigated with special attention. A detailed mathematical description of the following three processes was presented: the Auger-, the resonant-, and the Oppenheimer-Brinkman-Kramers (OBK)-process, respectively. The author modified the OBK process that it is now suited for light incident ions. That is the case when metallic targets are irradiated by solar protons.

The central topic of this thesis was the development of a thermodynamical model of formation of molecular hydrogen bubbles on metallic surfaces under space conditions. The here presented model allows the description of bubble grow on selected materials and under well defined environmental conditions. The grow both of small bubbles (tens of Å in diameter) and larger ones (tens in μm in a diameter) can be modeled. The reflectivity of the Aluminum foil that is covered with different bubble surface densities and different radii was investigated. A quantitative relation between the bubble growth, the bubble surface density, and the reflectivity of the degraded foil has been derived. Therefore, bubble formation will reduce the propulsion abilities of any sail-craft.

Thus up to now available results of laboratory experiments with respect to molecular bubble growth under proton irradiation have been reviewed. A large set of different materials has been investigated. The collected experimental results and the numerical model lead to the conclusion that bubble growth processes may appear at least in the close vicinity of the Sun.

In the near future the formation theory of molecular hydrogen bubbles on metallic surfaces will be verified experimentally by use of the Complex Irradiation Facility (hereafter CIF) at DLR, Bremen, Germany. This facility is designed to study the behavior of materials under complex irradiation and to investigate their degradation in the space environment. With the CIF it is possible to irradiate samples with three light sources (for the simulation of the spectrum of solar electromagnetic radiation) simultaneously with protons and electrons.

Further theoretical studies of the bubble growth process are planned. Different equations of state of the hydrogen molecular gas will be tested. It would be interesting to study the dynamics of bubble growth with different gas models. A more sophisticated mechanism of bubble crack will be implemented. The idea is to take into account the dynamical thickness change of a bubble cap. Also a broad variation of merging process of H_2 molecules to a bubble will be studied.

Since for the foreseeable future no sample returns of materials exposed to interplanetary space is planned, both laboratory, and theoretical studies of degradation processes that are based on Hydrogen recombination are considered. They are nevertheless necessary, since bubble formation can be a serious problem for the success of space missions.

Appendix A

OBK recombination in metal lattices

A.1 The Hartree approximation

One can consider a multiparticle system described by a Hamiltonian (all particles are distinguishable) in the form:

$$H = \sum_{\mathrm{i}} H_{\mathrm{i}} + \frac{1}{2} \sum_{\mathrm{i} \neq \mathrm{j}} V_{\mathrm{i,j}}, \tag{A.1}$$

where $H_{\mathrm{i}} = \frac{p_{\mathrm{i}}^2}{2m} + V_{\mathrm{s}}(\mathbf{r}_{\mathrm{i}})$ and $V_{\mathrm{i,j}} = V_{\mathrm{int}}(\mid \mathbf{r}_{\mathrm{i}} - \mathbf{r}_{\mathrm{j}} \mid)$, here V_{s} is the single-particle potential and V_{int} is the interaction potential [71].

In the Hartree approximation, one assumes that the wavefunction of eigenstates of the Hamiltonian can be written as a product of wavefunctions of single particle states, thus [71]:

$$\Phi = \phi_1(\mathbf{r}_1)\ \phi_2(\mathbf{r}_2)\ \phi_3(\mathbf{r}_3)\ ... \tag{A.2}$$

The expectation value of the Hamiltonian will have the form:

$$\int d^3r_1 d^3r_2\ ...\ \phi_1^*(\mathbf{r}_1)\phi_2^*(\mathbf{r}_2)\ ...\ \left(\sum_{\mathrm{i}} H_{\mathrm{i}} + \frac{1}{2} \sum_{\mathrm{i} \neq \mathrm{j}} V_{\mathrm{i,j}} \right) \phi_1(\mathbf{r}_1)\phi_2(\mathbf{r}_2)\ ... \tag{A.3}$$

Thus one can realize that the sum over H_{i} and $V_{\mathrm{i,j}}$ reduces to one and two particle expectation values [71]. Taking the functional derivative of the above equation with respect to $\phi_{\mathrm{m}}^*(\mathbf{r}_{\mathrm{m}})$ for the m^{th} partcile, one has:

$$\int d^3r_{\mathrm{m}} \left(H_{\mathrm{m}}\phi_{\mathrm{m}}(\mathbf{r}_{\mathrm{m}}) + \sum_{\mathrm{i} \neq \mathrm{m}} \int d^3r_{\mathrm{i}} \phi_i^*(\mathbf{r}_{\mathrm{i}}) V_{\mathrm{i,m}} \phi_i(\mathbf{r}_{\mathrm{i}}) \phi_m(\mathbf{r}_{\mathrm{m}}) - E\phi_m^*(\mathbf{r}_{\mathrm{m}}) \right) \delta\phi_m^*(\mathbf{r}_{\mathrm{m}}) = 0 \tag{A.4}$$

Thus one can write Eq. A.4 in the form:

$$H_{\mathrm{m}}\phi_{\mathrm{m}}(\mathbf{r}_{\mathrm{m}}) + \left(\sum_{\mathrm{i} \neq \mathrm{m}} \int d^3r_{\mathrm{i}} \phi_i^*(\mathbf{r}_{\mathrm{i}})\ V_{\mathrm{i,m}}\ \phi_i(\mathbf{r}_{\mathrm{i}}) \right) \phi_m(\mathbf{r}_{\mathrm{m}}) = E\phi_m(\mathbf{r}_{\mathrm{m}}). \tag{A.5}$$

Stationary Schroedinger equation A.5 is called the Hartree equation [71]. Hartree approximation reduces a N-particle problem to a set of single equations that one can solve. The interaction between the particles is reduced to a single potential potential [71]:

$$V_{\mathrm{H}}(\mathbf{r}_{\mathrm{m}}) = \int d^3 r_{\mathrm{i}} \sum_{\mathrm{i}\neq\mathrm{m}} \mid \phi_{\mathrm{i}}(\mathbf{r}_{\mathrm{i}}) \mid^2 V_{\mathrm{int}}(\mathbf{r}_{\mathrm{i}} - \mathbf{r}_{\mathrm{m}}). \tag{A.6}$$

Equation A.6 describes the interaction of the m^{th} particle with all other particles. If one consider a Coulomb interaction between the particles, the Hartree potential looks like the interaction of one particle with the charge density of all other particles [71]:

$$V_{\mathrm{H}}(\mathbf{r}_{\mathrm{m}}) = \int d^3 r \, \frac{Z_{\mathrm{t}} Z_{\mathrm{p}} \rho_{\mathrm{m}}(\mathbf{r})}{\mid \mathbf{r}_{\mathrm{m}} - \mathbf{r} \mid}. \tag{A.7}$$

Here $\rho_{\mathrm{m}}(\mathbf{r})$ is the probability density that the m^{th} particle is located at position $\mathbf{r}$. Z_{t} and Z_{p} are a charge numbers of target ions and incident ions, respectively. The m^{th} particle depends on the states of all the other $N-1$ particles.

A.2 The ionization energy of an electron in the $1s$ state - the OBK process

The ionization energy of an electron in the $1s$ state is:

$$-I_{\mathrm{K}} = E(\alpha, C) = \langle \phi_{\mathrm{i}}(\mathbf{r}_1) \mid H \mid \phi_{\mathrm{i}}(\mathbf{r}_1) \rangle, \tag{A.8}$$

where the Hamiltonian and the wave function are:

$$H = -\frac{1}{2}\boldsymbol{\nabla}^2 - \frac{1}{r_1} - \frac{(Z_{\mathrm{t}} - 1)}{r_1} \exp(-C r_1), \tag{A.9}$$

$$\phi_{\mathrm{i}}(\mathbf{r}_1) = \pi^{-\frac{1}{2}} \alpha^{\frac{3}{2}} \exp(-\alpha \mathbf{r}_1). \tag{A.10}$$

To calculate the ionization energy one can use the spherical coordinate system. For simplicity one can consider each term of Eq. A.9 separately:

1. $\langle \phi_{\mathrm{i}}(\mathbf{r}_1) \mid -\frac{1}{2}\boldsymbol{\nabla}^2 \mid \phi_{\mathrm{i}}(\mathbf{r}_1) \rangle$:

$$\langle \phi_{\mathrm{i}}(\mathbf{r}_1) \mid -\frac{1}{2}\boldsymbol{\nabla}^2 \mid \phi_{\mathrm{i}}(\mathbf{r}_1) \rangle = -\frac{1}{2} \langle \phi_{\mathrm{i}}(\mathbf{r}_1) \mid \left[-\pi^{-\frac{1}{2}} \alpha^{\frac{5}{2}} \frac{2}{r_1} \exp(-\alpha r_1) + \pi^{-\frac{1}{2}} \alpha^{\frac{7}{2}} \exp(-\alpha r_1) \right]. \tag{A.11}$$

The first term in the Eq. A.11 is:

$$\begin{aligned} -\tfrac{1}{2} \int_V \pi^{-\frac{1}{2}} \alpha^{\frac{3}{2}} \exp(-\alpha \mathbf{r}_1) \left[-\pi^{-\frac{1}{2}} \alpha^{\frac{5}{2}} \frac{2}{r_1} \exp(-\alpha r_1) \right] dV = \\ 4\alpha^4 \int_0^\infty r_1 \exp(-2\alpha r_1)\, dr_1 = -\alpha^2 \frac{2\alpha r_1 + 1}{\exp(2\alpha r_1)} \mid_0^\infty = \\ -\alpha^2 \frac{1}{1 + \frac{(2\alpha r_1)^2}{2(1+2\alpha r_1)} + \frac{(2\alpha r_1)^3}{6(1+2\alpha r_1)} + \ldots} \mid_0^\infty = \alpha^2, \end{aligned} \tag{A.12}$$

and the second one is:

$$-\tfrac{1}{2}\quad \int_V \pi^{-\frac{1}{2}}\alpha^{\frac{3}{2}}\exp(-\alpha\mathbf{r}_1)\left[\pi^{-\frac{1}{2}}\alpha^{\frac{7}{2}}\exp(-\alpha\mathbf{r}_1)\right]dV = \tag{A.13}$$
$$-2\alpha^5\left[\exp(-2\alpha\mathbf{r}_1)\left(\frac{r_1^2}{-2\alpha}-\frac{2r_1}{4\alpha^2}-\frac{1}{4\alpha^3}\right)\right]|_0^\infty = -\frac{1}{2}\alpha^2.$$

So the term $\langle\phi_{\rm i}(\mathbf{r}_1)\mid -\frac{1}{2}\boldsymbol{\nabla}^2\mid\phi_{\rm i}(\mathbf{r}_1)\rangle = \frac{1}{2}\alpha^2$.

2. $\langle\phi_{\rm i}(\mathbf{r}_1)\mid -\frac{1}{r_1}\mid\phi_{\rm i}(\mathbf{r}_1)\rangle$:

$$\langle\phi_{\rm i}(\mathbf{r}_1)\mid -\frac{1}{r_1}\mid\phi_{\rm i}(\mathbf{r}_1)\rangle = -4\alpha^3\int_0^\infty r_1\exp(-2\alpha r_1)\,dr_1 = \tag{A.14}$$
$$\alpha\frac{2\alpha r_1+1}{\exp(2\alpha r_1)}\,|_0^\infty = \alpha\frac{1}{1+\frac{(2\alpha r_1)^2}{2(2\alpha r_1+1)}+\frac{(2\alpha r_1)^3}{6(2\alpha r_1+1)}+\ldots}\,|_0^\infty = -\alpha$$

3. $\langle\phi_{\rm i}(\mathbf{r}_1)\mid -\frac{(Z_{\rm t}-1)}{r_1}\exp(-Cr_1)\mid\phi_{\rm i}(\mathbf{r}_1)\rangle$:

$$\begin{aligned}
\langle\phi_{\rm i}(\mathbf{r}_1)\mid -\frac{(Z_{\rm t}-1)}{r_1}\exp(-Cr_1)\mid\phi_{\rm i}(\mathbf{r}_1)\rangle &= \\
-4(Z_{\rm t}-1)\alpha^3\int_0^\infty r_1\exp[-(C+2\alpha)r_1]\,dr_1 &= \\
4(Z_{\rm t}-1)\alpha^3\frac{\exp[-(C+2\alpha)r_1]}{(C+2\alpha)^2}[(C+2\alpha)r_1+1]\,|_0^\infty &= \\
4(Z_{\rm t}-1)\frac{\alpha^3}{(C+2\alpha^2)^2}\frac{1}{1+\frac{[(C+2\alpha)r_1]^2}{2[1+(C+2\alpha)r_1]}+\ldots} &= \\
-4(Z_{\rm t}-1)\frac{\alpha^3}{(C+2\alpha)^2}&
\end{aligned} \tag{A.15}$$

Thus, ionization energy of the electron in the $1s$ state is the sum of three terms calculated above:

$$-I_{\rm K} = \frac{1}{2}\alpha^2-\alpha-4(Z_{\rm t}-1)\frac{\alpha^3}{(C+2\alpha)^2} \tag{A.16}$$

A.3 Cross section of the OBK process

The initial and final wave functions of the active electron are:

$$\psi_{\rm i}(\mathbf{r}_1,t) = \phi_{\rm i}(\mathbf{r}_1)\exp\left(-ip\mathbf{v}\cdot\mathbf{r}-i\frac{1}{2}p^2v^2t\right), \tag{A.17}$$

$$\psi_{\rm f}(\mathbf{r}_2,t) = \phi_2(\mathbf{r}_2)\exp\left[i(1-p)\mathbf{v}\cdot\mathbf{r}-\frac{i}{2}(1-p)^2v^2t\right], \tag{A.18}$$

where:

$$\phi_{\rm i}(\mathbf{r}_1) = \pi^{-\frac{1}{2}}\alpha^{\frac{3}{2}}\exp(-\alpha\mathbf{r}_1), \tag{A.19}$$

$$\phi_{\rm f}(\mathbf{r}_2) = \pi^{-\frac{1}{2}}Z_{\rm p}^{\frac{3}{2}}\exp(-Z_{\rm p}\mathbf{r}_2). \tag{A.20}$$

Here $p = m_{\rm p}/(m_{\rm p} - m_{\rm t})$, $\mathbf{r}_1 = \mathbf{r} + p\mathbf{R}$, and $\mathbf{r}_2 = \mathbf{r} - (1-p)\mathbf{R}$, and $\mathbf{R} = \mathbf{b} + \mathbf{v}t$. If the mass of the incident ion is small compared to the mass of the target atom ($p = 0.036$ for Al as a target and p^+ as an incident ion) one can set the p parameter to zero. For that approximation $\mathbf{r}_1$ and $\mathbf{r}_2$ are, respectively:

$$\mathbf{r}_1 \cong \mathbf{r}, \tag{A.21}$$

$$\mathbf{r}_2 \cong \mathbf{r} - \mathbf{R}. \tag{A.22}$$

Thus the wave functions are:

$$\psi_{\rm i}(\mathbf{r}_1, t) \cong \phi_{\rm i}(\mathbf{r}_1), \tag{A.23}$$

$$\psi_{\rm f}(\mathbf{r}_2 = \mathbf{r} - \mathbf{R}, t) \cong \phi_2(\mathbf{r}_2 = \mathbf{r} - \mathbf{R}) \times \exp\left[i\mathbf{v}\cdot\mathbf{r} - \frac{i}{2}v^2 t\right]. \tag{A.24}$$

The Hamiltonian of the active electron is:

$$H = -\frac{1}{2}\boldsymbol{\nabla}_r^2 - \frac{\alpha}{r} + V_{\rm s}, \tag{A.25}$$

where V_s is the effective potential felt by the active electron (see Eq. 2.91):

$$V_{\rm s} = -\frac{Z_{\rm p}}{r - b - vt} + \frac{1}{r}\left[(\alpha - 1) - (Z_{\rm t} - 1)\exp(-Cr)\right]. \tag{A.26}$$

To calculate the cross section of the process [25] one has first to evaluate the so-called transition amplitude [55]:

$$A(b) = \frac{1}{i}\int_{-\infty}^{\infty} dt\ \langle\psi_{\rm f} \mid V_{\rm s} \mid \psi_{\rm i}\rangle, \tag{A.27}$$

$$\Sigma \sim \int_0^{\infty} db\ \mid A(b) \mid^2 b. \tag{A.28}$$

The first step will be to calculate the $\langle\psi_{\rm f} \mid V_{\rm s} \mid \psi_{\rm i}\rangle$ term:

$$\langle\psi_{\rm f} \mid V_{\rm s} \mid \psi_{\rm i}\rangle = \langle\psi_{\rm f} \mid \left[-\frac{Z_p}{r - b - vt} + \frac{\alpha - 1}{r} - \frac{Z_t - 1}{r}\exp(-cr)\right] \mid \pi^{-\frac{1}{2}}\alpha^{\frac{3}{2}}\exp(-Cr)\rangle, \tag{A.29}$$

For simplicity one can consider each term separately:

1. The $\langle\psi_{\rm f} \mid -\frac{Z_p}{r-b-vt} \mid \psi_{\rm i}\rangle$

$$\langle\psi_{\rm f} \mid -\frac{Z_p}{r-b-vt} \mid \psi_{\rm i}\rangle = \tag{A.30}$$
$$-4Z_{\rm p}^{\frac{5}{2}}\alpha^{\frac{3}{2}}\exp\left[Z_{\rm p}(b+vt)-\frac{i}{2}v^2t\right]\int_0^\infty r^2\frac{\exp[r(iv-\alpha-Z_{\rm p})]}{r-b-vt}\,dr =$$
$$8Z_{\rm p}^{\frac{5}{2}}\alpha^{\frac{3}{2}}\frac{\exp(Z_{\rm p}R-\frac{i}{2}v^2t)}{R(\alpha+Z_{\rm p}-iv)^3}$$

2. $\langle\psi_{\rm f} \mid \frac{\alpha-1}{r} \mid \psi_{\rm i}\rangle$:

$$\langle\psi_{\rm f} \mid \frac{\alpha-1}{r} \mid \psi_{\rm i}\rangle = \tag{A.31}$$
$$4Z_{\rm p}^{\frac{3}{2}}\alpha^{\frac{3}{2}}(\alpha-1)\exp\left(Z_{\rm p}R-\frac{i}{2}v^2t\right)\int_0^\infty r\exp[r(iv-Z_{\rm p}-\alpha)]\,dr =$$
$$4Z_{\rm p}^{\frac{3}{2}}\alpha^{\frac{3}{2}}(\alpha-1)\frac{\exp(Z_{\rm p}R-\frac{i}{2}v^2t)}{(iv-Z_{\rm p}-\alpha)^2}$$

3. $\langle\psi_{\rm f} \mid -\frac{Z_{\rm t}-1}{r}\exp(-cr) \mid \psi_{\rm i}\rangle$:

$$\langle\psi_{\rm f} \mid -\frac{Z_{\rm t}-1}{r}\exp(-Cr) \mid \psi_{\rm i}\rangle = \tag{A.32}$$
$$-4Z_{\rm p}^{\frac{3}{2}}\alpha^{\frac{3}{2}}(Z_{\rm t}-1)\exp\left(Z_{\rm p}R-\frac{i}{2}v^2t\right)\int_0^\infty r\exp\left[r(-Z_{\rm p}+iv-C-\alpha)\right]\,dr =$$
$$-4Z_{\rm p}^{\frac{3}{2}}\alpha^{\frac{3}{2}}(Z_{\rm t}-1)\frac{\exp\left(Z_{\rm p}R-\frac{i}{2}v^2t\right)}{(Z_{\rm p}+C+\alpha-iv)^2}$$

So, the matrix element i.e. the transition probability from the initial to the final state $\langle\psi_{\rm f} \mid V_{\rm s} \mid \psi_{\rm i}\rangle$ is:

$$\langle\psi_{\rm f} \mid V_{\rm s} \mid \psi_{\rm i}\rangle = 4Z_{\rm p}^{\frac{3}{2}}\alpha^{\frac{5}{2}}\exp\left(Z_{\rm p}R-\frac{i}{2}v^2t\right)\times \tag{A.33}$$
$$\times\left[-\frac{2Z_{\rm p}}{\alpha R(iv-Z_{\rm p}-\alpha)^3}+\frac{1-\alpha^{-1}}{(iv-Z_{\rm p}-\alpha)^2}+\frac{Z_{\rm t}-1}{\alpha(\alpha+Z_{\rm p}+C-iv)^2}\right].$$

The scattering amplitude is defined as the time integral over this matrix element:

$$A(b)=\frac{1}{i}\int_{-\infty}^{\infty}dt\,\langle\psi_{\rm f} \mid V_{\rm s} \mid \psi_{\rm i}\rangle = \tag{A.34}$$
$$\frac{2^3Z_{\rm p}^{\frac{5}{2}}\alpha^{\frac{3}{2}}\exp(Z_{\rm p}b)}{i(Z_{\rm p}-\frac{i}{2}v)v}\left\{-\frac{2}{b(iv-Z_{\rm p}-\alpha)^3\alpha}\left[1-\frac{1}{b(Z_{\rm p}-\frac{i}{2}v)}\right]+\frac{1-\alpha^{-1}}{(iv-\alpha-Z_{\rm p})^2}+\frac{Z_{\rm t}-1}{\alpha(\alpha+Z_{\rm p}+C-iv)^2}\right\}.$$

From Eq. A.28 suggests that the cross section of the OBK process depends strongly on the incident proton velocity $\Sigma\sim v^{-12}$. As it was mentioned in the Section 2.4.3, the OBK process has an energetic threshold above which it occurs. It is efficient for high energy ions with energies of some MeVs.

Appendix B

Formation of hydrogen molecular bubbles on metal surfaces

B.1 Volume of a cap of a sphere

Using the geometry shown in the Fig. 3.8 and the spherical coordinates, the volume of a cap of a sphere (hereafter the bubble) is:

$$V = \int_0^R \int_0^\theta \int_0^{2\pi} R'^2 \sin\theta' \; dR' d\theta' d\phi, \tag{B.1}$$

$$V = \frac{2\pi}{3} R^3 (1 - \cos\theta). \tag{B.2}$$

Given the relation between radius r and height a of the bubble, $R = \frac{1}{2a}(r^2 + a^2)$, the volume is:

$$V = \frac{\pi}{12} \left[\frac{r^2 + a^2}{a} \right]^3 (1 - \cos\theta). \tag{B.3}$$

The relation between the height and the radius of the bubble is:

$$a = r \left(\frac{1 - \cos\theta}{\sin\theta} \right). \tag{B.4}$$

If θ is set to 0 then $a = r = R = 0$, on the other hand if the θ angle is $\pi/2$ then $a = r = R$.

B.2 Helmholtz free energy of H_2 molecules placed in certain positions in the sample's lattice

To get the relation of the Helmholtz free energy of the H_2 molecules located at certain positions in the sample but outside the bubbles, the definition of the free energy is used:

$$F = E - TS, \qquad S = k_B \ln\Omega, \tag{B.5}$$

here E is the internal energy of the H_2 molecules located at certain positions in the metal lattice, S denotes the entropy, while Ω represents the number of ways in which the H_2 molecules can be arranged on the N_0 lattice sites.

The number of lattice sites can be expressed by:

$$N_0 = N_{\mathrm{A}} d_{\mathrm{CSDA}} \frac{A_{\mathrm{s}}^2}{M_{\mathrm{u}}}, \tag{B.6}$$

where d_{CSDA} is the CSDA range of the fastest incident proton [114], A_{s} is the irradiated area of the sample, and M_{u} is the molar mass of the sample's material.

The number of H_2 molecules located outside the bubbles at certain positions in the metal lattice is $N_{\mathrm{H_2}}^T - \sum_{\mathrm{i}}^{N_{\mathrm{B}}^{\mathrm{T}}} \sum_{\mathrm{j}}^{N_{\mathrm{it}}} N_{\mathrm{H_2,i,j}}$. Where $N_{\mathrm{H_2}}^T$ is the total number of H_2 molecules in the sample, while $\sum_{\mathrm{i}}^{N_{\mathrm{B}}^{\mathrm{T}}} \sum_{\mathrm{j}}^{N_{\mathrm{it}}} N_{\mathrm{H_2,i,j}}$ is the total number of H_2 molecules within all bubbles. The summation over the number of time steps j count the number of H_2 molecules in the i^{th} bubble. The second summation over the number of bubble i^{th}, counts the number of H_2 molecules within all bubbles. Therefore, performing the subtraction one gets the total number of H_2 molecules outside all bubbles, located at certain positions in the metal lattice. The entropy $k_{\mathrm{B}} \ln W$ of the collection of the H_2 molecules placed on a lattice site is [108]:

$$\begin{aligned} S &= k_{\mathrm{B}} \ln \frac{N_0!}{\left(N_{\mathrm{H_2}}^T - \sum_{\mathrm{i}}^{N_{\mathrm{B}}^{\mathrm{T}}} \sum_{\mathrm{j}}^{N} dN_{\mathrm{H_2,i,j}}\right)! \left[N_0 - \left(N_{\mathrm{H_2}}^T - \sum_{\mathrm{i}}^{N_{\mathrm{B}}^{\mathrm{T}}} \sum_{\mathrm{j}}^{N} N_{\mathrm{H_2,i,j}}\right)\right]!}, \\ &\cong -k_{\mathrm{B}} \left(N_{\mathrm{H_2}}^T - \sum_{\mathrm{i}}^{N_{\mathrm{B}}^{\mathrm{T}}} \sum_{\mathrm{j}}^{N} N_{\mathrm{H_2,i,j}}\right) \ln \left[\frac{N_{\mathrm{H_2}}^T - \sum_{\mathrm{i}}^{N_{\mathrm{B}}^{\mathrm{T}}} \sum_{\mathrm{j}}^{N} N_{\mathrm{H_2,i,j}}}{N_0}\right]. \end{aligned} \tag{B.7}$$

The internal energy E is given by the following relation:

$$E = \epsilon_{\mathrm{H_2}} \left(N_{\mathrm{H_2}}^T - \sum_{\mathrm{i}}^{N_{\mathrm{B}}^{\mathrm{T}}} \sum_{\mathrm{j}}^{N} N_{\mathrm{H_2,i,j}}\right), \tag{B.8}$$

where $\epsilon_{\mathrm{H_2}}$ is the binding energy of the H_2 molecule to a vacancy [67]. The internal energy of H_2 molecules located in the metal lattice sites is a product of the binding energy of a single H_2 molecule and the number of molecules.

The Helmholtz free energy of the H_2 molecules located outside the bubbles at certain positions in the metal lattice is then:

$$F_{\mathrm{H_2}} = \left(N_{\mathrm{H_2}}^T - \sum_{\mathrm{i}}^{N_{\mathrm{B}}^{\mathrm{T}}} \sum_{\mathrm{j}}^{N} N_{\mathrm{H_2,i,j}}\right) \left[\epsilon + k_{\mathrm{B}} T \ln \left(\frac{N_{\mathrm{H_2}}^T - \sum_{\mathrm{i}}^{N_{\mathrm{B}}^{\mathrm{T}}} \sum_{\mathrm{j}}^{N} N_{\mathrm{H_2,i,j}}}{N_0}\right)\right]. \tag{B.9}$$

B.3 Helmholtz free energy of H atoms in the sample

The number of H atoms in the sample and outside the bubbles is:

$$N_{\mathrm{H}} = N_{\mathrm{H}}^{\mathrm{T}} - 2 \left(\sum_{\mathrm{i}}^{\mathrm{N_B}} \sum_{\mathrm{j}}^{N} N_{\mathrm{H_2,i,j}} + N_{\mathrm{H_2}}^{\text{out. bubbles}}\right), \tag{B.10}$$

where $N_{\mathrm{H}}^{\mathrm{T}}$ is the total number of H atoms in the sample, so the number counts all of the incident hydrogen ions which have recombined into hydrogen atoms. Some of the hydrogen

atoms have recombined to H_2 molecules and some of the molecules are forming the bubbles. Hence to get the number of H atoms located on the lattice sites one has to subtract the total the total number of hydrogen atoms $\mathrm{N_H^T}$ and those hydrogen atoms which build H_2 clusters and H_2 bubbles. The reason of the factor 2 is that a single H_2 molecule consists of two H atoms.

The procedure to estimate the Helmholtz free energy of H atoms in the sample is the same as in Eq. B.9. Hence the term is:

$$F_{\mathrm{H}} = N_{\mathrm{H}} \left(\epsilon_{\mathrm{H}} + k_{\mathrm{B}} T \ln \frac{N_{\mathrm{H}}}{N_0} \right), \tag{B.11}$$

where ϵ_{H} is the migration energy of the H atom in the metal lattice. The migration energy is defined as the minimum energy which one has bring to the H atom to move it from the lattice site.

B.4 The derivatives of Helmholtz free energy of: gas of the i^{th} bubble, metal deformation caused by the bubble, H_2 molecules, and H atoms located outside the bubbles.

The quasistatic condition of the process of bubble grow leads to the following relation:

$$\frac{\partial F_{\mathrm{config}}}{\partial N_{\mathrm{H_2,i,j}}} = 0, \tag{B.12}$$

The assumption is fulfilled when the time scale of bubble growth is longer then the time scale of the formation of a H_2 molecule out of two H atoms and the thermodynamic equilibrium is rapidly re-established after merging a H_2 molecule to a given bubble during a given time step. Since the free energy of the system is given by the Eq. 3.13, the given condition B.12 can be written as a sum:

$$\frac{\partial F_{\mathrm{gas,i}}}{\partial N_{\mathrm{H_2,i,j}}} + \frac{\partial F_{\mathrm{md,i}}}{\partial N_{\mathrm{H_2,i,j}}} + \frac{\partial F_{\mathrm{surf,i}}}{\partial N_{\mathrm{H_2,i,j}}} + \frac{\partial F_{\mathrm{H_2}}}{\partial N_{\mathrm{H_2,i,j}}} + \frac{\partial F_{\mathrm{H}}}{\partial N_{\mathrm{H_2,i,j}}} = 0. \tag{B.13}$$

Derivatives of the free energy gas of the $\mathrm{i^{th}}$ bubble, of metal deformation caused by the bubble, and of H and H_2 molecules located on the lattice sites with respect to the number of H_2 molecules that merge on each time step to a babble, will be calculated separately. By use of the Helmholtz free energy of the gas, Eq. 3.14, the derivative is:

$$\frac{\partial F_{\mathrm{gas,i}}}{\partial N_{\mathrm{H_2,i,j}}} = -N k_{\mathrm{B}} T \ln \left(\frac{V_{\mathrm{max,i}}}{V_{\mathrm{min}}} \right) - \frac{3}{2} N k_{\mathrm{B}} T. \tag{B.14}$$

The free energy of a metal deformation caused by expanding $\mathrm{i^{th}}$ bubble is given by the Eq. 3.17, hence its derivative is:

$$\frac{\partial F_{\mathrm{md,i}}}{\partial N_{\mathrm{H_2,i,j}}} = \frac{3}{\pi} \frac{1+\gamma}{E} k_{\mathrm{B}}^2 T^2 \sum_{\mathrm{j}}^{\mathrm{N}} N_{\mathrm{H_2,i,j}} \left[2 r_{\mathrm{i}}^{-3} N - 3 r_{\mathrm{i}}^{-4} \frac{\partial r_{\mathrm{i}}}{\partial N_{\mathrm{H_2,i,j}}} \sum_{\mathrm{j}}^{\mathrm{N}} N_{\mathrm{H_2,i,j}} \right]. \tag{B.15}$$

The derivative of the Helmholtz free energy of the H_2 molecules (Eq. B.9) located outside the bubbles at certain positions in the metal lattice is:

$$\begin{aligned}
\frac{\partial F_{\mathrm{H_2}}}{\partial N_{\mathrm{H_2,i,j}}} &= -\epsilon_{\mathrm{H_2}} N N_{\mathrm{B}}^{\mathrm{T}} - N N_{\mathrm{B}}^{\mathrm{T}} k_{\mathrm{B}} T \ln\left(\frac{N_{\mathrm{H_2}}^{\mathrm{T}} - \sum_{\mathrm{i}}^{\mathrm{N_B^T}} \sum_{\mathrm{j}}^{N} N_{\mathrm{H_2,i,j}}}{N_0}\right) \\
&- k_{\mathrm{B}} T \left(N_{\mathrm{H_2}}^{\mathrm{T}} - \sum_{\mathrm{i}}^{\mathrm{N_B^T}} \sum_{\mathrm{j}}^{N} N_{\mathrm{H_2,i,j}}\right) \frac{N_0}{N_{\mathrm{H_2}}^{\mathrm{T}} - \sum_{\mathrm{i}}^{\mathrm{N_B^T}} \sum_{\mathrm{j}}^{N} N_{\mathrm{H_2,i,j}}} \frac{N N_{\mathrm{B}}^{\mathrm{T}}}{N_0} \\
&= -N N_{\mathrm{B}}^{\mathrm{T}} \left\{ \epsilon_{\mathrm{H_2}} + k_{\mathrm{B}} T \left[1 + \ln\left(\frac{N_{\mathrm{H_2}}^{\mathrm{T}} - \sum_{\mathrm{i}}^{\mathrm{N_B^T}} \sum_{\mathrm{j}}^{N} N_{\mathrm{H_2,i,j}}}{N_0}\right)\right]\right\}. \qquad \text{(B.16)}
\end{aligned}$$

The derivative of the Helmholtz free energy of the H atoms (Eqs. B.10 and B.11) located at certain positions in the metal lattice is (the procedure is the same as with Eq. B.16):

$$\frac{\partial F_{\mathrm{H}}}{\partial N_{\mathrm{H_2,i,j}}} = -2 N N_{\mathrm{B}}^{\mathrm{T}} \left[\epsilon_{\mathrm{H}} + k_{\mathrm{B}} T \left(1 + \ln \frac{N_{\mathrm{H}}^{T} - 2 N_{\mathrm{H_2}}^{T}}{N_0} \right) \right]. \qquad \text{(B.17)}$$

Acknowledgments

This thesis could no have been written without Professor Ulrich Geppert, who was my research supervisor. Professor Geppert is my mentor with an infinite amount of patience. He was always there, serving advices, and long discussions. I would like to also thank Professor Janusz Gil and Professor Giorgi Melikidze for support which allowed me to finish this thesis.

Table of Symbols

Symbol	Description
a	constant parameter
A	scattering amplitude
A_s	area of a sample
α_c	fine structure constant
α_m	constant parameter
α_s	solar absorption coefficient
BS	backscattering coefficient
c	speed of light
C	constant parameter
C_0	wavenumber
d_CSDA	Continuous Slowing Down Approximation (CSDA - range)
δ	scattering angle
$\delta(x)$	Dirac delta
E	total energy
E'	energy of an electron in the conduction band
E''	energy of an Auger electron in the conduction band
E_F	Fermi energy
E_h	Hartree energy
E_ion	total energy of an incident ion
E_K	kinetic energy
$E_{\mathrm{K}^\mathrm{e}}$	kinetic energy of an Auger electron
$E_\mathrm{pot}^\mathrm{ion}$	potential energy of an incident ion
$\mathbf{E}^\mathrm{ind}$	induced electric field
E_Y	Young module
ϵ	permittivity
ϵ_0	vacuum permittivity
ϵ_H	migration energy of H atom in the metal lattice
ϵ_{H_2}	binding energy of H_2 molecule with a vacancy
ϵ_m	constant parameter
ϵ_t	thermal emission coefficient
η	relation between the number of H_2 molecules and H atoms in the sample
F_C	Coulomb force
$F_\mathrm{gas,i}$	Helmholtz free energy of gas filled i^th bubble
F_H	Helmholtz free energy of H atoms placed outside the bubbles within the metal lattice
F_{H_2}	Helmholtz free energy of H_2 molecules placed outside the bubbles within the metal lattice
$F_\mathrm{md,i}$	Helmholtz free energy of metal deformation caused by the i^th molecular hydrogen bubble
$F_\mathrm{surf,i}$	Helmholtz free energy of a surface of the i^th molecular hydrogen bubble
$F(x, E, \kappa)$	amount of energy per unit length

$\mathbf{G}$	reciprocal vector of the lattice
γ	Lorentz factor
γ_{p}	Poisson coefficient
$\Gamma^{\mathrm{C,L}}$	probability per unit time of electron capture (C) or loss (L)
H	Hamiltonian
H_0	Hamiltonian of an electron gas
H_{i}	partial derivative sum
H_{I}	Hamiltonian of ion - active electron composite
$\hbar$	Plank constant
$\|i\rangle$	eigenfunction
I	flux of particles
I_{p}	ionization potential
I_{K}	experimental ionization potential of K shell
$I_{\mathrm{particles}}$	intensity of particles
$\bar{I}_{\mathrm{p}}$	mean ionization potential
k_{B}	Boltzmann constant
κ	direction cosine
$\|\mathbf{k}_{\mathrm{OPW}}\rangle$	Orthogonal Plane Wave
$\mathbf{k}_0$	total momentum of ion - active electron composite
l	orbital quantum number
$\bar{l}$	mean free path
L	angular momentum
L_{s}	thickness of a solar sail foil
L_{n+1}^{2l+1}	Laguarre polynomial
m	mass of an incident particle
M	mass of metallic foil ion
M_{u}	molar mass of an element
m_{e}	mass of an electron
m_{p}	mass of a proton
μ	attenuation coefficient
n	number of shell in atom
n_0	number density of lattice ions
n_{e}	number density of incident electrons
n_{i}	integer number
N	number of iterations
$N_{\mathrm{particles}}$	number of incident particles
N_0	number of lattice sites
N_{A}	Avogadro constant
N_{B}	number of molecular hydrogen bubbles per unit area
$N_{\mathrm{B}}^{\mathrm{T}}$	total number of molecular hydrogen bubbles on irradiated sample
N_{cells}	number of cells
N_{D}	number of dislocations in the metal lattice
$N_{\mathrm{H_2,i,j}}$	number of H_2 molecules merged to the i^{th} bubble
$N_{\mathrm{H_2}}^{\mathrm{T}}$	total number of H_2 molecules in the sample
$N_{\mathrm{p^+,j}}$	number of protons sent to the sample in the j^{th} time step

Ω	number of ways in which H_2 molecules can be arranged on lattice sites
p	constant parameter
p_{i}	pressure inside the i^{th} bubble
P	probability
Π	probability amplitude
$\psi(r, \theta, \phi)$	state function of Hydrogen atom
$\psi_{\mathrm{i,f}}$	wave function
$\phi(\mathbf{q}, \omega)$	scalar potential
$\phi_{\mathrm{i,f}}$	wave function
q	momentum
Δp	momentum transfer
Q_{s}	total surface charge
r, R	distance
r_0	Bohr radius
$r_{\mathrm{e}}(n)$	radius of an electron on the n^{th} shell in an atom
r_{i}	radius of the i^{th} bubble
$r_{\mathrm{max,i}}$	maximum radius of the i^{th} bubble
R_{cell}	reflectivity of a single cell
R_{foil}	reflectivity of a foil
$R_{n,l}(r)$	radial part of state function of Hydrogen atom
ρ	density of material
$\boldsymbol{\rho}$	distance between ion - active electron
ϱ	resistivity
$\varrho_{\text{crystal imperfections}}$	contribution to resistivity from crystal imperfections
ϱ_{D}	contribution to resistivity from dislocations in metal lattice
$\varrho_{\text{impurities}}$	contribution to resistivity from impurities from dislocations in metal lattice
$\varrho_{\mathrm{c}}(\mathbf{r}, t)$	charge density
S	entropy
SY	sputtering yield
σ	conductivity
σ_{s}	metal strain
$d\Sigma$	differential cross section
Σ_{A}	cross section for Auger recombination process
Σ_{OBK}	cross section for OBK recombination process
Σ_{R}	cross section for resonant recombination process
Σ_{RR}	cross section of radiative recombination process
Σ_{total}	total cross section
t	time
Δt_{j}	time step
T	temperature
Θ	Debye temperature
$\Theta(x)$	step function
$\mathbf{u}_0$	plane wave
U_0	surface binding energy
v	velocity of incident particle
v_{e}	velocity of incident electrons
$v_{\mathrm{e}}(n)$	velocity of electron on the n^{th} shell in an atom

v_{F}	velocity of a reference frame
$V(\mathbf{G})$	Hartree potential
$V(r)$	potential energy
V_{i}	volume of the i^{th} bubble
$V_{max,i}$	maximum volume of the i^{th} molecular hydrogen bubble
V_{min}	minimum volume of molecular hydrogen bubble
V_{S}	effective potential
ν	frequency of the electromagnetic radiation
W	work function
$d\Omega$	solid angle
ω	binding energy
ω_0	angular velocity of an electron in an ion
dx	penetration length
ξ	impact parameter
$\xi_{\mathrm{H_2}}$	relation between the number of H_2 molecules inside and outside the molecular hydrogen bubble
ξ_{max}	maximum value of the impact parameter
ξ_{min}	minimum value of the impact parameter
$Y_{l,m}(\theta,\phi)$	spherical harmonics
ze, Ze	charge

Table of Physical Constants

Table B.1: Physical constants

Physical constant	value	description
c	2.997925×10^{8} ms^{-1}	speed of light
h	6.6261×10^{-34} Js	Planck constant
e	1.6022×10^{-19} C	elementary charge
m_{e}	9.109×10^{-31} kg	electron mass
m_{p}	1.6726×10^{-27} kg	proton mass
ϵ_0	8.8542×10^{-12} C^{2}m^{-2}N^{-1}	permittivity of free space
ϵ_{Al}	0.05	emissivity of the Aluminium
N_{A}	6.02214×10^{23} mol^{-1}	Avogadro constant

Table B.2: Young and Poisson values for common materials.

Material	Young modulus $\times 10^9$ [Nm^{-2}]	Poisson coefficient
Aluminum	69	0.33
Cooper	117.0	0.36
Platinum	146.86	0.39
Polyimide	2.5	-
Titanium	110.32	0.30

List of Figures

List of Tables

Bibliography

[1] Abarenkov I. V., Physica Status Solidi B 50, 465 - 470, 1972.

[2] Abdullayeva M. K., Ayukhanov A. K., Shamsiyev U. B., Radiation Effects 19, 225-229, 1973.

[3] Agnolan D., Study Overview of Solar Sail Demonstrator: Geosail, SCI-PA, 1, 1 - 54, 2007

[4] Alston S., Physical Review A 27, 2342-2357, 1983.

[5] Araminowicz J., Małuszyńska K., Przytuła M., Laboratorium Fizyki Jadrowej, Państwowe Wydawnictwo Naukowe, 1978.

[6] ASTM, E512-94(2010), Standard Particle for Combined, Simulated Space Environment Testing of Thermal Control Materials with Electromagnetic and Particulate Radiation, 2010

[7] Astrelin V. T., Burdakov A. V., Bykov P. V., Ivanov I. A., Ivanov A. A., Jongen Y., Konstentinov S. G., Kudryavtsev A. M., Kuklin K. N., Mekler K. I., Polosatkin S. V., Postupaev V. V., Rovenskikh A. F., Sinitskiy A. L., Zubairov E. R., Journal of Nuclear Materials 396, 43-48, 2009.

[8] Banks B. A., Atomic Oxygen Effects on Spacecraft Materials, NASA/TM-2003-212484, 2003.

[9] Banks B. A., Scattered Atomic Oxygen Effects on Spacecraft Materials, Procedings of the 9^{th} International Symposium on Materials in a Space Environment, 2003.

[10] Banyard K. E., Szuster B. J., Physical Review A 16, 129-132, 1977.

[11] Behrisch R., Ergebn. Exakt. Naturw. 35, 295, 1964.

[12] Belkic Dz., Gayet R., Salin A., Physics Reports 56, 279-369, 1979.

[13] Bid A., Bora A., Raychaudhuri A. K., Physical Review B 74, 035426-035434, 2006.

[14] Bitetti G., Marchetti M., Mileti S., Valente F., Scaglione S., Acta Astronautica 60, 166-174, 2007.

[15] Bransden B. H., Cheshire I. M., Proceedings of the Physical Society 81, 820-832, 1963.

[16] Callaway J., Physical Review 97, 933-936, 1955.

[17] Carter G., Colligon J. S., Nobes M. J., Journal of Material Science 6, 115-117, 1971.

[18] Canham L. T., Dyball M. R., Leong W. Y., Houlton M. R., Cullis A. G., Smith P. W., Materials Science an Engineering: B 4, 41-45, 1989.

[19] Castaing R., Slodzian G., C. R. Acad. Sci. 255, 1893, 1962.

[20] Chew G. F., Physical Review 80, 196-202, 1950.

[21] Dachwald B., AIAA Conference, San Diego, California, 7 - 11 August 2005

[22] Daniels R. D., Journal of Applied Physics 42, 417-420, 1970.

[23] Das A., Melissions. A. C., Quantum Mechanics: A Modern Introduction, Gordon and Breach Science Publishers, 1990.

[24] Datta S. K., Crothers D. S. F., McCarroll R., Journal of Physics B: Atomic, Molecular and Optical Physics 23, 479-495, 1990.

[25] Decker F., Eichler J., Physical Review A 39, 1530-1533, 1989.

[26] Echenique P.M., Flores F., Ritchie R.H., Solid State Physics 43, 229-308, 1990.

[27] Echenique P.M., Flores F., Physical Review B 35, 8249-8251, 1987.

[28] ECSS-Q-ST-70-06C, Particle and UV Radiation Testing for Space Materials, 2008.

[29] ECSS-Q-ST-70-09C, Measurements of Thermo-Optical Properties Control Materials, 2008.

[30] Farnsworth H. E., Schlier R. E., George T. H., Burger R. M., Journal of Applied Physics 29, 1150-1162, 1958.

[31] Ford A. L., Reading J., F., Becker R. L., Physical Review A 23, 510-518, 1981.

[32] Garwin R. L., Jet Propulsion 28, 188-190, 1958.

[33] Geppert U., Biering B., Lura F., Block J., Straubel M., Rainhard R., Advances in Space Research 48, 1695-1701, 2011.

[34] Ghosh M., Mandal C.R., Mukherjee S.C., Physical Review A 35, 2815-2820, 1987.

[35] Gravielle M.S., Miraglia J.E., Physical Review A 38, 5034-5037, 1988.

[36] Griffths D. J., Podstawy elektrodynamiki, Państwowe Wydawnictwo Naukowe, Warszawa 2005.

[37] Grigorovici R., Denenyi A., Botila T., The number of free electrons in aluminium, 1961.

[38] Grossman E., Gouzman I., Nuclear Instruments and Methods in Physics Research B: Beam Interactions with Materials and Atoms 208, 48-57, 2003.

[39] Grossman E., Lifshitz Y., Wolan J. T., Moung Ch. K., Moung G. B., Journal of Spacecraft and Rockets 36, 75-78, 1999.

[40] Gudimenko Y., Ng R., Kleiman J. I., Iskanderova Z. A., Tennyson R. C., Hughes P. C., Milligan D., Grigorevski A., Shuiski M., Kiseleva L., Edwards D., Finckenor M. „Enhancement of Surface Durability of Space Materials and Structures in LEO Environment", Procedings of the 9th International Symposium on Materials in a Space Environment, 2003.

[41] Guinea F., Flores F., Echenique P.M., Physical Review B 25, 6109-6125, 1982.

[42] Habenicht S., Bolse W., Lieb K. P., Reimann K., Geyer U., Physical Review B 60, R2200-R2203, 1999.

[43] Hagstrum H. D., Physical Review 96, 336-365, 1954.

[44] Hartle J., B., Gravity An Introduction To Einstein's General Relativity, Pearson Education,2003.

[45] Heltzel S., Semprimoschnig C. O. A., van Esbeek M. R. J., Journal of Spacecraft and Rockets 46, 248-254, 2009.

[46] Herring C., Physical Review 57, 1169-1177, 1940.

[47] **The HyperPhysics**, *Georgia State University*, http://hyperphysics.phy.gsu.edu/hbase/quantun

[48] Izumi T., Itoh G., Materials Transactions 52, 130-134, 2011.

[49] Jackson J. D., Classical Electrodynamics, John Wiley & Sons, Inc., 1999.

[50] Kamada K., Sagara A., Kinoshita H., Takahashi H., Radiation Effects 103, 119-133, 1986.

[51] Kaminsky M., Das S. K., Applied Physics Letters 21, 443-445, 1972.

[52] Karmakar P., Ghose D., Surface Science 554, L101-L106, 2004.

[53] Kezerashvili R. Ya., Matloff G. L., Advances in Space Research 44, 859-869, 2009.

[54] Kezerashvili R. Ya., Matloff G. L., Journal of British Interplanetary Society 60, 169-179, 2007.

[55] Kuang Y. R., Physical Review A 44, 1613-1619, 1991.

[56] Kuang Y. R., Journal of Physics B: Atomic, Molecular and Optical Physics 24, 1645-1655, 1991.

[57] Landau L. D., Lifschitz M. J., Quantum Mechanics, Non-Relativistic Theory, 2003.

[58] Landau L. M., Lifschitz M. J., Theory of Elasticity, Pergamon Press, 1986.

[59] Lang K. R., Astrophysical Formulae: A Compedium for the Physicist and Astrophysicist, Spinger-Verlag, 1980.

[60] Lapicki G., Losonsky W., Physical Review A 15, 896-905, 1977.

[61] Lautrup B., Physics of Continuous Matter, 2nd Edition, Taylor & Francis Group, Baco Raton, Florida, USA, 2011.

[62] Lieb H. J., Herzog R. F. K., Journal of Applied Physics 34, 2893-2897, 1963.

[63] Lin C. D., Soong S. C., Tunnell L. N., Physical Review A 17, 1646-1654, 1978.

[64] Lindhard J., Nielsen V., Scharff M., 1968, K. Danske Vidensk. Selsk. Math.-Fys. Meddr, 36

[65] Lura F., Verhovtsva T., Yaremennko V. I., Telepnev V. D., Proceedings of the 7th International Symposium on Materials in Space Environment, Toulouse, France, 119, 1997

[66] Longair M. S., High Energy Astrophysics Vol 1: Particles, Photons and their Detection, Cambridge University Press, 1992.

[67] Lu G., Kaxiras E., Physics Review Letters 94, 155501-155505, 2005.

[68] Makeev M. A., Curno R., Barabási A. L., Nuclear Instruments and Methods in Physics Research Section B: Beam Interactions with Materials and Atoms 197, 185-227, 2002.

[69] Marco J., Remaury S., Tonon C., 11th International Symposium on Materials in a Space Environment, Aix-En-Provance, France, 2009.

[70] Martynenko Yu. V., Radiation Effects, 45, 93-101, 1979

[71] Mason Bruce, Homer L. Dodge Department of Physics and Astronomy, *Quantum Physics - lectures*

[72] McDonald M., McInnes C., Advances in Space Research 48, 1702-1716, 2011.

[73] McDonald R. J., Advances in Physics 19, 457-524, 1970.

[74] McCracken G. M., Reports on Progress in Physics 38, 241-327, 1975.

[75] Metzger H., Peisl J., Williams J., Journal of Physics F: Metal Physics 6, 2195-2207, 1976.

[76] Minton T. K., Garton D., Advanced Series in Physical Chemistry 11, 420-489, 2001.

[77] Milacek L. H., Daniels R. D., Cooley J. A., Journal of Applied Physics 39, 2803-2816, 1968.

[78] Milcius D., Pranevicius L. L., Templier C., J., Journal of Alloys and Compounds 398, 203-207, 2005.

[79] Miraglia J. J., Physical Review A 30, 1721-1726, 1984.

[80] Montenbruck O., Gil E., Satellite Orbits: Models, Methods, Applications, 2005.

[81] Myers S. M., Baskes, M. I., Birnbaum, H. K., Corbett, J. W., Deleo, G. G., Estreicher, S. K., Haller, E. E., Jena, P., Johnson, N. M., Kirchheim, R., Pearton, S. J., Stavola, M. J., Review of Modern Physics 64, 559-617, 1992.

[82] Nahar S. N., Pradham A. K., Radiation Physics and Chemistry 70, 323-344, 2003.

[83] Pauly N., Dubus A., Rösler M., Nuclear Instruments and Methods in Physics Research B: Beam Interactions with Materials and Atoms 193, 414 - 418, 2002.

[84] Penalba M., Arnau A., Echenique P.M., Nuclear Instruments and Methods in Physics Research B: Beam Interactions with Materials and Atoms 48, 138-141, 1990.

[85] Podgorsak E. B., Radiation Physics for Medical Physicists, Springer - Verlag Berlin Hildenberg, 2010.

[86] Pustowałow G. E., Fizyka Atomowa i Jadrowa, Państwowe Wydawnictwo Naukowe, Warszawa 1972.

[87] Raisbeck G., Yiou F., Physical Review A 4, 1858-1868, 1971.

[88] Ree F. H., Bender C. F., Journal of Chemical Physics 71, 5362-5376, 1979.

[89] Ren X., Chu W., Li J., Su J., Qiao L., Materials Chemistry and Physics 107, 231-235, 2008.

[90] Rooij A., Corrosion in Space - Encyclopedia of Aerospace Engineering, ESA-ESTEC, John Wiley & Sons Ltd., 2010.

[91] Rozenek P., International Journal of Hydrogen Energy 32, 2816-2823, 2007.

[92] Rösler M., Garcia de Abejo F.J., Physical Review B 54, 17158-17165, 1996.

[93] Romero M., Boscher D., ESA Workshop on Space Weather, ESA Space Environments and Effects Analysis Section (ESA TOS-EMA), ESTEC, Noordwijk, The Netherlands, 1998.

[94] Rusponi S., Costantini G., Boragno C., Valbusa U., Physical Review Letters 81, 4184-4187, 1998.

[95] Schiff L. I., Quantum Mechanics, McGraw-Hill Book Company, Inc., 1955.

[96] Sharma A. K., Sridhara N., Advance in Space Research 50, 1411-1424, 2012

[97] Slater J. C., Physical Review 98, 1039-1045, 1955.

[98] Slater J. C., Quantum Theory of Atomic Structure, McGraw-Hill, 1960.

[99] Sigmund P., Physical Review 184, 383-416, 1969.

[100] Sols F., Flores F., Physical Review A 37, 1469-1475, 1988.

[101] Sols F., Flores F., Physical Review B 30, 4878-4880, 1984.

[102] Stopping-power and range tables for protons, National Institute of Standards and Technology, http://physics.nist.gov/PhysRefData/Star/Text/PSTAR.html

[103] Szpikowski S., Podstawy Mechaniki Kwantowej, Wydawnictwo Uniwersytetu Marii Curie - Skłodowskiej, 2006.

[104] Taute E., Physica Status Solidi (b) 142, 437-443, 1987.

[105] Thomas G. J., Drotning W. D., Metallurgical Transactions A 14, 1545-1548, 1983.

[106] Vajo J. J., Doty R. E., Cirlin E. H., Journal of Vacuum Science & Technology A 14, 2709-2721, 1996.

[107] Verner D. A., Ferland G. J., Astrophysical Journal Supplement 103, 467-473, 1996.

[108] Wigner E., Seitz F., Physical Review 43, 804-810, 1933.

[109] Winter T. G., Lin C. C., Physical Review A 10, 2141-2155, 1974.

[110] Winterbon B. K., Sigmund P., Sanders J. B., K. Denske Vidensk. Selsk., Math. -Fys. Meddr 37, 1970.

[111] Wittmaack K., Journal of Vacuum Science & Technology A 8, 2246-2251, 1990.

[112] Zhao X. H., Shen Z. G., Xing Y. S., Ma S. L., Journal of Physics D: Applied Physics 34, 2308-2315, 2001.

[113] Ziegler J. F., Journal of Applied Physics 85, 1249-1273, 1999.

[114] Ziegler J. F., SRIM software, www.srim.org.

[115] Ziman J. M., Electrons and Phonons, Oxford at the Clarendon Press, 1960.

[116] Zimny R., Miskovic Z. L., Nedeljkovic N. N., Dedeljkovic Lj. D., Surface Science 255, 135-156, 1991.